ISAAC VINÍCIUS DO NASCIMENTO

Evaluation of rough contact models in multibody tribodynamics simulation

Sao Paulo
2024

ISAAC VINÍCIUS DO NASCIMENTO

Evaluation of rough contact models in multibody tribodynamics simulation

Corrected Version

Dissertation presented to the Polytechnic School of the University of Sao Paulo to obtain the degree of Master in Science.

Advisor: Prof. Dr. Francisco José Profito

Sao Paulo
2024

Este exemplar foi revisado e corrigido em relação à versão original, sob responsabilidade única do autor e com a anuência de seu orientador.

São Paulo, _____ de _____ de _____

Assinatura do autor: _____

Assinatura do orientador: _____

Catalogação-na-publicação

Nascimento, Isaac Vinícius
Evaluation of rough contact models in multibody tribodynamics simulation / I. V. Nascimento -- versão corr. -- São Paulo, 2024.
136 p.

Dissertação (Mestrado) - Escola Politécnica da Universidade de São Paulo. Departamento de Engenharia Mecânica.

1.multibody dynamics simulation 2.crank-slider mechanism 3.lubricated clearance joints 4.rough contact models 5.mixed lubrication regime I.Universidade de São Paulo. Escola Politécnica. Departamento de Engenharia Mecânica II.t.

Dedication

This work is dedicated to my family for their love and constant encouragement, to my dear wife Valdécia and to my little son Asafe.

Acknowledgements

I am grateful to God, who has given me the breath of life, and to my family and friends for encouraging me in all circumstances.

This work could not have been completed without the unconditional support of my dear wife, Valdécia, who has always been by my side and taken such loving care of our little son, Asafe. I shall also thank my friends at church for providing a fraternal and harmonious environment for more than ten years that I have been living in São Paulo.

Special thanks to my beloved parents, Raimundo Severiano do Nascimento and Lívia Nascimento dos Santos, and my dear sister, Lígia Dayenne do Nascimento, for their support and wise advice that even physically distant, they always are present in my life.

To my bosses in the Navy Nuclear Development Directorate (DDNM) for allowing me to attend classes a few working hours per week during the Master's program period.

I am grateful to my supervisor, Prof. Dr. Francisco José Profito, who, with patience and understanding, always directed and helped me overcome difficulties and develop the technical aspects of this work. So, I wish him a very successful career in academic life and all the best to his family.

I would like to thank Prof. Dr. Roberto Martins de Souza, who received me at the Laboratory of Surface Phenomena of the Polytechnic School of the University of São Paulo and gave me the initial orientations. His comments in the class presentation, activity reports, and qualification process were very important to reach the necessary level of this work.

Finally, I thank all the professors with whom I could learn and absorb knowledge during the classes, and also to the administrative team of the postgraduate program in the Mechanical Engineering Department for providing secure information about how to procedures during this time.

"... Get wisdom, get understanding: Forget it not; neither decline from the words of my mouth. Forsake her not, and she shall preserve thee: Love her, and she shall keep thee."
(Proverbs 4:5-6, Holy Bible)

Abstract

Current technological demands associated with stricter environmental legislation have caused changes and impacts on the design of engineering components operating under high thermal-mechanical loads and subjected to complex multiphysics phenomena that affect their performance and durability. For instance, the crank-connecting rod-piston-cylinder mechanism in internal combustion engines and reciprocating hermetic compressors experience friction, wear, and lubrication effects at the revolute joints, significantly influencing the overall system performance. To design and optimize such components in the context of rapid advancement of potential tribological solutions, engineers need accurate and fast simulation tools that can capture the tribodynamic behavior of the system under realistic working conditions. In particular, in the cases of systems working under mixed lubrication conditions, current simulation tools often rely on simplified rough contact models that do not account for the elastoplastic deformation of the surface asperities, leading to inaccurate predictions of contact loads and stresses. Therefore, there is a need for tribodynamic models that can represent the mixed lubrication regime and the rough contact mechanics more realistically in a computationally efficient way. In this context, the present study sought to analyze the tribodynamic behavior of a crank-slider mechanism with lubricated clearance joints operating under mixed lubrication conditions. For this purpose, a multibody tribodynamics modeling methodology that couples the tribological phenomena in lubricated clearance joints with the dynamic model of multibody systems is proposed using the multibody dynamics formalism. A mixed lubrication model based on the Reynolds equation with the fluid film cavitation modeling that complies with the mass-conservation principle and elastic and elastoplastic rough contact models are implemented and used to calculate the hydrodynamic and asperity contact loads. A comparative analysis is carried out to evaluate the influence of the contact model on the system performance, considering three configurations of lubricated revolute clearance joints. The simulation results indicated significant differences between the elastic and elastoplastic rough contact models evaluated in the tribological performance and dynamic behavior of the joints. In particular, for the configuration of the mechanism with all joints with clearance, the block–crank joint (B–CS) was the most requested, making it possible to observe variations of more than 50% between the elastic and elastoplastic models for the minimum oil film thickness parameter (MOFT) when surface separations were low ($h'/\sigma < 2$), resulting in significantly different peak pressures and power losses. Overall, due to the robustness of the mathematical formulations and physical mechanisms considered, it is suggested to use the KE or JG elastoplastic models when more detailed multibody tribodynamics analyses are desired, especially those involving wear and failure effects.

Keywords: Multibody dynamics simulation, crank-slider mechanism, lubricated revolute clearance joints, rough contact models, mixed lubrication regime.

Resumo

As atuais demandas tecnológicas associadas a legislações ambientais mais rigorosas têm provocado alterações e impactos no projeto de componentes de engenharia que operam sob elevadas cargas termomecânicas e estão submetidos a fenômenos multifísicos complexos que afetam seu desempenho e durabilidade. Por exemplo, o mecanismo biela-pistão-cilindro em motores de combustão interna e compressores herméticos alternativos experimentam efeitos de atrito, desgaste e lubrificação nas juntas de revolução, influenciando significativamente o desempenho geral do sistema. Para projetar e otimizar tais componentes no contexto do rápido avanço de possíveis soluções tribológicas, os engenheiros precisam de ferramentas de simulação precisas e rápidas que possam capturar o comportamento tribodinâmico do sistema sob condições de trabalho realistas. Em particular, nos casos de sistemas que trabalham sob condições de lubrificação mista, as ferramentas de simulação atuais baseiam-se frequentemente em modelos de contato rugoso simplificados que não levam em consideração a deformação elastoplástica das asperezas da superfície, levando a previsões imprecisas de cargas e tensões de contato. Portanto, há uma necessidade de modelos tribodinâmicos que possam representar o regime de lubrificação mista e a mecânica de contato rugoso de forma mais realista e computacionalmente eficiente. Neste contexto, o presente estudo buscou analisar o comportamento tribodinâmico de um mecanismo crank-slider com juntas com folga lubrificadas operando sob condições de lubrificação mista. Para tanto, é proposta uma metodologia de modelagem tribodinâmica multicorpos que acopla os fenômenos tribológicos em juntas com folga lubrificadas com o modelo dinâmico de sistemas multicorpos, utilizando o formalismo da dinâmica multicorpos. Um modelo de lubrificação mista baseado na equação de Reynolds com modelagem de cavitação de filme fluido que atende ao princípio de conservação de massa e modelos de contato rugoso elástico e elastoplástico são implementados e utilizados para calcular os carregamentos hidrodinâmico e de contato entre as asperezas. Uma análise comparativa é realizada para avaliar a influência do modelo de contato no desempenho do sistema, considerando três configurações de juntas de revolução com folga lubrificadas. Os resultados da simulação indicam diferenças significativas, entre os modelos elástico e elastoplásticos estudados, no desempenho tribológico e no comportamento dinâmico das juntas. Em particular, para a configuração do mecanismo com todas as juntas com folga, a junta bloco - manivela (B-CS) foi a mais solicitada, sendo possível observar variações da ordem de mais de -50 % de diferença entre os modelos elástico e elastoplásticos no parâmetro de mínima espessura de filme de óleo (MOFT), quando os valores de aproximação de superfície foram baixos ($h'/\sigma < 2$), resultando em significantes diferentes picos de pressão e de perda de potência por contato. No geral, devido à robustez das formulações matemáticas e dos mecanismos físicos considerados, sugere-se a utilização dos modelos elastoplásticos KE ou JG quando

se desejam análises tribodinâmicas multicorpos mais detalhadas, especialmente aquelas que envolvem efeitos de desgaste e falha.

Palavras-chaves: Simulação dinâmica multicorpos, mecanismo crank-slider, juntas de revolução com folga lubrificadas, modelos de contato rugosos, regime misto de lubrificação.

List of Figures

List of Tables

List of abbreviations and acronyms

ACE	Algebric Constraint Equations
APL	Asperity Power Loss
APP	Asperity Peak Pressure
B	Block
B–CS	Block-Crankshaft Joint
CEB	Chang, Etsion and Bogy Model
CM	Center of Mass of the Body
CR	Connecting Rod
CR–S	Connecting Rod-Slider Joint
CS	Crankshaft
CS–CR	Crankshaft-Connecting Rod Joint
DoF	Degrees of Freedom
GT	Greenwood and Tripp Model
GW	Greenwood and Williamson Model
HPP	Hydrodynamic Peak Pressure
ICE	Internal Combustion Engine
JG	Jackson and Green Model
KE	Kogut and Etsion Model
LUBST	LUBrication Simulation Toolbox
ME	Motion Equations
MOFT	Minimum Oil Film Thickness
ODE	Ordinary Differential Equations
PW	Pullen and Williamson Model

RJ	Revolute Joint
S	Slider
S–B	Slider-Block Joint
STD	Standard Deviation
TJ	Translational Joint
TPL	Total Power Loss
ZMC	Zhao, Maietta and Chang Model
SSV	Start-Stop Vehicle
HEV	Hybrid Electric Vehicle
PHEV	Plug-in Hybrid Electric Vehicle
BEV	Battery Electric Vehicle
NGV	Natural Gas Vehicle
FCEV	Fuel Cell Electric Vehicle
CONV	Conventional Vehicle

Contents

1 Introduction

As a result of the increasing restrictions imposed on the consumption of fossil fuels and polluting gas emissions, as well as the increased demand for alternative and sustainable sources of energy, several technological challenges have emerged concerning the development of more energy-efficient mechanical systems and with greater durability, mainly in the transportation and energy sectors (ALLMAIER; OFFNER, 2016). From a tribological point of view, alternatives to attempt such restrictions consist of developing coatings and structured surfaces, low-viscosity lubricants and additives formulation, and changing the operating regimes of the systems (*e.g.*, hybrid internal combustion engines with start-stop cycles). In this scenario, there is also a tendency towards the development of increasingly compact systems with higher density power downsizing technologies (*e.g.*, internal combustion engines with direct injection and turbocharger, modern reciprocating hermetic compressors and transmission systems for wind turbines), which results in components with smaller gaps and higher thermo-mechanical loads and stresses between the moving parts.

Figure 1 shows a gradual trend towards replacing conventional motor vehicles driven by burning fossil fuels, such as gasoline and diesel, with hybrid and completely electric vehicles, which will considerably reduce the emission of polluting gases. This trend also arises from the need for automakers and manufacturers to adapt to new legislation to control emissions and consumers' preference for more environmentally sustainable products and goods. This context presents several challenges to the design of the next generation of engine components.

More compact and turbocharged engines with more start-stop cycles and advanced gas emission control equipment are the main characteristics of the new generation of engines planned for the coming decades. Accompanying these trends, the lubricating oils available on the market will gradually have lower viscosities and a greater quantity of additives to support the high thermo-mechanical loads and guarantee low friction and wear resistance between the moving parts. This tendency is observed in Figure 2, which shows the evolution in recent years and forecast of the gradual replacement of more viscous SAE-rated oils for less viscous oils in the North American market.

Crank–connecting rod–piston mechanisms are widely used in mechanical equipment and machines, such as internal combustion engines and reciprocating compressors. Such mechanisms make it possible to convert the rotational motion of a driver crank into a linear reciprocating motion and vice versa. The bodies that compound these mechanisms are normally connected by revolute joints and a translational joint that restricts the final

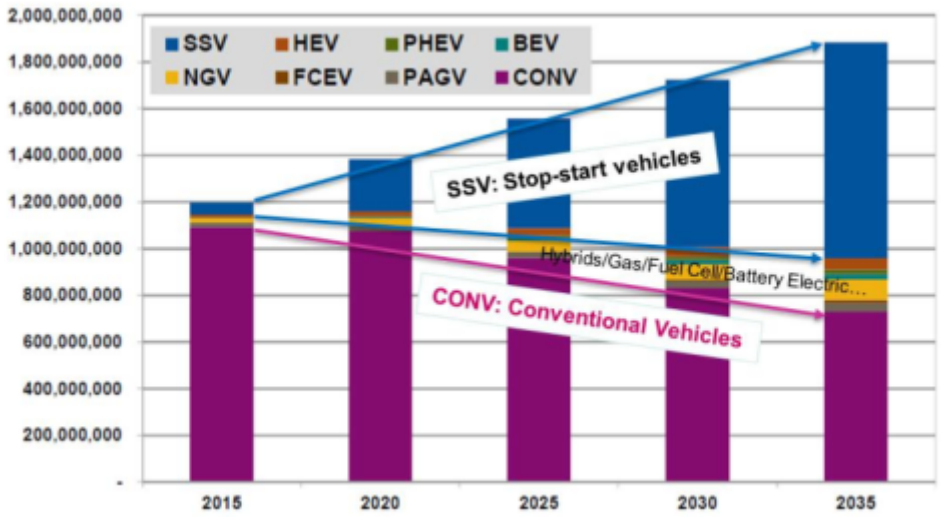

Figure 1 – Growth trend in the number of start-stop vehicles and replacement of conventional vehicles in the coming years.

Source: from Navigant Research *apud* Zhmud (2018).

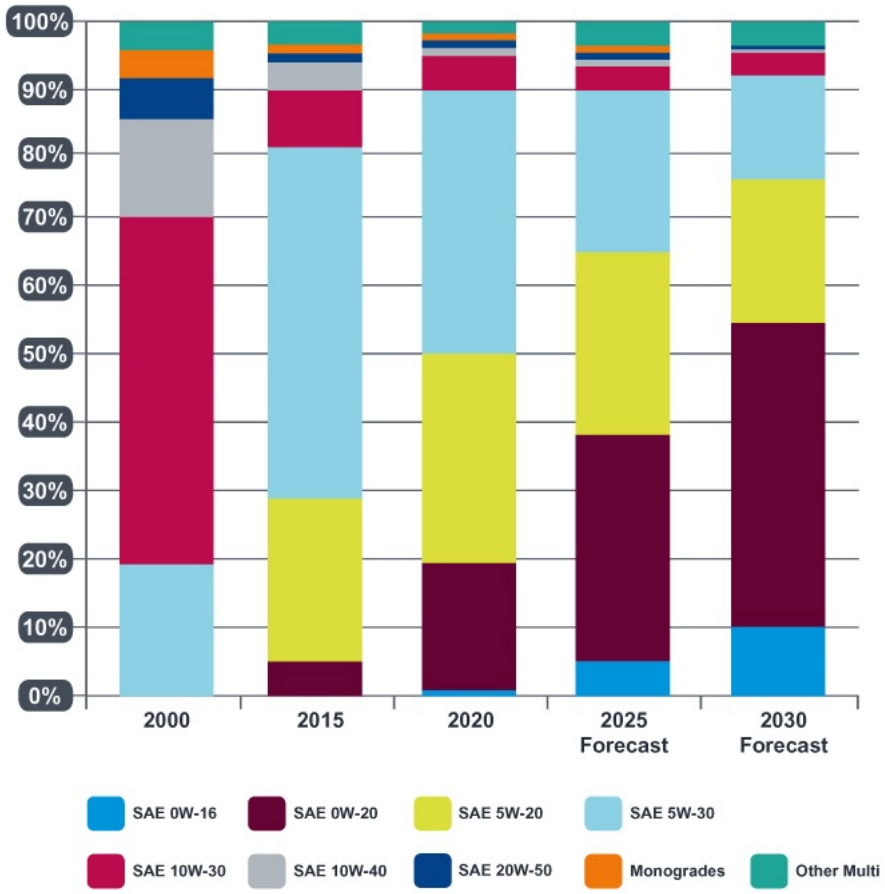

Figure 2 – Gradual trend of shifting from more viscous engine oils to lower viscosity lubricants in the North American market.

Source: Insight (2020).

movement of the piston in one direction. Clearance revolute joints, also known as journal bearings, possess a radial clearance whose precision and reliability are affected by the manufacturing process, mechanical assembling, and wear and tear effects. It is well-known from experimental and theoretical studies that revolute joints with not well-designed clearances are prone to several mechanical problems, such as high levels of assembly vibrations and power dissipation, severe wear and fatigue, and even the failure of the mechanical component (RAVN, 1998; FLORES, 2008).

1.1 Background

A review of theoretical and experimental works on bearings for reciprocating machinery was presented by Campbell et al. (1967). They used a case study based on empirical data of a dynamically loaded bearing to relate the results obtained from mathematical models. They addressed from hand- and graphical methods to numerical computer methods capable of predicting the journal's full path for some cases. Special attention was paid to the minimum oil film thickness (MOFT) obtained by experimental tests or calculated by the theoretical models.

Dubowsky and Freudenstein (1971a) proposed a mathematical model for an elastic mechanical joint with clearance in which the dynamic equations of motion were derived to various operating conditions. Their model was developed using the damper-spring approach and applying the Hertzian elastic contact model concept coupled with the equations of motion. In the second part of the study, the authors applied the mathematical model developed to determine the dynamic response under various operating conditions (DUBOWSKY; FREUDENSTEIN, 1971b).

One of the first works that investigated the behavior of a statically loaded journal bearing in start-stop operation was published by Mokhtar, Howarth and Davies (1977). Evaluating the movement of the shaft experimentally, whose center moves in the form of a spiral at the beginning until it finds a stable position, the authors observed that before the occurrence of the complete separation of the surfaces by the lubricating film at the starting regime, the contact was mainly of sliding with little or no rolling; on the other hands, at the stopping regime, the shaft followed a typical hydrodynamic *loco* until the rotation ended. Under typical startup conditions, the hydrodynamic forces were rapidly generated and soon dominated the journal's loading behavior. Furthermore, there was mainly sliding between the shaft and bearing surfaces, the contact time was on the order of a small fraction of a second, and when a hydrodynamic film was formed separating the shaft and bearing surfaces, the shaft took up a whirling motion around the steady-state operating position. Although the experimental work dealt with a single bearing subjected to constant loading, it was very useful in understanding the orbital movement and contact

behavior of a journal bearing system in start-stop conditions.

Rogers and Andrews (1977) presented the description of a computer program able to simulate dynamic planar systems with clearances in the revolute connections. The program was based on the vector network method and contained mathematical models considering the effects of clearance, surface compliance, and lubricant. When in contact conditions, clearance connections were modeled using the load-deflection relationship.

An experimental study was presented by Dubowsky and Moening (1978) to validate an analytical model to calculate the impact forces in clearance joints. They used the Lagrangian approach to derive the equations of motion and included perturbation coordinates to model mechanisms with elastic links and clearance connections. Their conclusions corroborate the information that the impact forces resulting from mechanism clearances are greater than the forces calculated when considering the same mechanism without clearances, and it can contribute to rapid wear and lead to total mechanism failure. Afterwards, Haines (1985) conducted an experimental investigation of the dynamic behavior of dry clearance revolute joints with varying degrees of clearance. They pointed out the prediction of the moment in which the pin and the journal maintain or lose continuous sliding contact as one of the key aspects since it is associated with a major cause of vibration.

A continuous contact model for impact contact analysis of multibody systems was proposed by Lankarani and Nikravesh (1985) by combining the general tendency of the Hertz contact law with a hysteresis damping factor. The hysteresis damping factor, which accommodates energy dissipation during contact, is a function of impact velocity, material properties, and coefficient of restitution.

Soong and Thompson (1990) carried out an analytical investigation of the dynamic response of a general planar kinematic chain of interconnected rigid bodies linked by revolute joints with clearance. In their analysis, the motion equations were established by incorporating a four-mode model of the phenomenological behavior of each revolute joint into the generalized form of the Lagrange equations. The dynamic behavior predicted by the proposed methodology was compared with the corresponding response data from a complementary experimental investigation.

The dynamic response of a dry revolute clearance joint in a rigid four-bar mechanism was investigated by Rhee and Akay (1996). The authors used the Lagrangian approach to model the motion of a rocker-arm pin at the ground connection and provided results regarding the pin trajectories and Poincaré maps. Their results showed that the pin motion can range from simple periodic motions to periodic motions with periods multiples of the crank revolution, and, in some cases, the motion becomes chaotic. They noted that when the friction between the pin and bearing surfaces was considered, the strongly nonlinear behavior of the system disappeared, and the response became periodic. Numerical results

also showed nonlinear dependence on the clearance size and friction coefficient.

Flores, Ambrósio and Claro (2004) presented a study of the kinematic and dynamic characteristics of a crank-slider mechanism considering the clearance of the revolute joint linking the connecting rod to the slider. They proposed a simulation methodology that incorporated the dry and lubricated conditions of the joint individually and in a hybrid way, including a function to make a continuous transition between the hydrodynamic lubrication and contact models. The authors concluded that the simulation results considering friction and lubrication effects seem more realistic because of the reduced levels of impact forces and decreased unrealistic high peaks in the slider acceleration found in the dry contact condition. It was also noted that these mechanical systems with clearance joints can have a predictable nonlinear response, an essential feature for designing and controlling these mechanisms. Later on, Flores et al. (2006) used the proposed methodology with analytical hydrodynamic and contact impact models to evaluate the dynamic behavior of mechanical systems with realistic revolute joint characteristics. The hydrodynamic lubrication theory for infinitely long journal bearings under dynamically loaded conditions was used to calculate the forces generated by the lubrication action. They concluded that the lubricated joint acts like a nonlinear spring damper element that introduces damping and stiffness to the system and avoids direct surface contact. Results also revealed that clearance, friction, and lubrication phenomena are always present and can significantly alter the system's dynamic response. Consequently, the ability to model these phenomena plays an important role in accurately predicting the dynamic behavior of mechanical systems. In their study, a lubricant that allowed the clearance revolute joint to keep an orbit movement closer to the center of the bearing was used, where there was no lubricant film breaking. Afterwards, Flores et al. (2007) proposed a general methodology to assess the influence of the clearance and friction coefficient of revolute joints on the dynamic response of rigid planar multibody systems. Their results predicted the existence of periodic or regular motion at certain clearance sizes and friction coefficients and chaotic behavior in other cases.

A methodology for modeling and analyzing planar flexible multibody systems with clearance and lubricated revolute joints based on the absolute nodal coordinate method was introduced by Tian, Zhang and Yang (2010). They used the Lankarani-Nikravesh formulation to model the contact forces and the analytical solution of infinitely long journal bearings to compute the hydrodynamic forces. In addition, as proposed by Flores, Ambrósio and Claro (2004), they used a hybrid function to simulate the transition between the hydrodynamic and contact models. The simulation results indicated that the contact forces for the flexible system are much smaller than the contact forces for the rigid system, and the fluid lubricant can greatly reduce the impact between the contacting surfaces.

Koshy, Flores and Lankarani (2013) conducted a comparative analysis between the

Hertz and Lankarani-Nikravesh contact models using the multibody dynamics simulation software MSC-ADAMS® and experimental results for a crank-slider mechanism. Due to the elastic characteristic of the components, both models presented higher acceleration peaks than the experimentally observed ones. Still, due to a dissipative term, the Lankarani-Nikravesh model showed better agreement with experimental data than the Hertz model. The authors pointed out that selecting the appropriate force model and the dissipative term is crucial to predicting the dynamic behavior of multibody systems involving contact events.

The influence evaluation of clearance sizes in the dynamic behavior of a crank-slider mechanism was performed by Wang and Liu (2015) using an improved nonlinear elastic damping contact model and a modified Coulomb friction model. Their analysis did not consider the effects of lubrication and flexibility of the bodies. They observed that clearance joints cause high peaks in the systems' kinematic and dynamic characteristics. With the enlargement of the radial clearance, the slider acceleration, joint reaction forces, and crank moment significantly fluctuate with increasing amplitudes.

Zhao et al. (2016) developed a simulation framework to analyse the dynamic behavior of the crank–connecting rod–piston mechanism of an ICE with clearance on the piston-pin revolute joint. They used the finite element method to solve the modified Reynolds equation based on the average flow model by Patir and Cheng for mixed lubrication. The Lankarani-Nikravesh model was used to calculate the contact forces, and the LuGruge friction model was used to calculate the sliding and stiction friction and stick-slip transitions. The dynamic motion equations were obtained using the Lagrange formulation.

Recent works, such as Zhao et al. (2016), Lu et al. (2018), Fang et al. (2019), Fang et al. (2021), have employed in their dynamic analysis of ICE crank–connecting rod–piston mechanisms, the Greenwood and Williamson (GW) or Greenwood and Tripp (GT) elastic rough contact model to calculate the contact pressure, and applied either the Finite Element Method (FEM), Finite Volume Method (FVM) or Finite Difference Method (FDM) to solve numerically the Reynolds equation for the hydrodynamic pressure.

Most of the works mentioned above employed smooth contact-impact models for multibody system dynamics simulations with clearance joints. A detailed analysis of the journal orbits in clearance revolute joints obtained with smooth contact-impact models shows that these models allow a major normal penetration of the journal within the bearing compared to the results predicted with rough contact models. Such high penetration calculated with contact-impact models may sometimes be unrealistic depending on the operating conditions and simulation parameters.

Applying smooth contact-impact models in multibody dynamic simulations requires accurately predicting the instant of contact occurrence. This is important to define the

continuous transition between the hydrodynamic lubrication and contact models, thus demanding the implementation of adaptive time-stepping strategies in the simulation algorithm. The importance of identifying contact detection for contact impact analysis in multibody dynamic systems was studied by Flores and Ambrosio (2010). However, it is important to remark that when using a solver that calculates the hydrodynamic and rough contact loads simultaneously, the transition aspect between the mixed and full-film hydrodynamic lubrication regimes ceases to be a problem once the pressures are evaluated depending solely on the gap between the surfaces. Yet, the time-step selection and control are still important for the simulation stability and convergence due to the high nonlinearities of the joint interface models.

Two approaches have been given to the theoretical treatment of rough contact mechanics: statistical and deterministic. The statistical approach allows for the calculation of the real contact area and contact load using analytical expressions derived as a function of the probability distribution function and statistical parameters associated with the surface asperities. The advantage of such an approach is the easier calculation of the contact parameters for arbitrary surfaces without needing any previous time-consuming rough contact mechanics simulation. However, depending on the nature of the surface texture of the bodies in contact, the statistical approach may lead to error if the probability distribution function is inconsistent and does not adequately reflect the distribution of the asperity heights. In the deterministic approach, the contact load and real contact area are calculated from contact models defined in the microscopic (roughness) scale. Some disadvantages of the deterministic approach are (i) the definition and calculation of the asperity curvature radii, (ii) the individual calculation of contact parameters for each asperity, and (iii) the higher computational effort due to the greater number of surface points. The deterministic approach can be advantageous when the analyzed surface texture requires a more precise evaluation of local contact mechanics effects. Therefore, it is necessary to evaluate the surface texture of the solids in contact to assess which approach is more appropriate according to the desired accuracy.

Several statistical rough contact models have been proposed in the literature (PULLEN; WILLIAMSON, 1972; CHANG; ETSION; BOGY, 1987; ZHAO; MAIETTA; CHANG, 2000; KOGUT; ETSION, 2003; JACKSON; GREEN, 2006). The basic model often used to develop more complex models has been the model introduced by Greenwood and Williamson (1966), in which the contact occurs between an equivalent rough surface with asperities of different heights and a smooth flat plane within the elastic regime. This widely applied model offers good results when the loading is low, the asperity distribution is close to the Gaussian distribution, and the asperity deformation does not exceed the elastic regime. However, many of the rough contact interactions found in the most diverse mechanical applications exceed the limit of the elastic regime of the material. This way, evaluating rough contact problems with the GW model can lead to non-negligible errors.

To minimize this limitation, many researchers have presented models that extend the basic hypothesis of elastic deformation of the Greenwood and Williamson model to the elastoplastic regime to obtain theoretical results that are more consistent with the results experimentally observed. In the context of statistical contact models, we can cite the models proposed by Chang, Etsion and Bogy (1987), which is based on the conservation of the volume of the asperities during plastic deformation; Zhao, Maietta and Chang (2000), which incorporates the transition from elastic deformation to fully plastic flow using an analytical function; and Kogut and Etsion (2003) and Jackson and Green (2006) that involves finite element analysis for modeling elastoplastic contact.

In recent work, Ghaednia et al. (2017) reviewed the state-of-the-art of elastoplastic asperity contact modeling. Their work highlighted the importance of considering the elastoplastic behavior in the asperity contact, mainly when using metallic materials, because of the high pressures and stresses involved in the contact resulting in the yielding of the material.

As noted previously, most multibody system dynamics research studies have applied contact-impact models in their analysis for various reasons, either by preference, performance, or ease of implementation. Moreover, works on multibody dynamics simulation have only recently used simple elastic rough contact models, such as the Greenwood & Williamson and Greenwood & Tripp models. It is well known that such models allow a good approximation when smooth contact occurs within the asperities elastic limit; however, when there is a heavier contact between the asperities, consideration of elastoplastic material behavior can be an important factor influencing the joint design parameters and materials and even the choice of the lubricant for given system application. Therefore, using elastoplastic rough contact models, which offer more accurate estimates of the contact loads, may enable more realistic predictions of joints' dynamic and tribological performances in multibody system dynamics analysis.

1.2 Objectives

According to the preceding introduction and background, the main objectives of the present work are:

- Couple multibody dynamics modeling with the tribology analysis of clearance joints.
- Evaluate the influence of different rough contact models on the lubrication and tribodynamic behaviors of a crank–connecting rod–slider mechanism with clearance joints operating under mixed lubrication conditions.
- Implement the developed multibody tribodynamics modeling methodology and elastoplastic rough contact models in the computational code LUBST (LUBrication

Simulation Toolbox).

- Start the development of a graphical user interface (GUI) for the LUBST framework to enable code sharing and interactions with non-developers and/or non-academic users.

2 Mathematical Modeling

2.1 Multibody Dynamics Formulation

This section presents the basic concepts of the multibody system dynamics modeling used in this work.

According to Nikravesh (2007), modeling a mechanical system requires knowing its individual components so that if they move relative to each other, such a system can be called a multibody mechanical system. Interconnection between its elements or bodies can be made through kinematic joints, springs, dampers, simple contact, or other elements. With the advent of the computer, many complex multibody dynamics analyses have been resolved quickly, efficiently, and accurately due to the high computational processing capacity.

Traditionally, kinematic and dynamic multibody system analyses were carried out assuming the bodies as rigid and without considering the physical properties of the joints. Kinematic solutions were obtained using graphical or analytical methods for simplified cases. However, with the increased use of computers, numerical solutions of complex multibody systems then began to be developed (FLORES, 2008) (2008).

According to Nikravesh (1988), computational programs for multibody system analyses can be formulated for general or specific purposes. A specific-purpose program is often structured to provide analyses of a single application, while a general-purpose program can enable the analysis of a diversity of mechanical systems, be it planar (2D) or spatial (3D). Specific programs can be computationally efficient with low storage requirements and less computational capacity. Conversely, general programs are not computationally so efficient, needing more memory spacing, but they are much more flexible. Both programs purpose receive the input data from the user and provide the equations of motion of the system components and their numerical solution.

The computational efficiency of a general-purpose multibody dynamics program depends on several factors, such as the choice of coordinates and the numerical solution methods. The choice of coordinates directly influences the number of equations of motion and their degree of nonlinearity (NIKRAVESH, 1988). Three coordinates formulations are often used in multibody dynamics modeling, namely (i) the generalized coordinates that are in the same number of the DoF needed to describe the system configuration, (ii) the relative coordinates that can define the orientation of each body with respect to a fixed body or other body in movement, and (iii) the global Cartesian coordinates of the bodies center of mass and the orientation angles that define the position of the local

Table 1 – Comparative board of the coordinates formulations often used for multibody dynamics modeling.

Coordinates	Generalized	Relative	Cartesian
Number of coordinates	minimum	moderate	high
Number of ODEs	minimum	moderate	high
Number of ACEs	none	moderate	high
Nonlinearity	high	moderate	low
Derivation of MEs	difficult	moderately difficult	simple
Computational efficiency	efficient	efficient	less efficient
Coding complexity	difficult	relatively difficult	easy

Source: from Nikravesh, (1988).

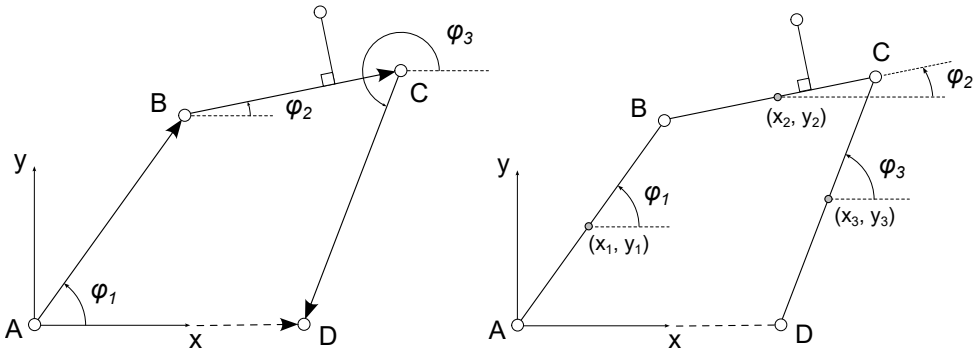

Figure 3 – Configuration of a four-bar system: (a) relative coordinates; (b) Cartesian coordinates.

Source: adapted from Nikravesh, (1988).

bodies coordinate systems relative to the global coordinate system (NIKRAVESH, 1988; SHABANA, 2013). A comparative board of these coordinates formulations is presented in Table 1 considering the number of coordinates, the number of ordinary differential equations (ODEs), the number of algebraic constraint equations (ACEs), the nonlinearity order, the derivation of motion equations (MEs), the computational efficiency, and the coding complexity. Figure 3 shows a four-bar mechanism described using relative and Cartesian coordinates formulations.

Although the Cartesian coordinates formulation presents more coordinates, ODEs, and ACEs, this formulation will be adopted in this work due to its easier implementation and derivation of the motion equations.

2.1.1 Kinematics

Kinematics studies the motion of systems regardless of the forces that produce it. As the forces are not considered in kinematic analyses, the movement of the bodies is specified by driving elements that govern the motion of specific degrees of freedom. The

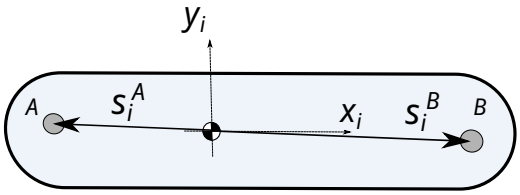

Figure 4 – Points A and B of the body i and their local coordinates vectors $\mathbf{s}_i^A$ and $\mathbf{s}_i^B$.

position, velocity and acceleration of the remaining bodies are determined by kinematic constraint equations that describe the system's topology (FLORES, 2008).

The configuration of a multibody system is identified by a set of variables called coordinates that completely define the location and orientation of each body at each instant of the movement (SHABANA, 2013). In the Cartesian coordinates formulation, the position ($\mathbf{q}$) and velocity ($\dot{\mathbf{q}}$) vectors are constituted by data of the linear and angular positions and velocities of the bodies with respect to a fixed global coordinate system. For instance, in a planar motion, each body has three DoF: two translations in the x and y directions (coordinates x and y), and one rotation around an axis perpendicular to the plane of motion (angular coordinate ϕ). In this way, the position, velocity and acceleration vectors of each body that comprises a multibody system with N moving bodies can be defined as

$$\mathbf{q}_i^T = \begin{bmatrix} \varphi_i & x_i & y_i \end{bmatrix}, \quad i = 1, 2, 3, ..., N \tag{2.1}$$

$$\dot{\mathbf{q}}_i^T = \begin{bmatrix} \dot{\varphi}_i & \dot{x}_i & \dot{y}_i \end{bmatrix}, \quad i = 1, 2, 3, ..., N \tag{2.2}$$

$$\ddot{\mathbf{q}}_i^T = \begin{bmatrix} \ddot{\varphi}_i & \ddot{x}_i & \ddot{y}_i \end{bmatrix}, \quad i = 1, 2, 3, ..., N \tag{2.3}$$

Therefore, the vectors with the positions, velocities, and accelerations of all bodies of a planar multibody system with N moving bodies are given as follows:

$$\mathbf{q}^T = \begin{bmatrix} \mathbf{q}_1^T & \mathbf{q}_2^T & ... & \mathbf{q}_N^T \end{bmatrix}$$

$$\dot{\mathbf{q}}^T = \begin{bmatrix} \dot{\mathbf{q}}_1^T & \dot{\mathbf{q}}_2^T & ... & \dot{\mathbf{q}}_N^T \end{bmatrix}$$

$$\ddot{\mathbf{q}}^T = \begin{bmatrix} \ddot{\mathbf{q}}_1^T & \ddot{\mathbf{q}}_2^T & ... & \ddot{\mathbf{q}}_N^T \end{bmatrix}$$

It is possible to determine the position, velocity, and acceleration vectors of an arbitrary point on a body using the local body coordinate system attached to its center of mass. In Figure 4, considering the body Cartesian coordinate system ($G_i x_i y_i$) of body i, the local position vectors $\mathbf{s}_i^A$ and $\mathbf{s}_i^B$ of the points A and B can be written as

$$\mathbf{s}_i^A = \begin{bmatrix} x_i^A \\ y_i^A \end{bmatrix}, \quad \mathbf{s}_i^B = \begin{bmatrix} x_i^B \\ y_i^B \end{bmatrix} \tag{2.4}$$

Taking into account the body i rotated by an angle φ_i with respect to the fixed global coordinate system ($G_i x_o y_o$) with origin at the body's center of mass, as shown in

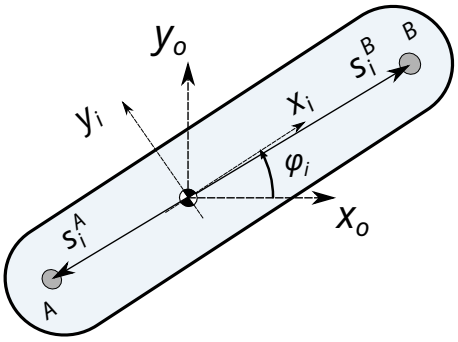

Figure 5 – Body i rotated by an angle φ with respect to a fixed global reference system.

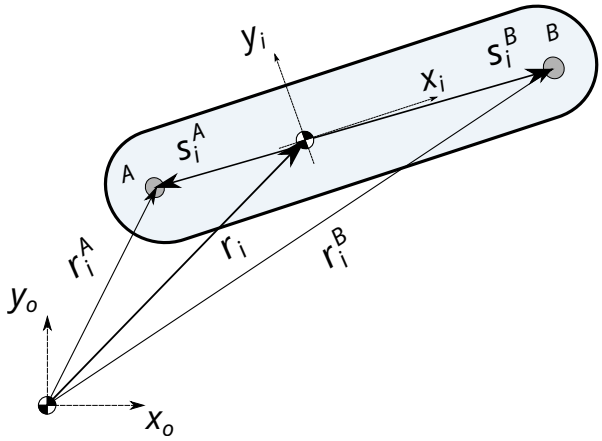

Figure 6 – Positions of body's i center of mass ($\mathbf{r}_i$) and points A and B with a fixed global reference system non-coincident to the local body reference system.

Figure 5, the global position vectors of the points A and B can be expressed through the following relation

$$\mathbf{r}_i^A = \mathbf{T}_i \mathbf{s}_i^A \tag{2.5}$$

$$\mathbf{r}_i^B = \mathbf{T}_i \mathbf{s}_i^B \tag{2.6}$$

where $\mathbf{T}_i$ is the rotation matrix of the body i relative to the global coordinate system, which is given as

$$\mathbf{T}_i = \begin{bmatrix} \cos(\varphi_i) & -\sin(\varphi_i) \\ \sin(\varphi_i) & \cos(\varphi_i) \end{bmatrix} \tag{2.7}$$

If the origin of the global coordinate system is located at a point other than the center of mass of the body, a vector connecting the origin of the global coordinate system to the center of mass of the body can be added to the relations 2.5 and 2.6. Figure 6 shows this situation. Therefore, the global position vectors of the points A and B can be obtained by the following relation

$$\mathbf{r}_i^A = \mathbf{r}_i + \mathbf{T}_i \mathbf{s}_i^A \tag{2.8}$$

$$\mathbf{r}_i^B = \mathbf{r}_i + \mathbf{T}_i \mathbf{s}_i^B \tag{2.9}$$

The velocity and acceleration vectors of points A and B can be determined by taking the first- and second-order time derivatives of the relations 2.8 and 2.9

$$\dot{\mathbf{r}}_i^A = \dot{\mathbf{r}}_i + \dot{\mathbf{T}}_i \dot{\varphi}_i \mathbf{s}_i^A \tag{2.10}$$

$$\dot{\mathbf{r}}_i^B = \dot{\mathbf{r}}_i + \dot{\mathbf{T}}_i \dot{\varphi}_i \mathbf{s}_i^B \tag{2.11}$$

$$\ddot{\mathbf{r}}_i^A = \ddot{\mathbf{r}}_i + (\ddot{\mathbf{T}}_i \dot{\varphi}_i^2 + \dot{\mathbf{T}}_i \ddot{\varphi}_i)\mathbf{s}_i^A \tag{2.12}$$

$$\ddot{\mathbf{r}}_i^B = \ddot{\mathbf{r}}_i + (\ddot{\mathbf{T}}_i \dot{\varphi}_i^2 + \dot{\mathbf{T}}_i \ddot{\varphi}_i)\mathbf{s}_i^B \tag{2.13}$$

where

$$\dot{\mathbf{T}}_i = \begin{bmatrix} -\sin(\varphi_i) & -\cos(\varphi_i) \\ \cos(\varphi_i) & -\sin(\varphi_i) \end{bmatrix} \tag{2.14}$$

$$\ddot{\mathbf{T}}_i = \begin{bmatrix} -\cos(\varphi_i) & \sin(\varphi_i) \\ -\sin(\varphi_i) & -\cos(\varphi_i) \end{bmatrix} \tag{2.15}$$

2.1.2 Constraint Equations

A kinematic pair imposes certain conditions on the relative motion between the two bodies it comprises. When these conditions are expressed in analytical form, they are called constraint equations. As a kinematic pair defines the relative movement between two bodies, the number of degrees of freedom of a kinematic pair is smaller than the total number of degrees of freedom of the two free bodies. Therefore, the constraint is any condition that reduces the number of degrees of freedom of a multibody system (NIKRAVESH, 1988; FLORES, 2008).

In a multibody system, the n_c constraint equations can be written in terms of the Cartesian coordinates of each body, where n_c is less than or equal to the system's degree of freedom. These constraint equations can be expressed in the vector form as (NIKRAVESH, 1988; FLORES, 2008):

$$\mathbf{\Phi}(\mathbf{q_1}, \mathbf{q_2}, \ldots, \mathbf{q_N}, t) = \mathbf{\Phi}(\mathbf{q}, t) = \mathbf{0} \tag{2.16}$$

The velocity and acceleration constraint equations can be derived by taking time derivatives of 2.16. Therefore, the velocity constraint equations can be written as

$$\dot{\mathbf{\Phi}} = \mathbf{J}\dot{\mathbf{q}} = -\mathbf{\Phi}_t = \mathbf{v} \tag{2.17}$$

where $\mathbf{J}$ is the *Jacobian* matrix obtained by differentiating the constraint equations with respect to the coordinates of the system, $\mathbf{J} = \partial\mathbf{\Phi}/\partial\mathbf{q}$, $\dot{\mathbf{q}}$ is the velocity vector and $\mathbf{v}$ is the vector containing the partial derivatives of $\mathbf{\Phi}$ with respect to time, $\partial\mathbf{\Phi}/\partial t$. The *Jacobian* matrix $\mathbf{J}$ can be represented in matrix format as follows:

$$\mathbf{J} = \begin{bmatrix} \frac{\partial \mathbf{\Phi}_1}{\partial q_1} & \frac{\partial \mathbf{\Phi}_1}{\partial q_2} & \cdots & \frac{\partial \mathbf{\Phi}_1}{\partial q_N} \\ \frac{\partial \mathbf{\Phi}_2}{\partial q_1} & \frac{\partial \mathbf{\Phi}_2}{\partial q_2} & \cdots & \frac{\partial \mathbf{\Phi}_2}{\partial q_N} \\ \vdots & \vdots & \ddots & \vdots \\ \frac{\partial \mathbf{\Phi}_{n_c}}{\partial q_1} & \frac{\partial \mathbf{\Phi}_{n_c}}{\partial q_2} & \cdots & \frac{\partial \mathbf{\Phi}_{n_c}}{\partial q_N} \end{bmatrix} \tag{2.18}$$

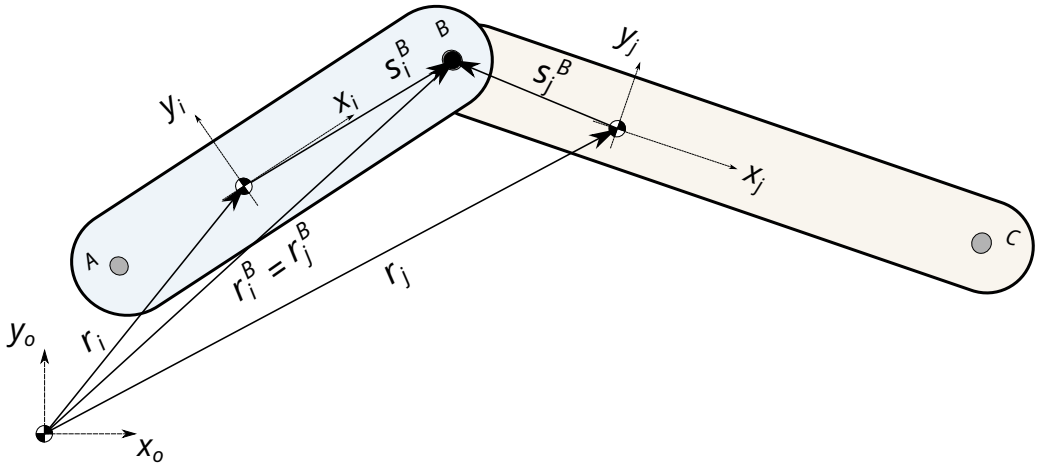

Figure 7 – Ideal planar revolute joints connecting the bodies i and j.

A second derivative of the constraint equations, Equation 2.16, with respect to time leads to the acceleration constraint equations (FLORES, 2008):

$$\ddot{\mathbf{\Phi}} = \mathbf{J}\ddot{\mathbf{q}} = -\frac{\partial(\mathbf{J}\dot{\mathbf{q}})}{\partial \mathbf{q}}\dot{\mathbf{q}} - 2\mathbf{\Phi}_{qt}\dot{\mathbf{q}} - \mathbf{\Phi}_{tt} = \gamma \tag{2.19}$$

where $\ddot{\mathbf{q}}$ is the acceleration vector, and γ is the vector of the terms of quadratic velocities that are exclusively a function of velocity, position and time. In the case of scleronomic constraints, that is, when $\mathbf{\Phi}$ is not explicitly dependent on time, the terms $\mathbf{\Phi}_t$ in Equation 2.17, and $\mathbf{\Phi}_{qt}$ and $\mathbf{\Phi}_{tt}$ in Equation 2.19 vanish (FLORES, 2008).

2.1.3 Revolute Joints

Ideal Revolute Joints

A revolute joint connects two bodies through a common point. A revolute joint eliminates two DoFs of the linked bodies in a plane motion. Figure 7 illustrates the connection between bodies i and j through a revolute joint. The variables s_i^B and s_j^A contain the body coordinates of the connection points B and A relative to the centers of mass of the bodies i and j, respectively.

Through a revolute joint, as shown in Figure 7, it is possible to obtain a relation between the position vectors of the point common to both connected bodies. If the revolute joint perfectly connects the bodies, the following constraint equation is defined

$$\mathbf{r}_i^B = \mathbf{r}_j^B \tag{2.20}$$

Developing the relation 2.20, we obtain:

$$\mathbf{r}_i + \mathbf{T}_i\mathbf{s}_i^B - \mathbf{r}_j - \mathbf{T}_j\mathbf{s}_j^B = \mathbf{0} \tag{2.21}$$

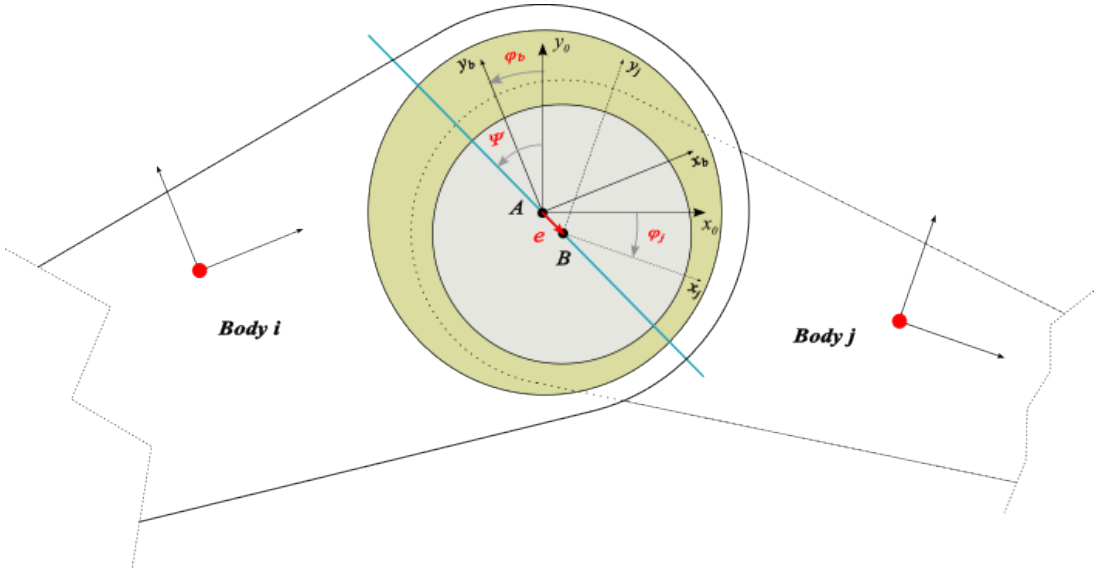

Figure 8 – Revolute clearance joint connecting two bodies in a planar system.

Source: adapted from Flores, Ambrósio and Claro (2004).

where $\mathbf{r}_i$ and $\mathbf{r}_j$ are, respectively, the position vectors of the centers of mass of the bodies i and j with respect to the global coordinate system, $\mathbf{T}_i$ and $\mathbf{T}_j$ are the rotation matrices of the bodies i and j relative to the global coordinate system, and $\mathbf{s}_i^B$ and $\mathbf{s}_j^B$ are the local position vectors of the connection point B in the bodies coordinate systems. In the specific case of a single revolute joint in plane motion, as shown in Figure 7, two scalar constraint equations are established in terms of the global Cartesian coordinates x and y.

Similarly, the velocity and acceleration constraint equations are obtained by taking the first and second derivatives of the constraint equations with respect to time. Accordingly, from Equation 2.21

$$\dot{\mathbf{r}}_i + \dot{\mathbf{T}}_i \dot{\varphi}_i \mathbf{s}_i^B - \dot{\mathbf{r}}_j - \dot{\mathbf{T}}_j \dot{\varphi}_j \mathbf{s}_j^A = \mathbf{0} \tag{2.22}$$

$$\ddot{\mathbf{r}}_i + (\ddot{\mathbf{T}}_i \dot{\varphi}_i^2 + \dot{\mathbf{T}}_i \ddot{\varphi}_i)\mathbf{s}_i^B - \ddot{\mathbf{r}}_j - (\ddot{\mathbf{T}}_j \dot{\varphi}_j^2 + \dot{\mathbf{T}}_j \ddot{\varphi}_j)\mathbf{s}_j^A = \mathbf{0} \tag{2.23}$$

Clearance Revolute Joints

The clearance revolute joints are represented by the eccentricity vector and the angle formed by itself and the axis x_0 that is related to the global Cartesian coordinate reference. The bearing coordinate system has the same angular orientation φ_b of the local Cartesian coordinate reference located in the CM of the body j, where k is the bearing identification index. Figure 8 presents, for a planar system, the example of a revolute joint with clearance that connects two bodies and highlights the eccentricity parameters for a connection of this type.

As can be seen in Figure 8, the connection point A of the body j is considered the center of the bearing, and the connection point B of the body i is considered the center of the journal (pin). The clearance revolute joint allows both of these points to

move independently in relation to each other, which does not occur in a joint considered ideal or perfect. This movement depends on several factors, such as the characteristics of the bodies in the system, their operational condition, and the forces involved. The displacement between these points, the center of the bearing and the center of the shaft, will result in a vector $\mathbf{e}$ that represents the distance between these points in the Cartesian coordinate of the global reference system. This vector has a magnitude e and an angle θ ($\theta = \Psi - 90$) that define its orientation.

$$\mathbf{e} = \mathbf{r}_i^B - \mathbf{r}_j^A \tag{2.24}$$

The magnitude of the eccentricity vector e is evaluated as:

$$e = \sqrt{\mathbf{e}^T \mathbf{e}} \tag{2.25}$$

$\mathbf{e}^T$ denotes the transpose of the vector $\mathbf{e}$.

The unit normal vector of the bearing k $\mathbf{n}_k$, with the coordinates given in the global Cartesian coordinate reference $(x_o y_o)$ is defined as:

$$\mathbf{n} = \frac{\mathbf{e}}{e} \tag{2.26}$$

The first time derivative, that is, the variation of the vector eccentricity in time $\dot{\mathbf{e}}$ can be obtained by the following relation:

$$\dot{\mathbf{e}} = \dot{\mathbf{r}}_i^B - \dot{\mathbf{r}}_j^A \tag{2.27}$$

The direction of the unit vector $\mathbf{n}$ coincides with the line connecting the bearing and shaft centers, in the radial direction. The tangential direction is obtained by rotating the vector $\mathbf{n}$ clockwise by 90 degrees. Dividing the modulus of the eccentricity vector e by the radial clearance c, we obtain the eccentricity relation ϵ.

$$\epsilon = \frac{e}{c} \tag{2.28}$$

The rate of eccentricity change over time $\dot{\epsilon}$ is obtained by differentiating Equation 2.28 with respect to time and dividing the result by radial clearance.

$$\dot{\epsilon} = \frac{\dot{e}}{c} \tag{2.29}$$

The components at coordinates x and y of the unit normal vector $\mathbf{n}$ are defined as a function of the orientation angle θ.

$$\begin{bmatrix} n_x \\ n_y \end{bmatrix} = \begin{bmatrix} cos(\theta) \\ sin(\theta) \end{bmatrix} \tag{2.30}$$

Equation 2.30 can be rewritten as:

$$\theta = arctan(\frac{n_y}{n_x}) \tag{2.31}$$

The terms of the vectors $\mathbf{e}$ and $\dot{\mathbf{e}}$, from the Equations 2.24 and 2.27, respectively, related to the global Cartesian coordinates, are used as dynamic input data parameters to obtain the hydrodynamic and contact pressures.

2.1.4 Motion Equations System

Dynamic analysis seeks to study the movement of bodies in a given dynamic system over a period of time. This analysis uses position and velocity restriction equations derived from kinematic analysis and mass data and moments of inertia of the bodies, in addition to prior knowledge of the external forces and moments that act on the system.

In dynamic analysis, a unique solution is obtained when the constraint equations are considered simultaneously with the differential equations of motion for a suitable set of initial conditions.

For a system of unrestricted bodies, the dynamic formulation can be given in such a way that the loads (forces and moments) acting on the system are equal to the product of the inertia matrix of the bodies by the acceleration vector. Equation 2.32 presents this relationship for unrestricted bodies.

$$\mathbf{M}\ddot{q} = \mathbf{f} \tag{2.32}$$

In the case of a system of constrained bodies, the formulation presents the reaction forces at the joints $\mathbf{f^c}$, so that:

$$\mathbf{M}\ddot{q} = \mathbf{f} + \mathbf{f^c} \tag{2.33}$$

According to Nikravesh (1988) it is possible to obtain a relationship between the reaction forces and the restraining equations if: (1) a coordinate eigenvector is defined, and (2) the restraining forces are established in the same coordinate system of the coordinate vector. Assuming that the joints are frictionless and that the work done by the restraining forces in an infinitesimal virtual displacement is zero, we arrive at the following relationship:

$$\mathbf{f^c} = -\mathbf{J}^T\mathbf{\Lambda} \tag{2.34}$$

Associating Equations 2.33 and 2.34, we have:

$$\mathbf{M}\ddot{q} + \mathbf{J}^T\mathbf{\Lambda} = \mathbf{f} \tag{2.35}$$

Using Equations 2.19 and 2.35 together, the dynamic formulation can be represented in the following matrix form (NIKRAVESH, 1988; FLORES, 2008):

$$\begin{bmatrix} \mathbf{M} & \mathbf{J}^T \\ \mathbf{J}^T & \mathbf{0} \end{bmatrix} \begin{bmatrix} \ddot{\mathbf{q}} \\ \mathbf{\Lambda} \end{bmatrix} = \begin{bmatrix} \mathbf{f} \\ \gamma \end{bmatrix} \tag{2.36}$$

Mass and Inertia Matrix

The matrix of masses and inertia moments of the body of the system has dimension λ N x λN, where λ is equal to 3, for a planar motion and equal to 6, for a movement in a three-dimensional space. λ represents all the possibilities of linear and angular movement of each body; N is the number of moving bodies in the system; $\mathbf{J}$ is the Jacobian matrix, whose dimension is λ n_c x λN, where n_c is the number of constraint equations; $\mathbf{J^T}$ is the transpose of the Jacobian matrix; $\ddot{\mathbf{q}}$ is the vector of generalized accelerations of the system; $\mathbf{\Lambda}$ is the Lagrange multiplier vector representing the reaction forces in ideal joints); $\mathbf{f}$ is the vector containing the sum of forces and moments acting on the system; and γ is the vector containing the quadratic terms of the angular velocities.

The mass matrix $\mathbf{M}$ contains the inertia properties of the bodies in the system related to their respective centers of mass. In a planar (2D) system, the matrix $\mathbf{M_i}$ of the body i is given by:

$$\mathbf{M}_i = \begin{bmatrix} I_i & 0 & 0 \\ 0 & m_i & 0 \\ 0 & 0 & m_i \end{bmatrix} \tag{2.37}$$

where m_i and I_i are, respectively, the mass and the inertia moment of the body i with respect to the axis that passes through its center of mass and is perpendicular to the motion plane.

The matrix of inertia properties of the system $\mathbf{M}$ is formed by the set of matrices $\mathbf{M_i}$ of each element, which are organized and assembled in a diagonal line, one after the other, contemplating the matrices of inertia properties of all bodies.

$$\mathbf{M} = \begin{bmatrix} \mathbf{M}_1 & \mathbf{0} & \cdots & 0 \\ \mathbf{0} & \mathbf{M}_2 & \cdots & 0 \\ \vdots & \vdots & \ddots & \vdots \\ \mathbf{0} & \mathbf{0} & \cdots & \mathbf{M}_N \end{bmatrix} \tag{2.38}$$

Loads Vectors and Joint Reaction Forces

The load vector $\mathbf{f}$, represents the sum of all efforts (forces and moments) actuating in the CM of the bodies in the system, including all external loads and those arising in the clearance revolute joints. The vector $\mathbf{f}$ has dimension λN x 1.

The vector $\mathbf{f}$ can be divided into other vectors containing specific efforts: gravitational field loads $\mathbf{f}_g$, where forces related to gravitational acceleration are considered; and dynamic efforts $\mathbf{f}_d$, where the forces and moments applied to the bodies vary as a function of time, being, however, known in advance.

When considering a system with one or more bodies connected by clearance joints, a loading vector $\mathbf{f}_j$ is also included, which contains the hydrodynamic and contact forces

actuating on the elements connected by such joints. These loads are obtained through the models that are applied to each of the clearance joints and result in significant differences in the dynamic behavior of the system. These forces are particularly dynamic and depend on the evolution of the dynamic behavior of the system. These efforts are obtained in each time step because they depend on eccentricity variables that vary according to the position, velocity, and acceleration of the system.

$$\mathbf{f} = \mathbf{f}_g + \mathbf{f}_d + \mathbf{f}_j \tag{2.39}$$

The reaction forces in the joint can be expressed in terms of the *Jacobian* matrix of constraint equations $\mathbf{J}$ and the Lagrange multiplier vector, as presented in equation 2.34 (NIKRAVESH, 1988; FLORES, 2008).

$\mathbf{\Lambda}$ is the vector physically related to the reaction forces generated between the interconnected elements by the kinematic joints considered ideal or perfect.

Baumgarte Stabilization Method

The dynamic motion equation system, Equation 2.36, is solved for $\ddot{\mathbf{q}}$ and $\mathbf{\Lambda}$. Then, at each integration time step, the acceleration vector $\ddot{\mathbf{q}}$ and the velocity vector $\dot{\mathbf{q}}$, are integrated to obtain, respectively, the velocities and positions of the system for the next time step. This procedure is repeated until the final analysis time is reached.

Variables of the equation that governs the dynamic behavior of the system are not related to the position and velocity constraint equations, even though the constraint equations are non-linear. Thus, as the integration time progresses, the error in the calculated values for the kinematic parameters accumulates, and the constraints violations increase. Therefore, the results produced may be unacceptable and in order to avoid it, the integration method requires the use of a constraint stabilization technique, especially for long simulations. These errors are due to the finite precision of numerical methodologies and position and velocity constraint equations that do not appear anywhere in the solution procedure. Methods capable of eliminating errors in the restriction or velocity equations or, at least, keeping such errors under control must be implemented (FLORES, 2008).

Although the initial conditions guarantee non-violation of the constraint equations in position and velocity, during the course of numerical integration, numerical errors do not satisfy the constraint equations. The effect of these errors increases with time. Therefore, the constant distances are no longer constant and the points of the same element progressively approach or move away from their original position (FLORES, 2008; FLORES et al., 2006).

Several stabilization methods have been studied and proposed to avoid violating the restriction equations during the integration procedure. Some of them are the Baumgarte

Stabilization Method, the coordinate partitioning method, and the augmented Lagrangian formulation.

Flores (2008) cites the stabilization method of Baumgarte (1972), given its simplicity and ease of computational implementation, as the most popular and attractive technique to control restriction violations. He considers, however, that this method does not solve all possible numerical difficulties, such as, for example, those that arise close to kinematic singularities, and there is no specific procedure or detailed explanations about the choice of *feedback* parameters, α and β which can make your definition ambiguous. Choosing these coefficients usually involves trial and error (BAUMGARTE, 1972).

The Baumgarte Stabilization Method replaces the differential equation of the acceleration constraint equation, Equation 2.19, with the following expression:

$$\ddot{\mathbf{\Phi}} + 2\alpha\dot{\mathbf{\Phi}} + \beta^2\mathbf{\Phi} \tag{2.40}$$

where $\ddot{\mathbf{\Phi}}$, $\dot{\mathbf{\Phi}}$ and $\mathbf{\Phi}$ represent, respectively, the constraint equations for acceleration, velocity, and position of bodies in the dynamic system.

Flores, Ambrósio and Claro; Flores et al. use the stabilization method of Baumgarte (1972) to avoid violating the restriction conditions in the integration process, so that the vector γ, on the right side of the equality of Equation 2.19, is replaced by the following expression:

$$\gamma - 2\alpha\dot{\mathbf{\Phi}} - \beta^2\mathbf{\Phi} \tag{2.41}$$

where α and β are constants for the stabilization method; $\mathbf{\Phi}$ and $\dot{\mathbf{\Phi}}$ are, respectively, the vector of constraint equations and the vector of velocity equations.

Using Baumgarte's stabilization method (BAUMGARTE, 1972), the vector on the right side of Equation 2.36 will also depend on the terms of position and velocity, derived from the vector of constraint equations. In this context, including Baumgarte's stabilization method, the dynamic analysis can be expressed in the matrix form as follows (FLORES, 2008):

$$\begin{bmatrix} \mathbf{M} & \mathbf{J}^{\mathbf{T}} \\ \mathbf{J}^{\mathbf{T}} & \mathbf{0} \end{bmatrix} \begin{bmatrix} \ddot{\mathbf{q}} \\ \mathbf{\Lambda} \end{bmatrix} = \begin{bmatrix} \mathbf{f} \\ \gamma - 2\alpha\dot{\mathbf{\Phi}} - \beta^2\mathbf{\Phi} \end{bmatrix} \tag{2.42}$$

2.2 Mechanism Model

2.2.1 Crank–Connecting Rod–Slider Mechanism

The crank–connecting rod–slider mechanism with clearance joints considered in this work consists of four bodies connected by joints: a fixed block and three moving bodies (crank, connecting rod, and slider). Revolute joints link the first three bodies, and the last one is connected to the block by a horizontal translation joint, which we assumed to

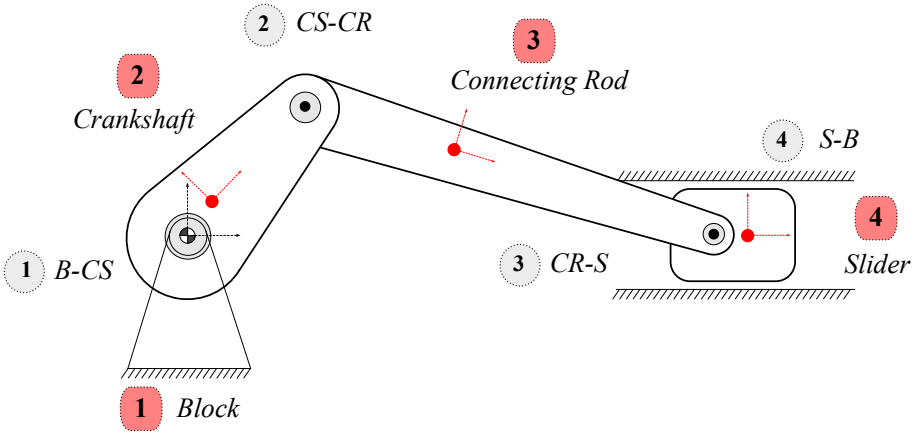

Figure 9 – Crankshaft–connecting rod–slider mechanism model.

Table 2 – Identification of the mechanism joints. RJ and TJ denote revolute and translational joint, respectively.

Number	Type	Name	ID
1	RJ	Block-Crankshaft	B–CS
2	RJ	Crankshaft-Connecting Rod	CS–CR
3	RJ	Connecting Rod-Slider	CR–S
4	TJ	Slider-Block	S–B

Table 3 – Identification of the mechanism bodies.

Number	Name	ID
1	Block	B
2	Crankshaft	CS
3	Connecting Rod	CR
4	Slider	S

be a perfect joint in this study. The global reference frame is fixed at the center of the block–crankshaft joint. Figure 9 illustrates the mechanism model with its corresponding bodies and joints. Tables 2 and 3 present the identification number and the names given to the bodies and joints of the mechanism.

Considering the connection of the bodies, the following connectivity matrix ($\mathbf{V}$) can be constructed, where each column represents a joint connecting the bodies in its rows.

$$\mathbf{V} = \begin{bmatrix} 1 & 2 & 3 & 4 \\ 2 & 3 & 4 & 1 \end{bmatrix}. \tag{2.43}$$

Each body has a local coordinate vector $\mathbf{s}_i^k$ defined from the center of mass of the body i to the connection point of the joint k. This vector has two Cartesian coordinates (x, y) that specify the position of the joint connection point relative to the body center of mass. Using the connectivity matrix, it is possible to construct the coordinate matrix ($\mathbf{S}$)

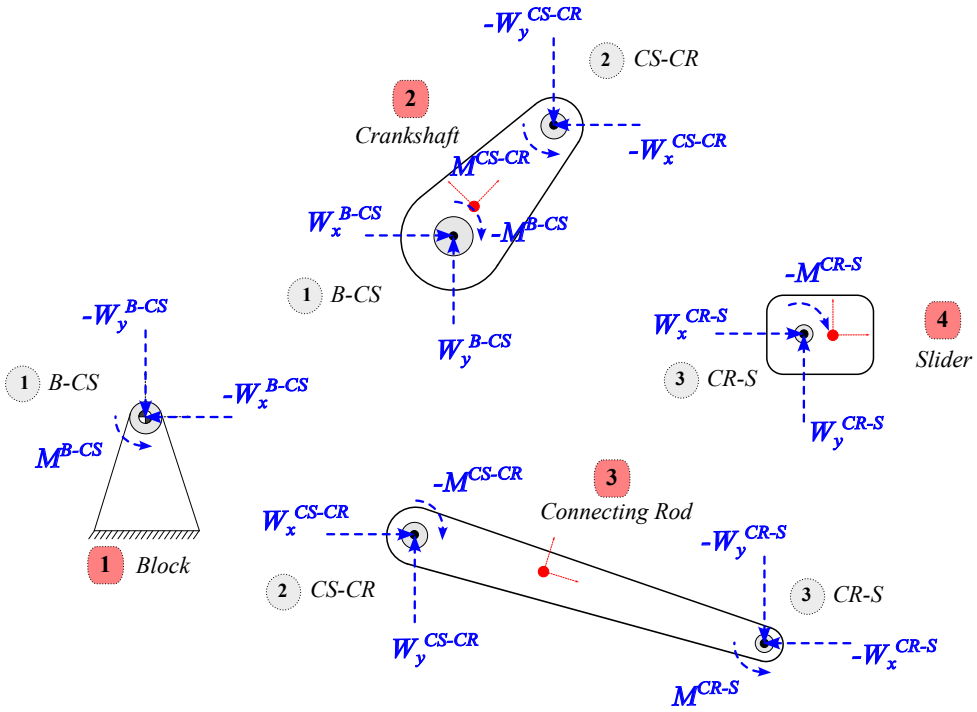

Figure 10 – Free-body diagrams of the bodies that compose the crankshaft–connecting rod–slider mechanism.

as follows

$$\mathbf{S} = \begin{bmatrix} \mathbf{s}_1^1 & \mathbf{s}_2^2 & \mathbf{s}_3^3 & \mathbf{s}_4^4 \\ \mathbf{s}_2^1 & \mathbf{s}_3^2 & \mathbf{s}_4^3 & \mathbf{s}_1^4 \end{bmatrix}. \tag{2.44}$$

2.2.2 Free-Body Diagrams and Joint Forces

Figure 10 shows the free-body diagrams with the forces and moments acting on the mechanism bodies and joints. The body weights were ignored from the analysis because their magnitudes are much smaller than the joint loads. Therefore, the load vector of the system can be written as

$$\mathbf{f}^T = \left[\mathbf{f}_{CS}^T, \quad \mathbf{f}_{CR}^T, \quad \mathbf{f}_S^T\right], \tag{2.45}$$

where

$$\mathbf{f}_{CS}^T = \left[M^{B-CS} + M^{CS-CR}, \quad W_x^{B-CS} - W_x^{CS-CR}, \quad W_y^{B-CS} - W_y^{CS-CR}\right], \tag{2.46a}$$

$$\mathbf{f}_{CR}^T = \left[-M^{CS-CR} + M^{CR-S}, \quad W_x^{CS-CR} - W_x^{CR-S}, \quad W_y^{CS-CR} - W_y^{CR-S}\right], \tag{2.46b}$$

$$\mathbf{f}_S^T = \left[-M^{CR-S}, \quad W_x^{CR-S}, \quad W_y^{CR-S}\right]. \tag{2.46c}$$

The load vectors in Eqs. 2.46 include the forces and moments on each body, whose components are with respect to the global reference system. The joint loads result from the hydrodynamic and asperity contact effects at the interface of these connecting components.

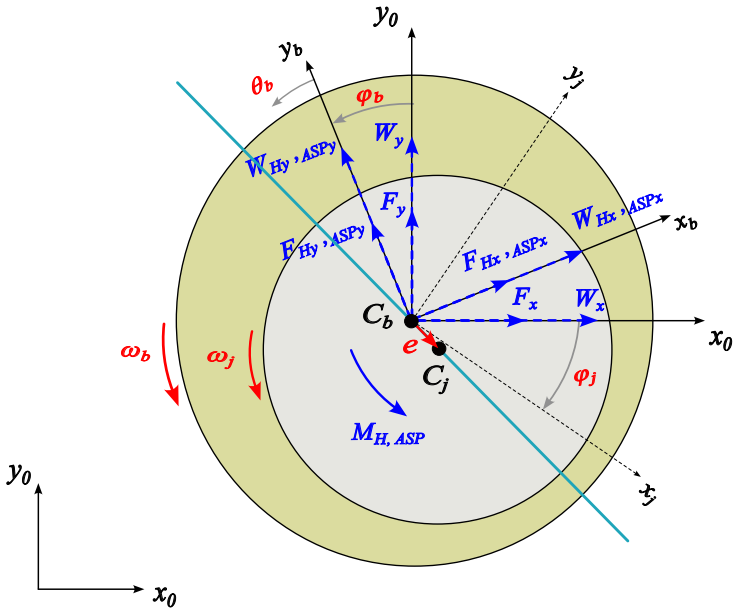

Figure 11 – Hydrodynamic and asperity contact forces and moments acting on a journal bearing joint.

2.2.3 Journal Bearing Joint

In this work, the lubricated revolute clearance joints B–CS, CS–CR and CR–S are modeled as plain journal bearings. Figure 11 illustrates the hydrodynamic and asperity contact forces ($\mathbf{W}_{H,ASP}$ and $\mathbf{F}_{H,ASP}$) and moments ($\mathbf{M}_{H,ASP}$ and $\mathbf{M}_{H,ASP}$) acting on a journal bearing joint represented in the local bearing reference system $C_b x_b y_b z_b$. $\mathbf{M}_f$ indicates the binary moment in the body as a result of the force that rises in the clearance joint related to that body. As this local reference system is attached to the body, its position and orientation change relative to the global reference system $Ox_o y_o z_o$. Therefore, the following transformation should be applied to obtain the components of the hydrodynamic and asperity contact loads in the global reference system.

$$\mathbf{W} = [\mathbf{T}(\varphi_b)]\,(\mathbf{W}_H + \mathbf{F}_H + \mathbf{W}_{ASP} + \mathbf{F}_{ASP}) \tag{2.47a}$$

$$\mathbf{M} = \mathbf{M}_H + \mathbf{M}_{ASP} + \mathbf{M}_f \tag{2.47b}$$

The hydrodynamic and asperity contact forces and moments on the joint are calculated by integrating the hydrodynamic and asperity contact pressures and shear stresses on the lubrication domain of the joint. Details about the calculation of the joint loads from the corresponding pressures and shear stresses are presented in the Annexes of (PROFITO, 2015). The following sections present the models used in this work for predicting the hydrodynamic and asperity contact pressures on the joint interface in more detail.

2.3 Hydrodynamic Model

2.3.1 Lubrication Regimes

Journal bearings are mechanical components that usually operate with a lubrication film sufficiently thick to ensure full separation of the journal and bearing surfaces, preventing inefficiencies, surface damage and failure. However, in more extreme conditions (e.g. high thermomechanical loads and low-viscosity oils), the lubricating film tends to become thinner, and the contact between the surfaces is more likely, leading to increased wear and reduced service life.

A useful concept for understanding the role of different lubrication regimes is the Stribeck curve, as shown in Figure 12. Historically, the Stribeck curve was widely disseminated from systematic experiments conducted by Stribeck that showed the behavior of friction in radial plain bearings under different operating conditions (HAMROCK; SCHMID; JACOBSON, 2004).

The Stribeck curve is a chart of the coefficient of friction versus the so-called Hersey number, a dimensionless parameter that represents the ratio of the product of fluid viscosity and velocity to the applied load under steady-state conditions. The Stribeck curve distinguishes three lubrication regimes: boundary, mixed, and hydrodynamic regimes. The coefficient of friction reaches its minimum at the transition from the mixed to the hydrodynamic regime. Thus, theoretically, radial bearings should operate in this transition; however, wear occurs when metal-to-metal contact between the surfaces appears in the mixed to the boundary lubrication regimes (ALLMAIER; OFFNER, 2016).

Given the changing parameters and operating conditions promoted by the current technology trends, a bearing previously designed to operate in hydrodynamic lubrication may actually experience mixed lubrication, where the hydrodynamic pressures within the lubricating film and the rough contact pressures arising from the interaction of surface asperities share the total applied load. Figure 13 illustrates the surface separation conditions for each lubrication regime. For instance, during the bearing start-up transient (predominance of boundary and mixed lubrication regimes), the magnitude of applied loads, contact geometry, material properties and topographical characteristics of the surfaces in contact mainly determine the thickness of the lubricating film. In this sense, using rough contact models that better describe the interaction between surface asperities is very important for analysing friction and wear and their evolution over their lifetime. Under these conditions, of particular importance is the determination of the real contact area (which is only a fraction of the nominal contact area) and the normal load capacity supported by the asperities as a function of the average separation between the surfaces (CHANG; ETSION; BOGY, 1987).

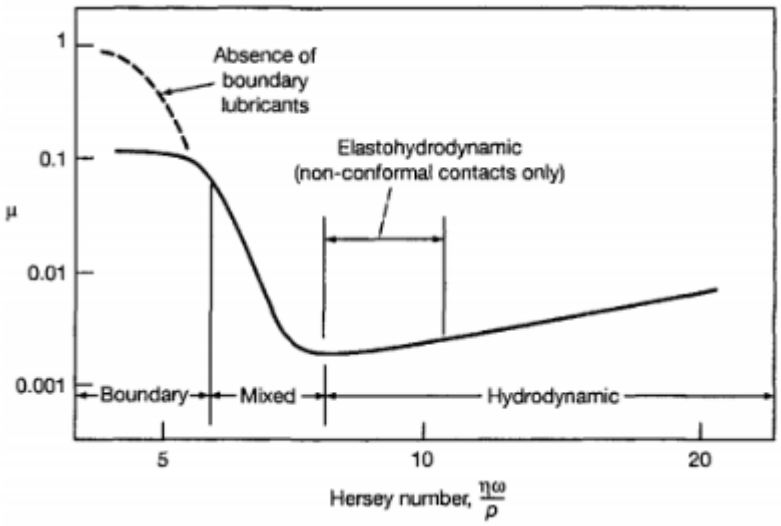

Figure 12 – Typical conformal contact Stribeck curve, relating the Hursey number to the coefficient of friction.

Source: Hamrock, Schmid and Jacobson (2004).

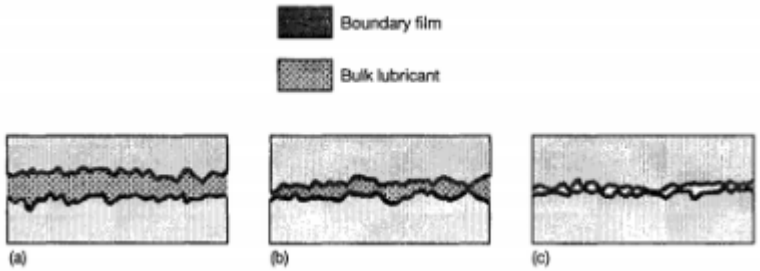

Figure 13 – Lubricating film conditions in different lubrication regimes: (a) hydrodynamic lubrication with surfaces completely separated by a fluid film; (b) mixed or partial lubrication and (c) boundary lubrication.

Source: Hamrock, Schmid and Jacobson, (2004).

2.3.2 Journal Bearing Model

Figure 14 shows a schematic of the journal bearing model adopted in this work, illustrating the pertinent local reference systems and the main geometric and operational parameters. The local bearing reference system ($C_b x_b y_b z_b$) has the same orientation as the body reference system that holds it.

Reynolds Equation

In 1886, Osborne Reynolds derived a dimension-reduced partial differential equation from the Navier Stokes and continuity equations for calculating the pressure distribution in incompressible fluid film lubricated bearings. In addition to providing a theoretical basis for thin film lubrication, Reynolds also directly compared the proposed theory with the experimental results obtained by Tower (1883) (HAMROCK; SCHMID; JACOBSON, 2004). The principal hypotheses assumed in the pioneered derivation of the Reynolds

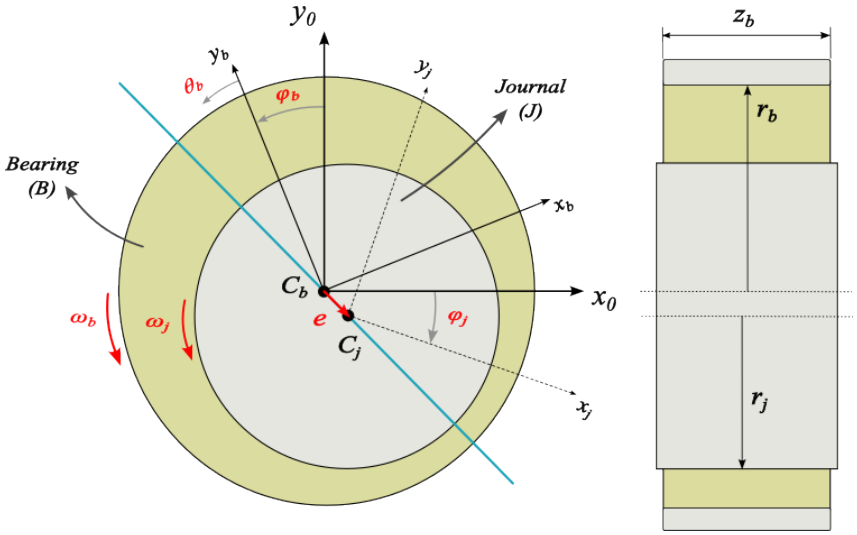

Figure 14 – Journal Bearing model.

equation are: the flow is laminar, the lubricant behaves as a Newtonian fluid, the pressure is constant across the film thickness, and the fluid density and viscosity are constant throughout the lubricant film.

As mentioned in Section 2.2.3, the lubricated revolute clearance joints of the mechanism studied in this work are modeled as rigid plain journal bearings. The hydrodynamic pressure generated within the lubricant film at the joint interface is calculated using the following transient isothermal Reynolds equation with the Elrod-Adams $p-\theta$ mass-conserving cavitation model (FRENê et al., 1997 *apud* PROFITO, 2015)

$$\frac{\partial}{\partial x}\left(\frac{\rho h^3}{12\mu}\frac{\partial p_{_H}}{\partial x}\right)+\frac{\partial}{\partial z}\left(\frac{\rho h^3}{12\mu}\frac{\partial p_{_H}}{\partial z}\right)=\frac{\partial}{\partial x}\left[\frac{\rho(\omega_j+\omega_b)Rh\theta}{2}\right]+\frac{\partial(\rho\theta h)}{\partial t}, \tag{2.48}$$

with the complementarity boundary conditions for cavitation

$$(p_{_H}-p_{cav})\cdot(1-\theta)=0 \quad \Rightarrow \quad \begin{cases} p_{_H}>p_{cav}, \ \theta=1 & \text{in } \mathcal{D}^+ \\ p_{_H}=p_{cav}, \ 0\leq\theta<1 & \text{in } \mathcal{D}^- \\ p_{_H}=p_{cav} & \text{on } \mathcal{C}. \end{cases} \tag{2.49}$$

In the above equations, $p_{_H}(x,z)$ is the hydrodynamic pressure, $\theta(x,z)$ is the lubricant film fraction that represents the fluid saturation in the cavitation regions, $h(x,z)$ is the lubricant film thickness, ρ and μ are the lubricant density and dynamic viscosity, ω_j and ω_b are the journal and bearing rotational speeds, R is the nominal bearing radius, and $x=R\theta_b$ and z are the corresponding bearing circumferential and axial coordinates of the local coordinate system $Oxyz$ attached to the bearing surface where the Reynolds equation is described. Additionally, p_{cav} is the limit cavitation pressure, $\mathcal{D}^+$ and $\mathcal{D}^-$ are the pressured and cavitation regions, respectively, and $\mathcal{C}$ is the cavitation boundaries.

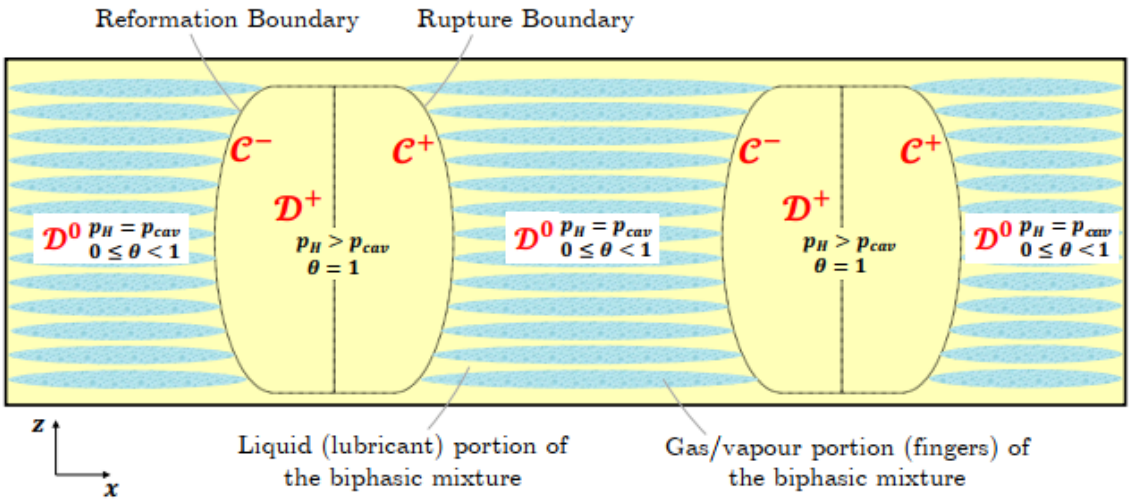

Figure 15 – Schematic of the cavitation regions and boundaries on an unwrapped journal bearing domain. Pressured regions (D^+) are separated by intermediate cavitation zones (D^0) bounded by their respective reformation (C^-) and rupture boundaries (C^+)

Source: from Profito (2015).

The lubricant film thickness of a plain journal bearing can be expressed in the local coordinate system $Oxyz$ as

$$h\left(x,z\right) = c - Y_r \cos\theta_b + X_r \sin\theta_b, \tag{2.50}$$

where c is the bearing nominal clearance, and X_r and Y_r are the rigid body displacements of the journal relative to the bearing in the $C_b x_b$ and $C_b y_b$ directions of the local bearing reference system $C_b x_b y_b z_b$.

Fluid Film Cavitation

Since lubricants are unlikely to withstand high tensile stresses, the lubricant film is broken down whenever the fluid pressure reaches values below the saturation pressure of the gases dissolved into the oil (gaseous cavitation) and/or the vapour pressure of the lubricant (vapour cavitation). This rupture of the fluid film leads to the growth of unpressurized zones (cavitated zones) that are filled with a biphasic mixture of liquid (lubricant) and gases/vapour (PROFITO, 2015).

The cavitation (D^0) and pressurized (D^+) regions on a lubricated domain are illustrated schematically in Figure 15, which also shows the cavitation boundaries that separate both regions. These boundaries can be of two types: (1) rupture boundary (C^+), where cavitation initiates with fluid film rupture; and (2) reformation boundary (C^-) where the lubricant film begins to be reestablished due to the gradual rise in the hydrodynamic pressures (PROFITO, 2015).

Several formulations exist to model the cavitation phenomenon in lubricated contacts mathematically, such as the Gumbel (or half-Sommerfeld) model, Swift-Steiber (or Reynolds) model, and Jakobsson-Floberg-Olsson (JFO) model. The JFO approach is the most common formulation used for fluid film cavitation modeling that complies with the mass-conservation principle over the lubricated domain.

Jakobsson-Floberg-Olsson (JFO) proposed a set of complementarity boundary conditions that enforce the mass conservation of the lubricant flow throughout the lubricated domain, including in the rupture and reformation cavitation boundaries. The main assumptions of the JFO model are listed as follows Profito (PROFITO, 2015).:

- In the cavitated regions, the fluid pressure in the biphasic mixture remains constant and equal to the limit pressure (p_{cav}) associated with the type of cavitation considered (gaseous or vapour cavitation).
- In the cavitated regions, the liquid phase (lubricant) of the mixture flows through in-between gases/vapour fingers that span entirely across the film thickness (Figure 15).
- At the cavitation boundaries, the mass conservation is enforced by imposing complementarity boundary conditions that must be used concomitantly with the solution of the Reynolds equation.

Using the JFO complementarity boundary conditions is not straightforward in practice once the cavitation boundaries are unknown *a priori*. Elrod and Adams (1974, 1981) proposed modifications in the Reynolds equation to accomplish the JFO conditions automatically. The main concept of the so-called $p-\theta$ model presented by Elrod and Adams is based on the definition of the new lubricant film fraction variable θ which is aimed to account for the existence of the cavitation biphasic mixture directly into the Reynolds equation (PROFITO, 2015).

The complementarity boundary conditions for cavitation imposed by the Elrod-Adams $p-\theta$ mass-conserving cavitation model is mathematically represented by Eq. 2.49. Accordingly, in the pressured regions (D^+), where the hydrodynamic pressures are higher than the limit cavitation pressure ($p_{_H} > p_{cav}$), the fluid film develops completely ($\theta = 1$). In the cavitation zones, the fluid pressures remain constant ($p_{_H} = p_{cav}$), and the lubricant film is broken ($0 \leq \theta < 1$).

Lubricant Shear Stresses

The variation of the lubricant viscosity within the pressured and cavitation regions relative to its nominal value can also be expressed as a function of the film fraction θ as

(PROFITO, 2015)

$$\mu \quad \rightarrow \quad \mu g(\theta), \tag{2.51}$$

where $g(\theta)$ is a weighting function that determines how the dynamic viscosity of the lubricant changes in terms of the distribution of the film fraction. Such a viscosity variation must be considered in the calculation of shear stresses. Linear correlation between viscosity and fluid film fraction is assumed within cavitation zones, *i.e.* $g(\theta) = \theta$. Therefore, the modified expressions of the lubricant shear stresses on the journal and bearing surfaces in the circumferential direction become

$$\tau_{\substack{j \\ H_x}} = \frac{h}{2}\frac{\partial p_{\substack{H}}}{\partial x} + \frac{\mu\theta(\omega_j - \omega_b)R}{h}, \tag{2.52a}$$

$$\tau_{\substack{b \\ H_x}} = -\frac{h}{2}\frac{\partial p_{\substack{H}}}{\partial x} + \frac{\mu\theta(\omega_j - \omega_b)R}{h}. \tag{2.52b}$$

2.4 Asperity Contact Models

According to Liu, Wang and Lin (1999), the contact between asperities is the main characteristic of the mixed lubrication regime. Because of this, the continuous flow of lubricant between the surfaces is stopped, and the applied load is supported by the fluid pressure and the asperity contact pressure together. Investigations of contact and interaction between surfaces are essential for mixed lubrication studies (LIU; WANG; LIN, 1999).

According to Sander, Allmaier and Priebsch (2006), to design more efficient radial bearings, a detailed simulation approach is required, which is adequate to describe the complex behavior of mixed elastohydrodynamic lubrication. In this sense, it is important to address some contact models from which the contact efforts in gap joints are extracted and which will be included in the dynamic simulation of the system.

An accurate characterization of the contact between rough surfaces is important for analyzing tribological problems such as sealing, friction, and wear. Contact parameters are largely important for analyzing these problems in a given mechanical system. Some of these parameters of interest are: real contact area, which is only a fraction of the nominal or apparent contact area, surface deflections, contact pressures, and the stresses that develop within the solids resulting from loading requests.

In the next sections we present the mathematical equations of the rough contact models used in the tribodynamics simulation. All of these equations were implemented in the LUBST asperity contact solver to obtain the contact forces rising in the clearance revolute joints. Annex A describes these equations in the form that they were implemented in LUBST.

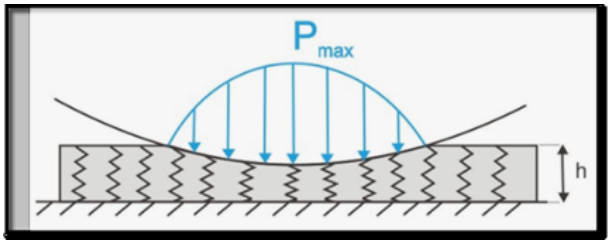

Figure 16 – Elastic model foundation with a rigid base of depth h that is compressed by a rigid indenter and the pressure distribution p over the contact area.

Source: adapted from Johnson (1985).

2.4.1 Hertz Model

Hertz (1882) studied the contact between two elastic solids with smooth surface profiles that could be approximated as a parabola near the contact area 16. This theory predicts that the contact area increases nonlinearly with the normal compressive force F, but $A \approx F^{2/3}$ (PERSSON, 2006), as can be seen in Equation 2.55.

The model developed by Hertz is based on the following simplifying assumptions (STACKOWIAK; BATCHELOR, 2005).

- The materials in contact are homogeneous and the yield stress is not exceeded;
- Contact stress is caused by a load that is normal to the contact tangent plane, which effectively means that there are no tangential forces acting between the solids;
- The contact area is very small compared to the dimensions of the solids in contact;
- Solids in contact are at rest and in equilibrium;
- The effect of surface roughness is negligible.

Hertz (1882) generalized his analysis by assigning a quadratic function to represent the profile of the two opposite surfaces, paying particular attention to the case of spheres in contact (FISCHER-CRIPPS, 2007). He deduced that an ellipsoidal pressure distribution would satisfy the boundary conditions of the problem, and showed that, for the case of a sphere, the required distribution for the normal pressure P(r) was (JOHNSON, 1985):

$$p(r) = p_{max}(1 - \frac{r^2}{a^2})^{1/2} \tag{2.53}$$

Hertz (1882) showed in his modeling that the contact pressure p assumes the form of an elastic potential field with a well-defined boundary. Within this field, stresses are associated with elastic deformations. Beyond the boundary of the field, the elastic deformations in both solids, resulting from contact, are zero (MEDEIROS, 2002).

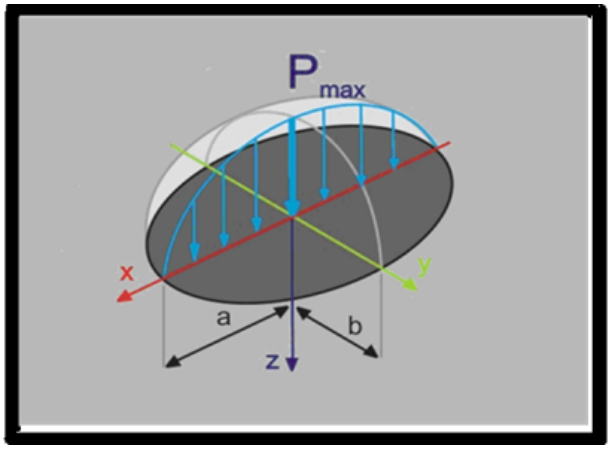

Figure 17 – Contact between two solids pressed against each other by a normal load F showing Hertz parameters in non-conforming contacts.

Source: adapted from Norton 1996.

According to Medeiros (2002), Hertz's effective contribution was to mathematically demonstrate that, in contact with nonconforming static solids compressed together and without friction, geometric and elastic parameters of the material are necessary and sufficient to define the contact area and the states of stress and strain acting.

Figure 17 shows the distribution of the contact pressure in three dimensions and the dimensions a and b of the deformations in their X and Y axes, respectively, characterizing an area with an elliptical geometry at the contact.

When two bodies with a flat, concave, or convex surface come into contact under a given load, these two contact surfaces deform to form a small contact area. Deformation can be plastic or elastic, depending on the amount of applied load, dimensions, and elastic and surface properties of the material. In many engineering applications, the contact areas are very small and the resulting pressures are very high (STACKOWIAK; BATCHELOR, 2005).

The geometric shape of the contact area (or 'footprint') will depend on the geometry of the solids in contact, specifically their radius of curvature and the contact configuration. The main geometries are: elliptical, circular, and rectangular. More generally, elliptical contact is the most common.

From the Hertz analysis, for a contact with a circular geometry, the contact radius a is given by the following expression (JOHNSON, 1985):

$$a = \left(\frac{3FR}{4E}\right)^{1/3} \tag{2.54}$$

The contact area will be $A = \pi a^2$. Substituting a from Equation 2.54, we get:

$$A = \pi\left(\frac{3FR}{4E}\right)^{2/3} \tag{2.55}$$

where F is the normal force applied; R is the equivalent radius, given by the following relationship between the radii of the revolution solids curvatures 1 and 2 (JOHNSON, 1985):

$$\frac{1}{R} = \frac{1}{R_1} + \frac{1}{R_2} \tag{2.56}$$

where E is the equivalent modulus, given by the relationship between the modulus of elasticity E_1 and E_2 and the Poisson coefficients v_1 and $mathitv_2$ of the solids (JOHNSON, 1985).

$$\frac{1}{E} = \frac{1 - {v_1}^2}{R_1} + \frac{1 - {v_2}^2}{R_2} \tag{2.57}$$

From Equation 2.54, the radius of contact is proportional to $F^{2/3}$, so p_{mean} is proportional to $F^{1/3}$. Using the contact area of the Equation 2.55 to calculate the mean pressure p_{mean} and the maximum pressure p_{max}, we have the following expressions:

$$p_{mean} = \frac{F}{\pi a^2} \tag{2.58}$$

$$p_{max} = \frac{3F}{2\pi a^2} = \left(\frac{6FE^2}{\pi^3 R^2}\right)^{1/3} \tag{2.59}$$

The maximum pressure is 3/2 times the mean pressure $p_{max} = (3/2)p_{mean}$.

The normal deformation δ suffered in the contact between the bodies is given by the following relationship:

$$\delta = \frac{a^2}{R} \tag{2.60}$$

Substituting a, from Equation 2.54, we have (JOHNSON, 1985):

$$\delta = (\frac{9F^2}{16RE^2})^{1/3} \tag{2.61}$$

From Equations 2.60 and 2.61, we can isolate the area A and the force F as a function of normal deformation δ.

$$A = \pi\delta R \tag{2.62}$$

$$F = \frac{4}{3}E\delta^{3/2}R^{1/2} \tag{2.63}$$

2.4.2 Greenwood and Williamson Model

Greenwood and Williamson (1966) proposed a statistical model to calculate the load and the real contact area between a rough and a smooth flat plane, as a surface separation function, using the equations proposed by Hertz, which consider the elastic limit. They applied the Hertz concept to the contact involving many asperities assuming constant curvature radius randomly distributed on the surface and used an exponential function to calculate real contact area using an approximated asperity distribution.

Below are some hypotheses applied to the GW model.

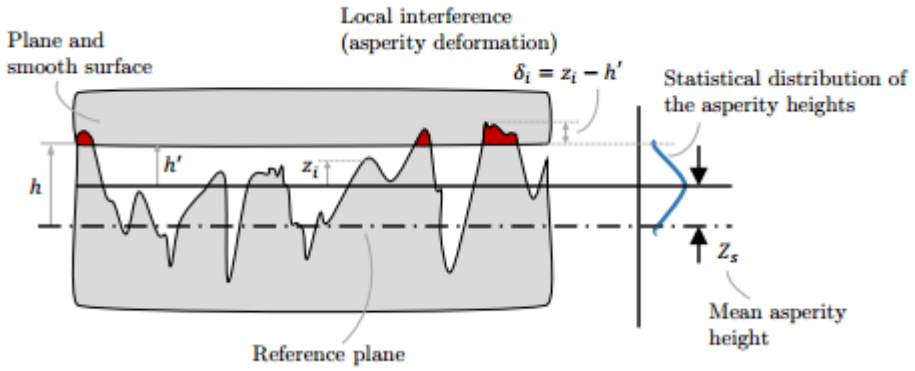

Figure 18 – Contact between a rigid, smooth plane against a rough surface illustrating the main variables of the Greenwood and Williamson (GW) model.

Source: Profito 2015.

- Surface roughness is isotropic;
- Asperities are spherical in the peak points;
- All asperities have the same curvature radius;
- Asperities heights present a approximated Gaussian distribution;
- Each individual asperity deforms separately, so that there is no interaction among them; and,
- The surface deformation below of each individual asperity is neglected.

As an approximation, Greenwood and Williamson proposed the calculation of the asperity height probability density function using an exponential function, as presented in Equation 2.64.

$$p(z) = \frac{1}{\sqrt{2\pi}} e^{-0.5(\frac{h'}{\sigma})^2} \tag{2.64}$$

The calculations of the real area and pressure, in the Greenwood and Williamson statistical model, are a function of the separation distance of the surfaces and are obtained considering the integral, in the distance of contact of the asperities with the flat surface, of the product of the probability height of the density function of the asperity $p(z)$, by interference δ, which is the difference between the height of the asperity and the distance from the approximation to the flat surface $\delta = z - h'$.

The real contact area and the pressure multiplication factors, in the GW model, derive from the equation proposed by Hertz, Equations 2.62 and 2.63, respectively. The equivalent radius of curvature, R, can be considered as the asperity radius β, assuming that contact will occur with a flat surface. In the case of the GW model, it is a function of the integration variable z, the asperity height probability density function of the height of the asperity $p(z)$ and the interference or penetration δ.

Considering the exponential distribution of roughness as an approximation to the Gaussian distribution for numerical calculation purposes, Greenwood and Williamson (1966) provided the following relations to calculate the real pressure and contact area in contact with a rough plane and an ideally smooth flat surface:

$$p_{GW} = \eta\beta\sigma E\frac{4}{3}\sqrt{\frac{\sigma}{R}}\int_{h'}^{\inf}\delta^{3/2}p(z)dz \tag{2.65}$$

$$A_{GW} = \pi\eta\beta\sigma\frac{4}{3}\sqrt{\frac{\sigma}{R}}\int_{h'}^{\inf}\delta p(z)dz \tag{2.66}$$

They also determined the limit of elastic deformation of an asperity, by considering the results of the hardness test by indentation of a sphere, expressed in the work of Tabor (1951). In the indentation hardness test of a sphere, the beginning of plastic flow is reached when the Hertz pressure p_max, between a sphere and a plane, reaches 0.6 H, where H is the hardness of the softer material.

$\delta = \frac{\pi}{2}^2\frac{P^2R}{E}$, from the relation between the Equations 2.62 and 2.55, and taking $P = 0.6H$:

$$\delta = 0.89R(\frac{H}{E})^2 \tag{2.67}$$

Greenwood and Williamson (1966) rounded the equation 2.67 to:

$$\delta^c = R(\frac{H}{E})^2 \tag{2.68}$$

Equation 2.68 represents the critical (maximum) interference for which plastic deformation of the asperity begins. Normalized critical interference $\delta^* = \delta^c/\sigma$ is the maximum normal deformation of the asperity on a given surface, necessary for the beginning of the transition from elastic behavior to plastic.

$$\delta^* = (\frac{H}{E})^2\frac{R}{\sigma} \tag{2.69}$$

2.4.3 Pullen and Williamson Model

Pullen and Williamson (1972) presented a model considering only the plastic deformation of the asperities. Their model was based on three physical observations: (1) the volume of the metal is not changed by plastic deformation; (2) the average indentation pressure is a well-defined material constant applicable to the entire range of asperity shapes; and (3) the displaced material reappears as a bulge in the out-of-contact zone. Similarly to the GW model, the PW model also considered the Gaussian distribution of asperities on the surface of the bodies in contact.

The assumptions applied to the model are the same as those described for the GW model.

$$p_{PW} = \eta\beta\sigma H2\pi\int_{h'}^{\inf}(z-h')^{3/2}p(z)dz \tag{2.70}$$

$$A_{PW} = \eta\beta\sigma 2\pi\int_{h'}^{\inf}(z-h')p(z)dz \tag{2.71}$$

2.4.4 Chang, Etsion and Bogy Model

Chang, Etsion and Bogy (1987) proposed a statistical model that considered the influence of plastic behavior, in addition to elastic behavior, on contact between surfaces. Most highly loaded contacts and between rougher surfaces have a much higher influence of plastic behavior than predicted in the elastic model. This behavior leads to contact areas larger than those predicted in the elastic model.

To model the plastic behavior of roughness, Chang et al. assumed that upon reaching the critical interference, in which the transition from elastic to plastic behavior begins, the roughness conserves its volume in the ensuing deformation, so that when compressed it'spreads' laterally, increasing the contact area. As the load increases, the number of these plastic contacts also increases, but the corresponding contact area in the GW model is calculated from Hertz's theory of elastic deformation, neglecting the conservation of volume in the plastically deformed regions (Mendelson 1968, cited by Chang, Etsion and Bogy (1987)).

The basic model of plastic contact, known as the 'profileometric model', was presented by Abbott and Firestone (1933) considering that the deformation of a rough surface against a plane is equivalent to cutting the undeformed rough surface at its intersection with the plane. The contact area is simply the geometric intersection of the plane with the original profile of the roughened surface, and the pressure on the contact area is the flow pressure or indentation hardness (CHANG; ETSION; BOGY, 1987).

Both assumptions of the plastic contact model, i.e., that the contact area is the geometric intersection of the two surfaces and that conservation of volume during plastic deformation is achieved by a uniform increase of the noncontacting surface, can be valid for heavily loaded contacts when neighboring asperities merge to form large contact areas. However, for light and moderately loaded contacts, in which there is a large percentage of elastically deformed asperities, these assumptions are not as realistic.

Chang et al. (1987), in their work, presented a model that would overcome and correct the discrepancies of results between the two extreme models, completely elastic and completely plastic, applicable to moderately loaded contacts where the deformations of the asperities are primarily elastic and there is also an appreciable percentage of asperities being deformed beyond their elastic limit.

Applying volume conservation, the CEB model adds a second expression to the elastic expression of the GW model, considering that the onset of plastic flow in the asperity occurs when the critical interference δ_c is reached.

$$p_{CEB} = \eta\beta\sigma E\left\{\frac{4}{3}\sqrt{\frac{\sigma}{R}}\int_{h'}^{h'+\delta^*_{CEB}}\delta^{3/2}p(z)\,dz + \pi K\frac{H}{E}\int_{h'+\delta^*_{CEB}}^{\inf}(2\delta-\delta^*_{CEB})p(z)\,dz\right\} \quad (2.72)$$

$$A_{CEB} = \eta\beta\sigma\pi \left\{ \int_{h'}^{h'+\delta^*_{CEB}} \delta p(z)dz + \int_{h'+\delta^*_{CEB}}^{\inf} (2\delta - \delta^*_{CEB})p(z)dz \right\} \tag{2.73}$$

In calculating the critical interference, they considered the contact pressure p, at which the plastic flow starts, equal to KH, where K is a dependent factor function of the Poisson coefficient v.

$$\delta^*_{CEB} = \left(\frac{\pi KH}{2E}\right)^2 \left(\frac{R}{\sigma}\right) \tag{2.74}$$

$$K = 0.454 + 0.41v \tag{2.75}$$

2.4.5 Zhao, Maietta and Chang Model

The CEB model suffers from a discontinuity in contact pressure expression at the critical interface. At this point, the average pressure suddenly jumps from 2/3 KH to KH. Furthermore, the load slope and the actual contact area are different at the critical interface. To overcome this limitation, Zhao, Maietta and Chang (2000) used a mathematical function that bridges elastic and fully plastic segments and maintains the continuity of the load and contact area expressions as well as their slopes (BEHESHTI; KHONSARI, 2012).

According to the analysis of Johnson (1985) for the indentation of a sphere in a plane, the contact load must be increased 400x from the initial yield point to the fully plastic flow state, which suggests that the elastoplastic transition of the flow regime is very long and therefore significant. Finally, the results of the CEB model show that the average separation is greater and the real contact area is smaller for the elastic-plastic contact than for the elastic contact with the same plasticity index and contact load. This result is contradictory to the experimental results of Powierza et al. (1992) and the physical intuition that elastic contact should exhibit greater stiffness than elastoplastic contact.

Within the elastoplastic regime, considering the analysis of Johnson (1985), they arrived at the following interference relation:

$$\delta_2 \geq 54\delta_1$$

This expression suggests that contact interference at the onset of fully plastic deformation would be at least 54 times greater than at initial yielding.

The output of the function must then be scaled by the distance between the top and bottom of the quadrilateral in the $A_{ep} - \delta$ plane, which represents the asperity contact area in the fully plastic and fully elastic states. The scaled function is translated by adding it to the fully elastic function $A_e - \delta$. The transformation results in the following expression:

$$A_{ep} = \pi R\delta[1 - 2(\frac{\delta - \delta_1}{\delta_2 - \delta_1})^3 + 3(\frac{\delta - \delta_1}{\delta_2 - \delta_1})^2] \tag{2.76}$$

The relationship between the average contact pressure and contact interference, within the elastoplastic deformation limit, is given by the following:

$$p_{ep} = [H - H(1-k)\frac{\ln \delta_2 - \ln \delta}{\ln \delta_2 - \ln \delta_1}] \tag{2.77}$$

$k = (2/3)K$, where K is given in Equation 2.75.

Taking $F_{ep} = p_{ep}A_{ep}$, we have the following equation for the load in the elastoplastic regime (ZHAO; MAIETTA; CHANG, 2000):

$$F_{ep} = \pi R\delta[H - H(1-k)\frac{\ln \delta_2 - \ln \delta}{\ln \delta_2 - \ln \delta_1}][1 - 2(\frac{\delta - \delta_1}{\delta_2 - \delta_1})^3 + 3(\frac{\delta - \delta_1}{\delta_2 - \delta_1})^2] \tag{2.78}$$

Applying these relations to the statistical contact, we obtain the following equations (ZHAO; MAIETTA; CHANG, 2000):

$$\begin{aligned} p_{ZMC} = \eta\beta\sigma E\Bigg\{ & \frac{4}{3}\sqrt{\frac{\sigma}{R}}\int_{h'}^{h'+\delta_1}(\delta)^{3/2}p(z)\,dz + 2\pi\frac{H}{E}\int_{h'+\delta_2}^{\inf}\delta p(z)\,dz + \\ & \pi\frac{H}{E}\int_{h'+\delta_1}^{h'+\delta_2}[1-(1-k)\frac{\ln \delta_2 - \ln \delta}{\ln \delta_2 - \ln \delta_1}][1 - 2(\frac{\delta - \delta_1}{\delta_2 - \delta_1})^3 + 3(\frac{\delta - \delta_1}{\delta_2 - \delta_1})^2]\delta p(z)\,dz\Bigg\} \end{aligned} \tag{2.79}$$

$$\begin{aligned} A_{ZMC} = \eta\beta\sigma\pi\Bigg\{ & \int_{h'}^{h'+\delta_1}\delta p(z)\,dz + 2\int_{h'+\delta_2}^{\inf}\delta p(z)\,dz + \\ & \int_{h'+\delta_1}^{h'+\delta_2}[1 - 2(\frac{\delta - \delta_1}{\delta_2 - \delta_1})^3 + 3(\frac{\delta - \delta_1}{\delta_2 - \delta_1})^2]\delta p(z)\,dz\Bigg\} \end{aligned} \tag{2.80}$$

$$\delta_1 = \delta^*_{ZMC} = \left(\frac{3\pi kH}{4E}\right)^2\left(\frac{R}{\sigma}\right) \tag{2.81}$$

The first, second and third terms of the relations correspond to the elastic, plastic, and elastoplastic regimes, respectively.

2.4.6 Kogut and Etsion Model

Although the ZMC model approach solved the continuity problem of the CEB model, this solution was based on mathematical manipulations and not physical considerations. Kogut and Etsion (2003) presented a different approach, where they performed a finite element simulation for the deformation of a single asperity. Next, they proposed convenient empirical expressions that include different asperity deformation regimes. Given the relationship of contact with a single asperity, they extended the approach to contact with rough surfaces using the statistical method (BEHESHTI; KHONSARI, 2012).

Kogut and Etsion (2003) used the finite element method to solve the elastoplastic contact problem of a single asperity and observed that the complete elastoplastic regime

is within interference values in the range of $1 \leq \delta/\delta_c < 110$ with a distinct transition in mean contact pressure at $\delta/\delta_c = 6$. Up to transitional interference $\delta/\delta_c = 6$, a plastic region develops below the contact interface, while the entire contact area is elastic. Above $\delta/\delta_c = 6$, the contact area contains an elastic circular inner core that is surrounded by an outer plastic ring. This elastic core contracts with increasing interference and finally disappears completely at $\delta/\delta_c = 68$. From this point on, the entire contact area is plastic, but the average contact pressure continues to increase until it becomes constant and equals the hardness at $\delta/\delta_c = 110$.

The dependence of A and F on δ in the elastoplastic regime has been expressed in the following general forms:

$$\frac{A}{A_c} = b(\delta/\delta_c)^m \tag{2.82}$$

$$A_c = \pi R \delta_c$$

$$\frac{F}{F_c} = c(\delta/\delta_c)^n \tag{2.83}$$

$$F_c = \frac{2}{3} KH\pi R\delta_c$$

The values of the constants b, m, c and n are determined by the contact mode in the four different deformation regimes and are presented in Table 4.

Table 4 – Values of constants b, m, c e n to the several deformation regimes.

Deformation regime	b	m	c	n
Fully Elastic	1	1	1	1.5
1st Elastoplastic regime $1 \leq \delta/\delta_c \leq 6$	0.93	1.136	1.03	1.425
2nd Elastoplastic regime $6 \leq \delta/\delta_c \leq 110$	0.94	1.146	1.4	1.263
Fully Plastic $\delta/\delta_c > 110$	2	1	3/K	1

Source: from Kogut and Etsion (2003).

Based on these considerations for contact involving an asperity, Kogut and Etsion (2003) proposed the following load relationships and actual contact area using the statistical model:

$$p_{KE} = \eta\beta\sigma E \left\{ \frac{4}{3}\sqrt{\frac{\sigma}{R}} \int_{h'}^{h'+\delta_c} (\delta)^{3/2} p(z)\,dz + \frac{2}{3} 1.03\pi K {\delta_c}^{-0.425} \frac{H}{E} \int_{h'+\delta_c}^{h'+6\delta_c} \delta^{1.425} p(z)\,dz + \right.$$
$$\left. \frac{2}{3} 1.4\pi K {\delta_c}^{-0.263} \frac{H}{E} \int_{h'+6\delta_c}^{h'+110\delta_c} \delta^{1.263} p(z)\,dz + 2\pi \frac{H}{E} \int_{h'+110\delta_c}^{\inf} \delta p(z)\,dz \right\} \tag{2.84}$$

$$A_{KE} = \eta\beta\sigma\pi \left\{ \int_{h'}^{h'+\delta_c} \delta p(z)\,dz + 0.93\pi\eta\sigma {\delta_c}^{-0.136} \int_{h'+\delta_c}^{h'+6\delta_c} \delta^{1.136} p(z)\,dz + \right.$$
$$\left. 0.94 {\delta_c}^{-0.146} \int_{h'+6\delta_c}^{h'+110\delta_c} \delta^{1.146} p(z)\,dz + 2 \int_{h'+110\delta_c}^{\inf} \delta p(z)\,dz \right\} \tag{2.85}$$

$$\delta_c = \delta^*_{KE} = \delta^*_{CEB} = \left(\frac{\pi KH}{2E}\right)^2 \left(\frac{R}{\sigma}\right) \tag{2.86}$$

The first and last terms of the relations correspond to the elastic and plastic regimes, respectively, and the second and third terms correspond to the first and second elastoplastic regimes.

2.4.7 Jackson and Green Model

Jackson and Green (2006) proposed a new model based on finite element analysis. They used, in their modeling, finer meshes than the KE model and took into account the effects of material properties and geometry during deformation. Furthermore, they extended the KE contact model to a roughness deformation of up to the value $a/R = 0.41$. They showed that the elastic deformation hypothesis for the asperity contact is valid not only within the critical interface limit, but up to 1.9x the critical interface. However, they did not determine the interface at which the full plastic regime starts. Unlike the KE model, which assumes constant hardness, the JG model considers the hardness variation during deformation. They showed that, in contrast to the KE model, the value of 2.8 for the relationship between mean pressure and flow resistance is not reached, even for very high interfaces.

Jackson and Green (2006) analytically derived critical interference using the Von Mises criterion, which resulted in the following equation:

$$\delta_{cJG} = \left(\frac{\pi C S_y}{2E}\right)^2 (\frac{R}{\sigma}) \tag{2.87}$$
$$C = 1.295 e^{0.736v}$$

The definition of critical interference for the JG model does not use the hardness H, but the yield strength S_y. They argued that the hardness is not constant for a given geometry; that is, by changing the roughness geometry, in contact, its hardness is changed.

The critical force F_c is then calculated from the critical interference δ_c, using equation 2.63:

$$F_c = \frac{4}{3}(\frac{R}{E})^2(\frac{C}{2}\pi S_y)^3 \tag{2.88}$$

Similarly, the critical contact area is calculated from equation 2.62:

$$A_c = \pi^3(\frac{C S_y R}{2E})^2 \tag{2.89}$$

At $0 \leq \delta/(\delta_c)_{JG} \leq 1.9$, the current simple roughness model effectively coincides with the Hertz solution. In larger interference, the following equations describe the contact of a single asperity in elastoplastic behavior.

$$A_{ep} = \pi R \delta (\frac{\delta}{1.9\delta_c})^B \tag{2.90}$$

$$B = 0.14e^{23(\frac{S_y}{E})}$$

$$F_{ep} = F([e^{-0.25(\frac{\delta}{\delta_c})^{5/12}}](\frac{\delta}{\delta_c})^{3/2} + \frac{4H_G}{CS_y}[1 - e^{(}-0.04(\frac{\delta}{\delta_c})^{5/9})]\frac{\delta}{\delta_c}) \tag{2.91}$$

$$\frac{H_G}{S_y} = 2.84[1 - e^{(-0.82(\sqrt{\frac{\delta}{R}}(\frac{\delta}{1.9\delta_c})^{B/2})^{-0.7})}]$$

Based on these considerations, Jackson and Green (2006) proposed the following load and real contact area relationships using the statistical model:

$$p_{JG} = \eta\beta\sigma E\left\{\frac{4}{3}\sqrt{\frac{\sigma}{R}}\int_d^{d+1.9\delta_c}\delta^{3/2}p(z)\,dz + \frac{4}{3}\frac{C\pi S_y}{2E}\int_{d+1.9\delta_c}^{\inf}(\delta_c)^{-0.5}(\delta)^{3/2}e^{-0.25(\frac{\delta}{\delta_c})^{5/12}+4\frac{2.84}{C}(1-e^{(-0.82(\sqrt{\frac{\delta}{R}}(\frac{\delta}{1.9\delta_c})^{B/2})^{-0.7})})\delta(1-e^{(-0.04(\frac{\delta}{\delta_c})^{5/9}))}}p(z)\,dz\right\} \tag{2.92}$$

$$A_{JG} = \eta\beta\sigma E\left\{\int_d^{d+1.9\delta_c}\delta^{3/2}p(z)\,dz + (\frac{1}{1.9\delta_c})^B\int_{d+\delta_c}^{\inf}(\delta)^{D+1}p(z)\,dz\right\} \tag{2.93}$$

2.4.8 Brief Contact Models Comparison

Table 5 presents some summarized characteristics and general comments on the contact models described in sections 2.4.2 to 2.4.7.

Table 5 – Comparison between the models regarding the regimes, number of terms and transitions.

Model	Year	Regime	Number of Terms	Transitions
GW	1966	Fully Elastic	1	0
CEB	1987	Elastic - Fully Plastic	2	0
ZMC	2000	Elastoplastic	3	1
KE	2003	Elastoplastic	4	2
JG	2006	Elastoplastic	2	1
PW	1972	Fully Plastic	1	0

Figure 19 presents graphical schemes that intends to qualitatively indicate the differences between elastic and elastoplastic contact models according to their mathematical formulation, particularly their terms of integration. It is represented as the elastoplastic behavior as a function of the intensity of interference (δ) - magnitude of the contact between the surfaces.

Some main differences and limitations of the models studied:

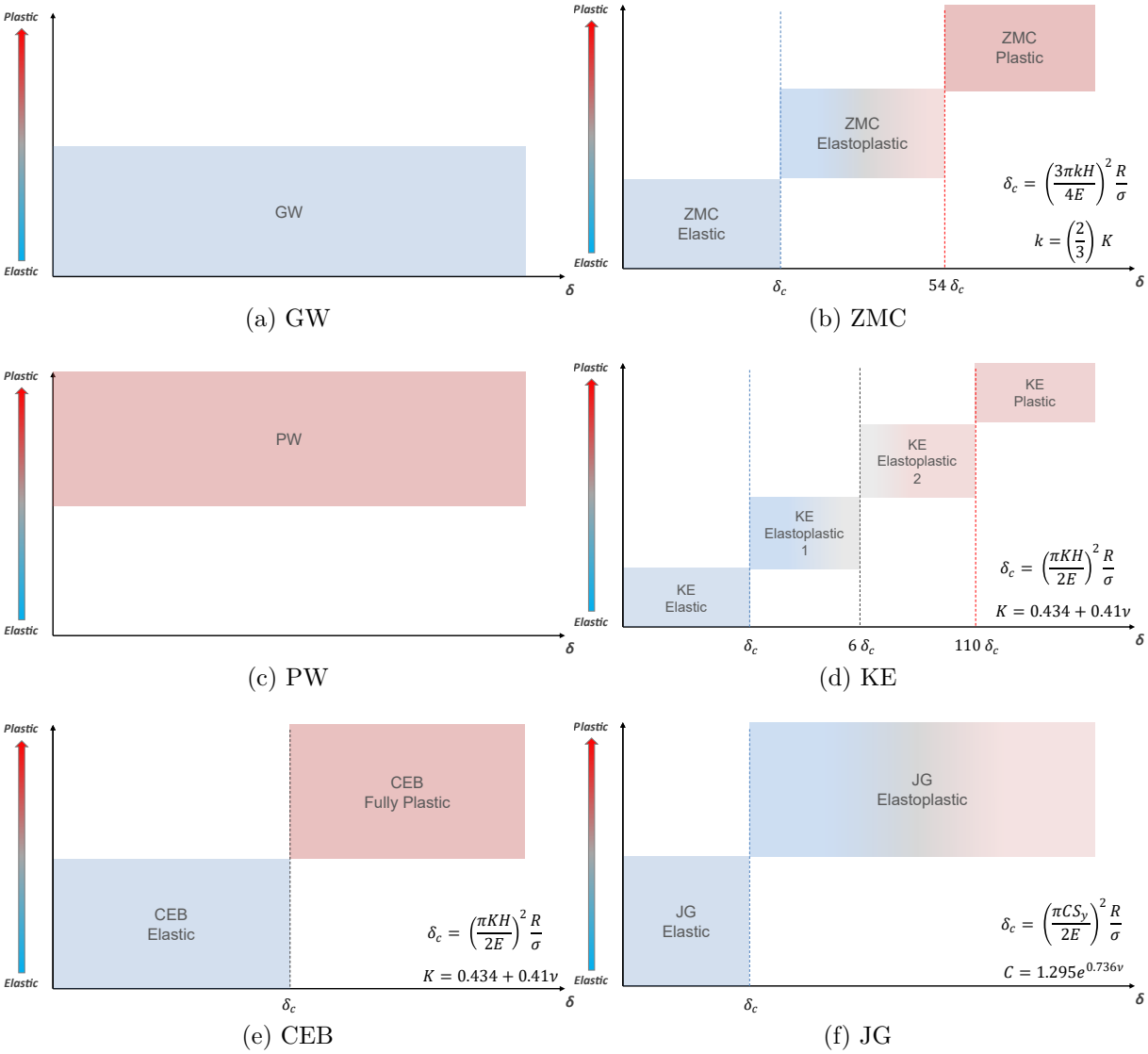

Figure 19 – Graphic schemes of the contact models according to their integration terms and respective critical interference mathematical formulation.

Greenwood and Williamson Model (1966)

- Calculus with low plasticity indexes, < 1, predominantly elastic contact;

- As it considers the calculation of the load and the real area of contact based on the Hertz equations, is limited only to use within the elastic regime of the material, that is, it is used with greater precision in small deformations or when the surfaces in contact are extremely smooth, with very low roughness; at high loads, which lead to high levels of plastic deformation of the asperities, the model starts to underestimate the real contact area.

- Regarding the GW model, it should be noted that the presented parameters consider only the surface characteristics for both load and contact area calculations.

Chang, Etsion and Bogy Model (1987)

- Their model considers the amount of plastic deformation suffered by the asperities and its influence on the load and the real contact area by applying the conservation of volume in the plastic deformation. In the calculation of critical interference, it uses a constant K, which is a function of the Poisson coefficient;

- It does not consider the long transition stage from the elastic to plastic behavior of roughness (it presents a discontinuity in the transition). Consider, in the calculation that, above the critical interference, the roughness is only plastically deformed, and does not yet show any elastic deformation.

Zhao, Maietta and Chang Model (2000)

- ZMC model considers a step of continuous transition between the elastic and the plastic regime mathematically, overcoming the discontinuity of the CEB model. Defines a second critical interference as the limit from the elastic to the completely plastic regime, where, $\delta_2 \geq 54\delta_c$, based on Johnson's considerations (JOHNSON, 1985);

- Although the ZMC model solved the discontinuity of the CEB model by adding an elastic-plastic transition regime, this was based on mathematical manipulations and not on physical considerations (BEHESHTI; KHONSARI, 2012).

Kogut and Etsion Model (2003)

- They presented a different approach running finite element simulations for the deformation of a single asperity. They proposed two transition moments with empirical expressions that include different deformation regimes. Critical interference limits differentiated from other models at each transition moment;

- They did not consider the effects of material properties and geometry during deformation.

Jackson and Green Model (2006)

- Compared with the KE model, they used finite elements with finer meshes, obtaining more accurate answers. They took into account, in the analyses, the effects of material properties and geometry during deformation. They also extended the KE model to a high roughness strain, up to the value of $a = 0.41R$. They showed that the elastic deformation hypothesis for the asperity contact is valid not only within the

critical interface limit, but also up to $1.9\delta_c$. They use as a material property, in the calculation of the critical interface, the flow resistance of the material S_y;

- They did not determine the interface at which the completely plastic regime starts, which was shown in the other models.

Pullen and Williamson Model (1972)

- PW model presents only one term that represents the fully plastic deformation behavior of the asperity. They used the hardness of the soft material to calculate the asperity pressure.

2.5 Friction Modeling

The well-known Coulomb model was used to obtain the friction (tangential) force in the contact between the surface asperities.

3 Computational Procedure

The computational procedure employed sought to generate and present as results some important parameters of the clearance joint behavior, such as Minimum Oil Film Thickness (MOFT), hydrodynamic and contact peak pressures and power losses, and the dynamic response of the system bodies.

Simulation has been divided into two major flow groups: (i) initial procedure and (ii) dynamic integration procedure. The initial procedure is subdivided into six blocks: model data, initial kinematic data, bearing parameters, loads, initial acceleration, and ideal joint reaction forces (if there be any), and initial time data. The second and last major group, the dynamic integration procedure, follows a similar processing sequence as the first one, but with the difference that some blocks update and store the data in each step of integration procedure. In the latter case, these blocks are inside a loop that only ends when the maximum time or crankshaft angle determined is reached, as presented in Figure 21.

Both these two groups have variables that are concentrated in a unique structured variable called 'MDS'. This variable MDS contains other seven structured variables: mechanism, simulation, kinematic, bearings, loads, and time. From these structures, only the mechanism and simulation variables can be considered as data fixed, that is, no one variable inside it is changed or added during the integration procedure (loop). The other four structures variables have data that are changed in the dynamic integration procedure.

3.1 Initial Procedure

Figure 20 presents a flow diagram of simulation processing for the first major group, the initial procedure.

This procedure has used the Lubrication Simulation Toolbox (LUBST) (PROFITO, 2015) to calculate the contact and hydrodynamic pressures to obtain the resulting forces and moments actuating in the clearance joints. The models used in the simulations are explained in forward sections.

During this work development, it was elaborated and implemented a few functions that resulted in the creation of a small Multibody Dynamic Simulation Toolbox (MDST) which has been coupled to the LUBST (PROFITO, 2015). As a contribution of this work a User Interface (UI) has been thought and it is in development to enable interaction with a user who wants to simulate similar models. The elastoplastic rough contact models were implemented inside the structure of LUBST that already had implemented in it as a

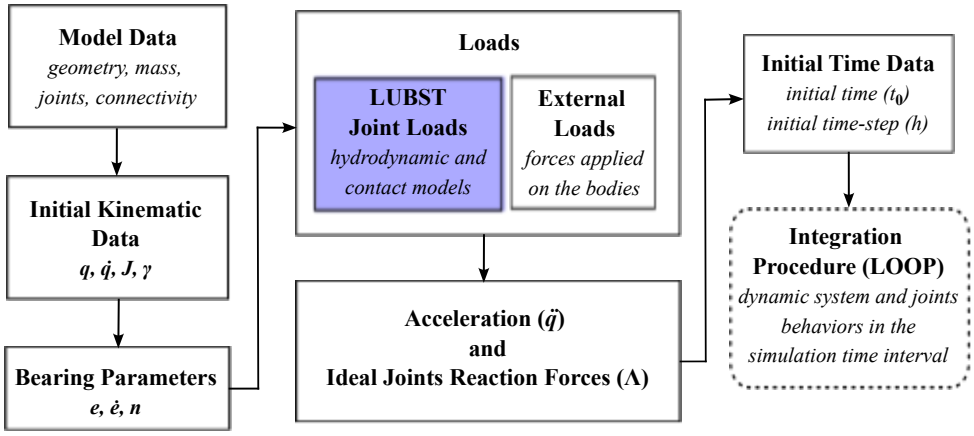

Figure 20 – System initial procedure flow diagram.

standard model the elastic Greenwood and Tripp (GT) contact model.

3.1.1 Model Data

Some important and necessary data are taken from the mechanism model to define and obtain the initial kinematic data. The data of the main structure of the mechanism are divided into other major minor structures: identification, analysis, number of bodies and joints, connectivity, restrictions, geometry, mass and inertia moment bodies properties, and bearing parameters.

Identification is the name designated for the dynamic system simulation. Analysis indicates if the system will be set to run as a planar system (2D) or a spatial system (3D); at the present time, only the planar (2D) analysis is supported. Connectivity is a matrix representing the connection relationship between bodies and joints. The geometry, mass, and inertia data structures contain the dimensional and inertial properties of the bodies; dimensions are taken from the center of mass local coordinate reference to the point of bearing connection. Bearing parameter structure data present information about the simulation of each clearance joint in the system: modeling type (it allows to choice between hydrodynamic and contact analytical models or LUBST models), number of bearings per joint connection, lubricant rheology consideration, if a connection body is bearing or journal, and initial eccentricity.

All these parameters stored in the form of data structures are used to develop the system initial conditions and the dynamic integration procedure.

3.1.2 Initial Kinematic Data

Initial kinematic block uses the data contained in the mechanism data structure to obtain the initial position and velocity of the dynamic system bodies, calculate the jacobian matrix **J** and gamma γ, that is the acceleration right hand term equation. These

last two parameters mentioned, **J** and gamma γ, exist if there are one or more ideal joints connecting the bodies because they are directly related to each equation of the restriction joint. Initial body velocity and acceleration were calculated via a recursive method that uses the data from the predecessor body and the joint.

3.2 Dynamic Integration Procedure

Having defined the initial kinematic conditions of the system, including the position of the body and joints of the system, velocity and acceleration, the initial loads and the reaction forces of the ideal joints, as shown in Figure 20, we can start the dynamic integration procedure. In this procedure, some important parameters that will be used as graphic results are stored in a form of numeric data arrays. Such parameters are angular and linear system bodies position, velocities, accelerations and clearance joints orbit dislocation, hydrodynamic and contact peak pressures and power losses, minimum film oil thicknesses, joints loads, and cumulative time.

Figure 21 presents a flow diagram of simulation processing for the second main group, dynamic integration procedure.

3.2.1 Integrator

For the purpose of integrating the acceleration and velocity data vectors of the system bodies and obtain, respectively, the velocity and position to the next time step, an E2-type implicit scheme, belonging to the family of second-order Stable L-SDIRK methods, was used as the integrator. This scheme is detailed in the article of Skvortsov (2013). The second-order differential equations are converted to the first-order equations by defining the $\mathbf{y}$ and $\dot{\mathbf{y}}$ vectors that contain, respectively, the system positions and velocities and the system velocities and accelerations.

$$\mathbf{y} = \begin{bmatrix} \mathbf{q} \\ \dot{\mathbf{q}} \end{bmatrix} \tag{3.1}$$

$$\dot{\mathbf{y}} = \begin{bmatrix} \dot{\mathbf{q}} \\ \ddot{\mathbf{q}} \end{bmatrix} \tag{3.2}$$

The kinematic data vectors (position and velocity), obtained as a result of the integration process, are related to the movement of the center of mass (CG) of the body. As presented in the following relation, velocities and accelerations at instant t after the integration process, yield position and velocities at the next time step, $t = t + \delta t$.

$$\dot{\mathbf{y}}(t)(integration) \rightarrow \mathbf{y}(t + \delta t) \tag{3.3}$$

The integrator is implemented considering three different system types: ideal, clearance and mixed. In the case of mixed system type, when there are ideal and clearance

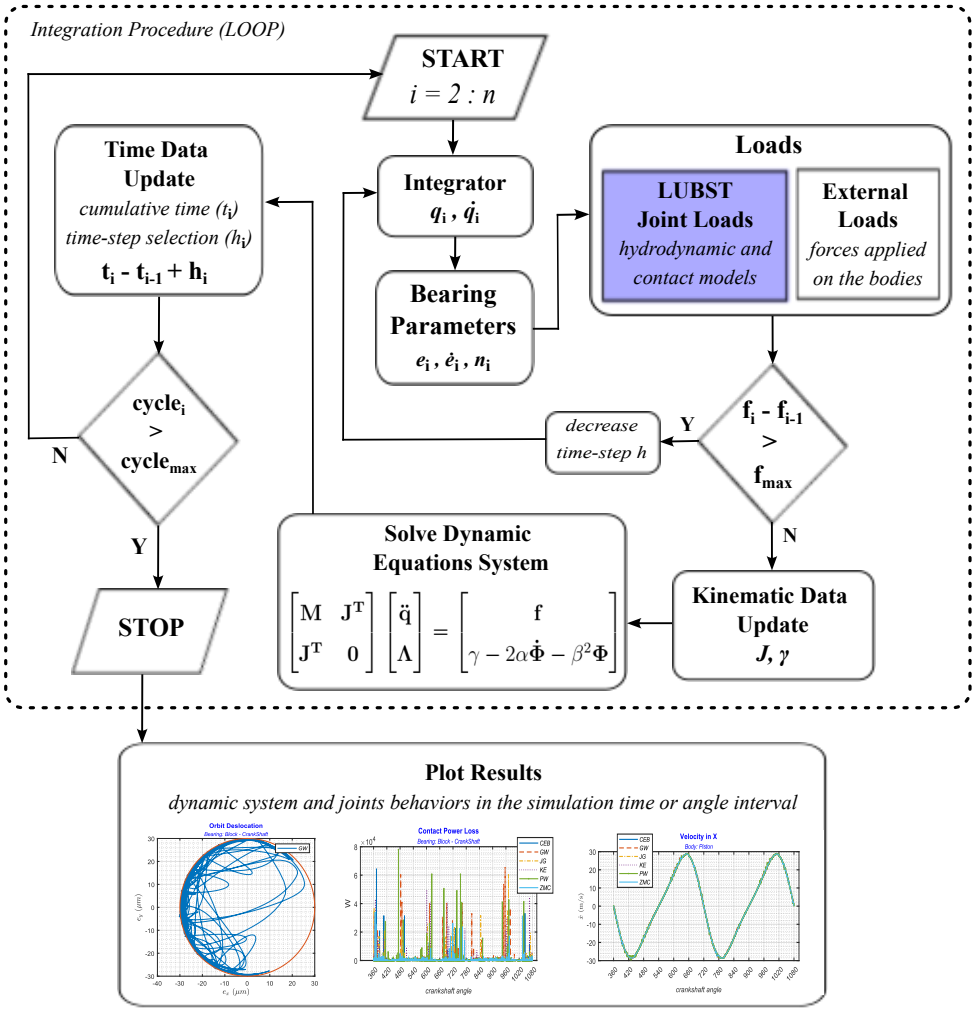

Figure 21 – Dynamic integration procedure flow diagram.

joints connecting bodies, the integration procedure is first performed for the subgroup of perfectly connected bodies or constrained group, whose bonds are considered ideal, and then for the subgroup of unconstrained bodies.

The direct integration method of equations of motion leads to the constraint violations due to the truncation and round-off errors that are computed during the integration procedure. Therefore, in a closed system type, it is necessary to consider the use of a stabilization technique to avoid these constraint violations, as described in section 2.1.4 of this work. As recommended, the parameters definitions α and β were established by running the simulation considering the mechanism with all joints as ideal and checking the position and velocity behavior.

3.2.2 Bearing Parameters

The bearing parameters block returns the eccentricity vector ($\mathbf{e}$), its first time derivative ($\dot{\mathbf{e}}$) and the normal vector $\mathbf{n}$. The position and velocity in the center of mass of the bodies data, obtained from the integration procedure or initial kinematic condition,

are used as input data to calculate them. The two first bearing parameters, $\mathbf{e}$ and $\dot{\mathbf{e}}$, are necessary as input data to calculate the hydrodynamic and contact loads of the clearance joints. These calculations are made inside the Loads block through the use of LUBST or analytical models.

It is structured to attempt two types of clearance joints: revolute and translational joints. Inside these substructures are stored the necessary data to calculate the loads that act there.

3.2.3 Loads

In the load's block, the loads actuating in the bodies of the system are obtained and calculated. Two types of loads can be considered: dynamic and clearance joints loads, including forces and moments. The first one, dynamic loads, are uploaded from a file containing the data and stored using a piecewise polynomial function whose data will be evaluated during the progress of the simulation, in the dynamic integration procedure, as commonly a function of the crankshaft angle. In particular, in the case simulated, no dynamic forces were considered.

The loads in the clearance revolute joints were calculated using the hydrodynamic and asperity contact models available and implemented in the LUBST toolbox. The models to be used in the simulation to each joint is defined by the user before it begins. LUBST incorporates the hydrodynamic model based on the Reynolds equation with the Jakobsson-Floberg-Olsson (JFO) cavitation model and the asperity contact models discretizing the bearing domain in a structured grid of 800 total nodes and solving it through the Finite Volume Method by Element (FVMbE) (PROFITO, 2015). This work considered the LUBST to calculate the hydrodynamic and contact loads for all clearance joints.

3.2.4 Time Data

To obtain an improved simulation, the integration procedure uses an integrator with a variable time step size. It was implemented as a function of the clearance joint eccentricity. The closer the contact, the smaller the time step size. Thinking about this, a maximum and a minimum time-step size is defined in the simulation. A good definition of these values will depend on some factors such as radial clearance, models used (high nonlinearity), drive body velocity, and lubricant viscosity, among others, so it is important to know well about the system characteristics and configuration to obtain good results in a short time. Otherwise, in the worst case, there will be no convergence in the simulation.

Time Step Selection

In this study, the time-step size was modeled using a mathematical function dependent on the eccentricity parameter. The function is chosen by the user, and it is defined before the simulation starts. Some of the functions available to model the behavior of these parameters are the *erf*, exponential or *log* functions. Once the system with clearance joints is initially modeled with high constant velocity, the simulation makes possible to set different initial time step values in different simulation intervals being dependent or not of the crankshaft angle.

Recalculation by Load Limit

The procedure allows to limit the maximum load difference between the integration steps. In each step, the load difference is verified and if it is higher than the maximum load value established, a smaller time step than the previous one is defined and the integration procedure is started again in order to limit the initial high loads that may occur in the beginning of simulation, facilitating the initial convergence. This procedure happens inside the integration procedure loop and the number of recalculate iterations is limited according to the value defined by the user. On the other hand, depending on the value of maximum load defined to a specific mechanism, it can result in a large amount of recalculation to reach a load lower than the value established. This condition will lead to a small time step size, and it will result in a large time to finish the simulation.

3.2.5 Solving Dynamic Equations System

In the integration procedure (loop), the dynamic equation system is solved using the Newton-Raphson numeric iterative method. Initial guess data x_{i-1}, that is, the vector with acceleration and reaction forces, is used with the data obtained in the last time step. In solving the equations system, two parameters are initially defined: tolerance and maximum number of steps to convergence. The process is repeated within a *loop for* using the updated vector data x_i to evaluate $H(x_i)$ until the established tolerance is satisfied through the relationship 3.4:

$$x_i = x_{i-1} - \frac{\mathbf{H}(x_{i-1})}{\mathbf{\Xi}(x_{i-1})} \tag{3.4}$$

where x_i and x_{i-1} are the column of vectors containing the acceleration and reaction forces, respectively, to the last and actual step; $\mathbf{H}(x_{i-1})$ and $\mathbf{\Xi}(x_{i-1})$ are, respectively, the evaluation of the term of the equation on the right hand side containing the total forces and the parameters of the Baumgarte stabilization method, and the matrix of the term of the equation on the left hand side (formed by the mass and *Jacobian* matrix) evaluated with the data of the last step. It is repeated until one of the two relations is satisfied: (i) if it reaches the maximum number of iterations without attempt of the established tolerance,

or (ii) when the difference $x_i - x_{i-1} \leq tolerance$.

$$\mathbf{x} = \begin{bmatrix} \ddot{\mathbf{q}} \\ \mathbf{\Lambda} \end{bmatrix} \tag{3.5a}$$

$$\mathbf{\Xi} = \begin{bmatrix} \mathbf{M} & \mathbf{J^T} \\ \mathbf{J^T} & \mathbf{0} \end{bmatrix} \tag{3.5b}$$

$$\mathbf{H}(x) = \begin{bmatrix} \mathbf{M\ddot{q}} + \mathbf{J^T\Lambda} - \mathbf{f} \\ \mathbf{M\ddot{q}} - (\gamma - 2\alpha\mathbf{\dot{\Phi}} - \beta^2\mathbf{\Phi}) \end{bmatrix} \tag{3.5c}$$

4 Results

In this study, three different configurations of the clearance revolute joints of a crank–connecting rod–slider mechanism have been simulated by applying the hydrodynamic and contact models described in Sections 2.3 and 2.4. Figure 22 shows the mechanism configurations I, II and III indicating the clearance revolute joints considered in the simulations.

The mechanism data are based on the model presented by Flores, Ambrósio and Claro (2004), with the lubricant viscosity decreased for the system to reach the limit of the mixed lubrication regime. Table 6 presents the description and identification of the three mechanism configurations considered in the simulations.

Table 6 – Clearance revolute joints considered in the three mechanism configurations.

Configuration	Description	Identification
I	Connecting rod–slider with clearance joint	1RJ
II	Connecting rod–slider and crankshaft–connecting rod with clearance joints	2RJ
III	Connecting rod–slider, crankshaft–connecting rod, and block-crankshaft with clearance joints	3RJ

In the first configuration, only the connecting rod–slider joint (CR–S) was considered a clearance joint. In the second configuration, the connecting rod–slider (CR–S) and the crankshaft–connecting rod (CS–CR) joints were assumed clearance joints. Finally, in the third configuration, all revolute joints, including the block–crankshaft joint (B–CS), were admitted clearance joints. Table 7 presents the body coordinates of the connection points of the revolute joints and the mass and inertia moments of the mechanism bodies.

It is assumed that no forces act on the tangential contact between the slider and the block on the translational joint, and the gravitational force was not considered in the simulations. The angular velocity of the crankshaft was kept constant at 5000 RPM. The parameters of the Baumgarte stabilization method (α and β) were equal to 500.

Table 7 – Bodies properties.

Body	Mass (kg)	Inertia Moment (kgm^2)	Coordinates (m)
Crankshaft	0.30	0.00010	$\mathbf{s}_2^1 = [0; 0]$ $\mathbf{s}_2^2 = [0.05; 0]$
Connecting Rod	0.21	0.00025	$\mathbf{s}_3^2 = [-0.06; 0]$ $\mathbf{s}_3^3 = [0.06; 0]$
Slider	0.14	0.00010	$\mathbf{s}_4^3 = [0; 0]$ $\mathbf{s}_4^4 = [0; 0]$

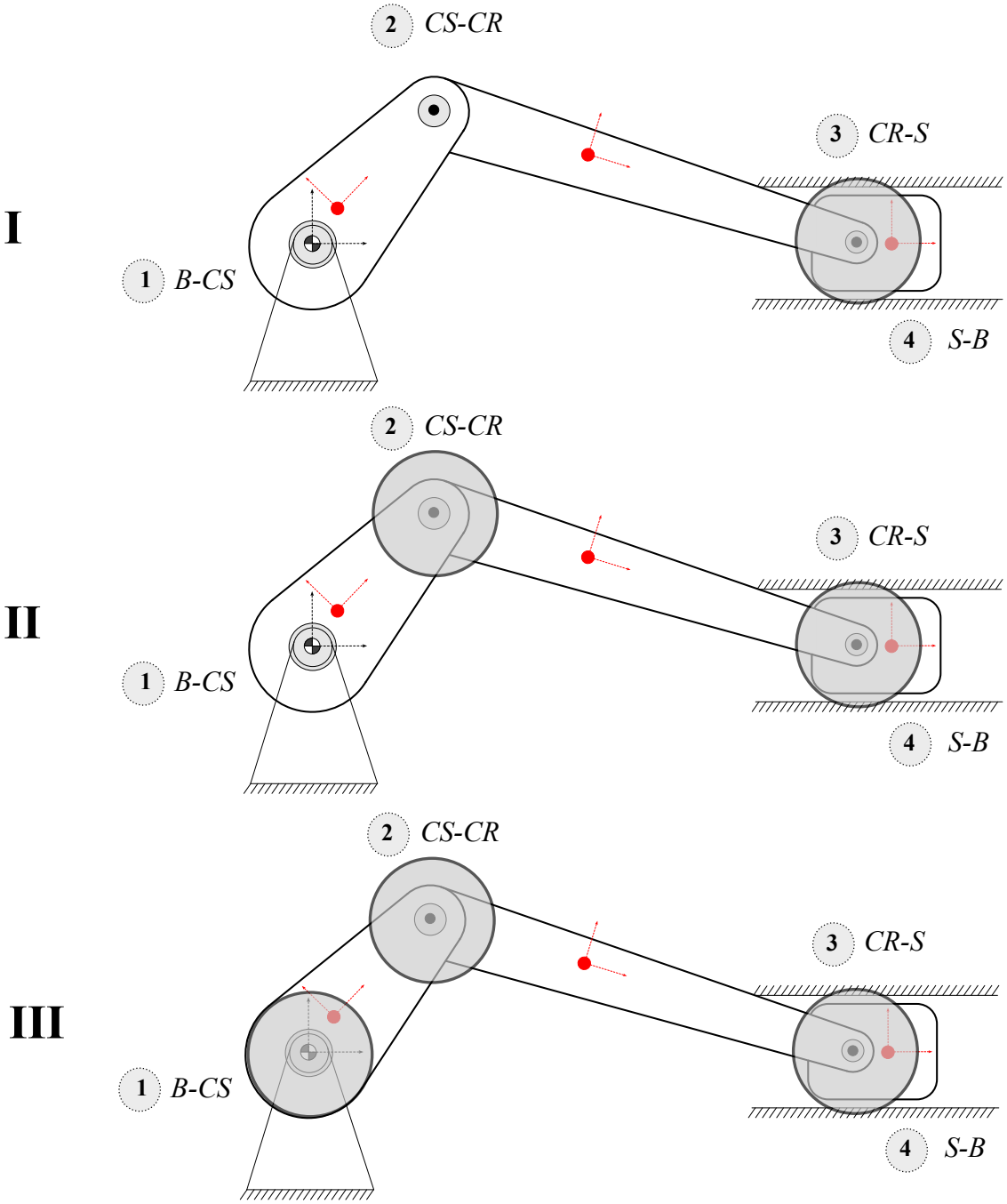

Figure 22 – Mechanism configurations I, II and III.

Table 8 – Joint parameters, material, geometry and bearing roughness properties.

Parameter	Value
Bearing radius, R_b	10 mm
Bearing width, L_b	20 mm
Radial clearance, c	30 µm
Lubricant viscosity, μ	1.0×10^{-4} Pa s
Asperity mean height, h	0.198 µm
Asperity height standard deviation, σ	0.251 µm
Asperity mean radius, β	15.980 µm
Density of asperities, η	10.760×10^{9} m^{-2}
Boundary coefficient of friction, c_f	0.08
Equivalent elastic modulus, E	115.18 GPa
Hardness, H	1373 MPa
Yield Strength, S_y	500 MPa
Poisson coefficient, v	0.3

The tolerance of 1.0×10^{-9} was applied to solve the motion equation system using the numerical iterative method of Newton-Raphson. For joint configurations I and II, the maximum and minimum time steps used were 20×10^{-6} and 7.25×10^{-7}, respectively, and for joint configuration III, 15×10^{-6} and 6.50×10^{-7}. These values allowed for a uniform and smooth simulation of the cases analyzed.

Regarding the joints and lubricant, a constant low viscosity lubricant and three revolute joints with identical radius (R_b), width (L_b) and clearance (c) were considered. These values were assumed constant in all simulation cases, changing only the joint configurations and the contact models. Table 8 summarizes the joint parameters, geometry, material, and bearing roughness properties.

A computer with the following characteristics was used to perform the simulations. Windows Operating System 10 x64, processor Intel® Core™ i5-7200U CPU @ 2.50 - 2.71 GHz, 16 GB of memory RAM, and MATLAB® software, version R2022a. The simulation time is mainly dependent on the number of clearance joints. The time consumed to execute dynamical simulations for configurations I, II, and III was approximately 5, 10 and 20 hours, respectively. Considering that for each configuration, six simulations were needed, one for each contact model, it took a time of approximately 30, 60 and 120 hours, respectively, to finish simulations for configurations I, II, and III, totalling about 210 hours of computational simulation.

The following sections present the results of the application cases described in the table 6. It includes the results of the dynamic behavior of the moving bodies of the crank–connecting rod–slider mechanism studied and the performance of its clearance joints for the three mechanism configurations considered. In order to check the dispersion of the MOFT results obtained by the models simulated in the clearance joints, standard deviation (STD) was calculated and it has been presented in the MOFT data table results.

Such parameter was calculated using the following formulation:

$$STD = \sqrt{\frac{\sum_{i=1}^{N}(MOFT_i - MOFT_{mean})^2}{N}}$$

where $MOFT_i$ is the MOFT value in the step i, N is the amount of MOFT values in the sample and $mean_{MOFT}$ is the arithmetic average of all the MOFT values in the sample.

4.1 Mechanism Configuration I

4.1.1 Lubrication Performance

Figure 23 presents the journal orbits in the connecting rod–slider joint (CR–S) calculated with the different contact models evaluated. The journal orbits for each contact model are similar in this joint configuration. However, it is possible to observe higher local fluctuations in the eccentricity predicted with the elastoplastic models in the crank angle intervals $0 - 60°$ and $330 - 360°$ (orbit left side).

Figure 24 shows the results of the bearing performance parameters calculated with the different contact models used in the simulations, and Figure 25 and Table 9 summarizes the mean, minimum, and maximum values of the minimum oil film thickness (MOFT) in the crank angle intervals $660° - 780°$ and $840° - 960°$. From the results portrayed in Figure 24, it is possible to notice a wide variation in the performance parameters in the transition intervals of the displayed cycles ($360° - 420°$, $660° - 780°$, $1020° - 1080°$). Looking at Figure 24 (c) and (d), we can note high hydrodynamic peak pressures in the crank angle intervals $360° - 420°$, $660° - 780°$ and $1020° - 1080°$, reaching values higher than 1 GPa at some points. On the other hand, in these intervals, the asperity peak pressures just reached 0.1 GPa at some points with the GW model. Moreover, the influence of asperity contact on power losses increased in the crank angle intervals $450 - 630°$ and $810 - 990°$ when the asperity contact pressures began to exceed the hydrodynamic pressures. In the crank angle intervals $360 - 420°$, $660 - 780°$ and $1020 - 1080°$, even with the high asperity peak pressures generated by the increased local contact compared to the other crank angle intervals, it was not representative compared to the hydrodynamic peak pressures.

The asperity contact power losses are the main ones responsible for the total power losses, as shown in Figure 24 (e). In this joint configuration, higher power loss values were obtained in the crank angle intervals $360° - 420°$, $660° - 780°$ and $1020° - 1080°$, reaching the maximum values just above 800 W for the GW model. In this case, the GW and CEB models presented the maximum and minimum values of power losses among all contact models in these crank angle intervals. The power losses were very close among the models in the crank angle intervals $450° - 630°$ and $810° - 990°$.

Interesting results are related to the analysis of Figure 24 (f) and Table 9. It is possible to note that the GW model presented the highest MOFT values and the CEB model the lowest values in the cycles analyzed. CEB model achieved the lowest MOFT of 0.3 µm in the crank angle intervals $360 - 420°$, $660 - 780°$ and $1020 - 1080°$. Considering the MOFT in the crank angles of 600° and 960°, there is a 0.1 µm difference between the GW and CEB models. Taking the asperity standard height deviation of the bearing surface, $\sigma = 0.251$ µm, this represents a difference of approximately 0.4 in the dimensionless surface separation ($\frac{h}{\sigma}$). Figure 25 summarizes the mean, minimum, and maximum MOFT obtained with the different contact models for the representative crank angle intervals $660 - 780°$ and $840 - 960°$. In the crank angle interval $660 - 780°$, the CEB model appears with the highest mean and the lowest minimum MOFT, which is probably related to the higher MOFT values reached in this crank angle interval, as can be seen in the journal orbit in Figure 23 (b); the GW model appears with the highest minimum MOFT in this crank angle interval. On the other hand, the mean, maximum and minimum MOFT are close for all contact models in the crank angle interval $840 - 960°$, indicating low dispersion, as shown in Table 9. The tendency among the models was quite similar to that observed in other crank angle intervals, with the CEB and the GW models presenting the lowest and highest MOFT, respectively.

Calculated kinematic parameters of the clearance joint, such as the eccentricity ratio (ϵ) and its time derivative ($\dot{\epsilon}$), are also shown in Figure 24 (a) and (b). A great variation in the transition intervals can be seen for these parameters. The eccentricity ratio reached values greater than 0.99 in the crank angle intervals $360° - 420°$, $660° - 780°$ and $1020° - 1080°$. In crank angle intervals $660 - 780°$ and $840 - 960°$, it was near this value but still just below. The time derivative of the eccentricity ratio presented peaks from -20×10^3 1/s to 10×10^3 1/s in the crank angle intervals $360 - 420°$, $660 - 780°$ and $1020 - 1080°$.

Figure 26 presents the MOFT percentage variation obtained through the rough elastoplastic contact models taking as base the mean and minimum values obtained by the GW elastic model (a) and (b) and the mean and minimum normalized surface separation (h/σ) (c) and (d) for the connecting rod–slider revolute joint (CR–S) in the crank angle intervals $660° - 780°$ and $840° - 960°$, respectively.

Results presented in figure 26 show that the normalized surface approximation mean and minimum values were between 3.5 and 5.0 and 2.0 to 3.0, respectively, in the crank angle interval $660° - 780°$. For the crank angle interval $840° - 960°$, surface separation values were closer one each other, varying between 2.5 and 3.5. It is possible to verify that in the first crank angle interval there was a positive percentage variation of the mean MOFT parameter to the CEB, JG and PW elastoplastic models related to the values obtained by the GW model. Such behavior was different of that obtained to the second

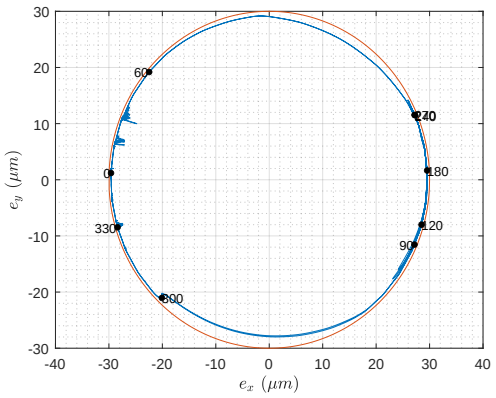

(a) GW

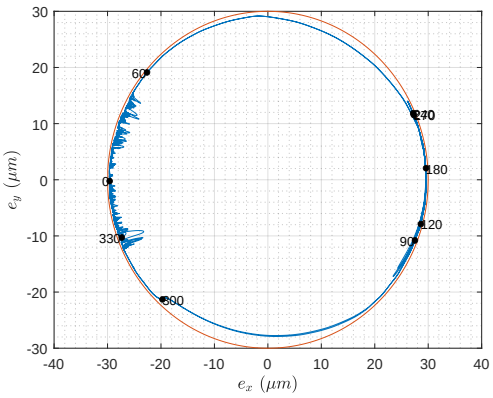

(b) CEB

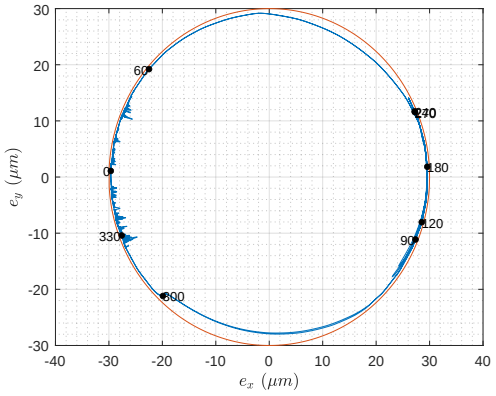

(c) ZMC

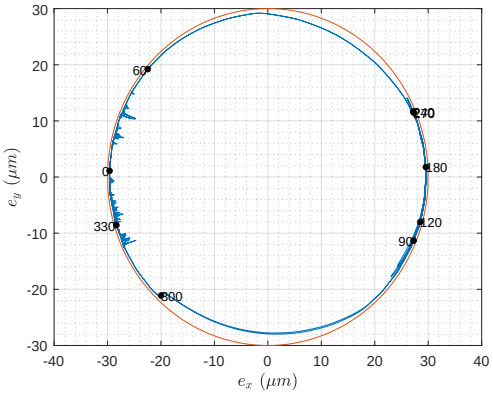

(d) KE

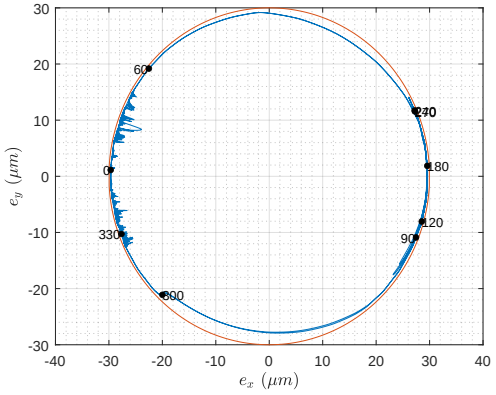

(e) JG

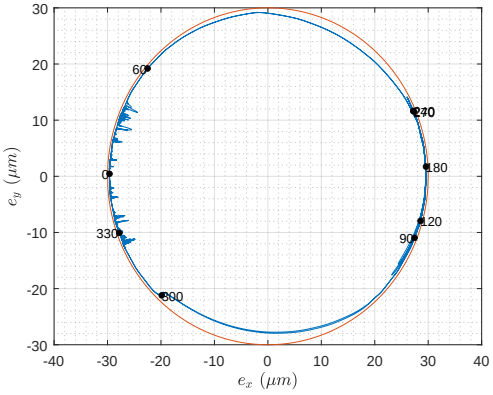

(f) PW

Figure 23 – Journal orbits in the connecting rod–slider revolute joint (CR–S) calculated with the different contact models for the mechanism configuration I.

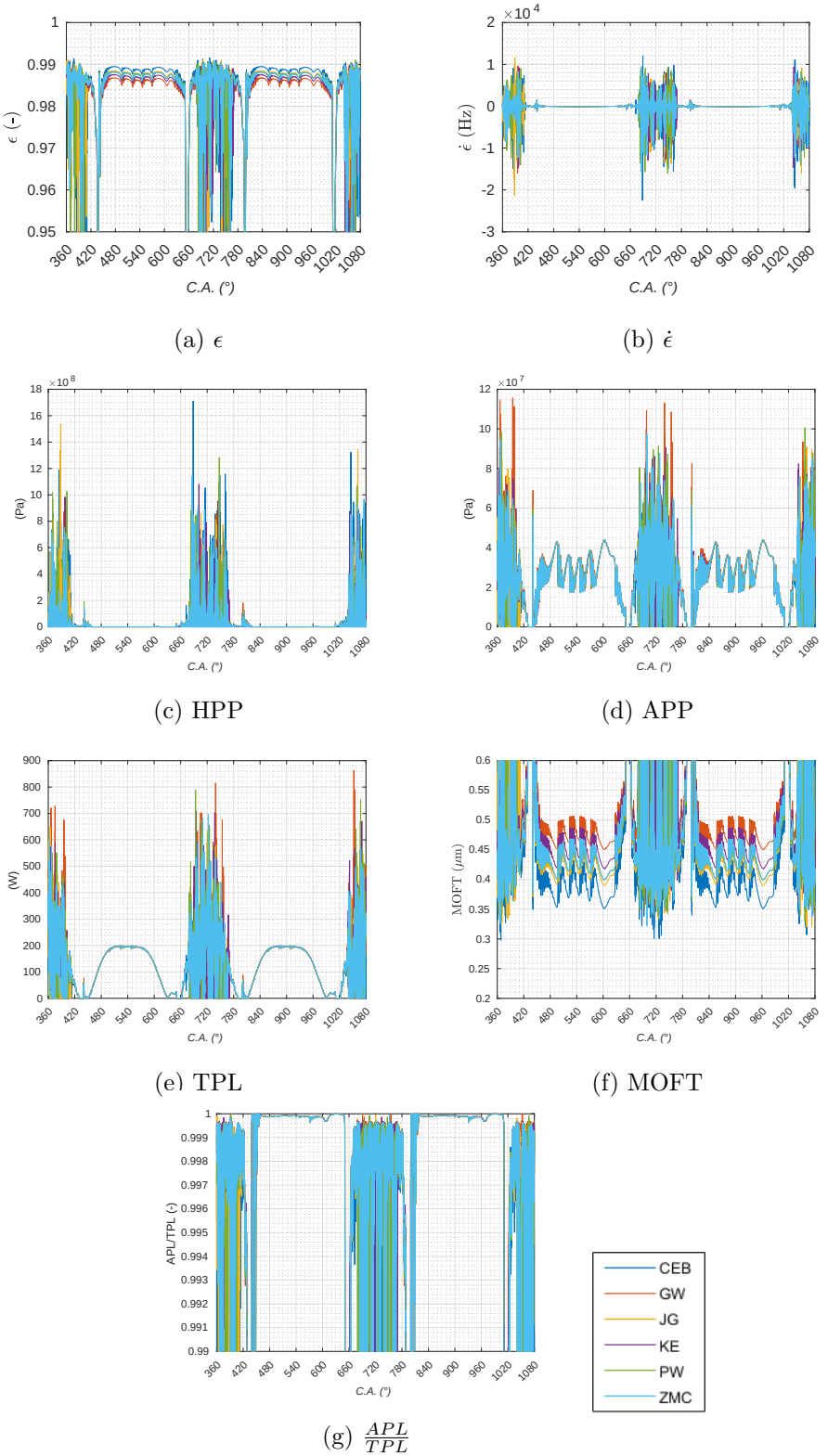

Figure 24 – Lubrication performance of the connecting rod–slider revolute joint (CR–S) for the mechanism configuration I. (a) Eccentricity ratio, (b) Eccentricity ratio velocity, (c) hydrodynamic peak pressure (HPP), (d) asperity contact peak pressure, (e) total power loss (TPL), (f) minimum oil film thickness (MOFT), and (g) asperity-to-total power loss ratio.

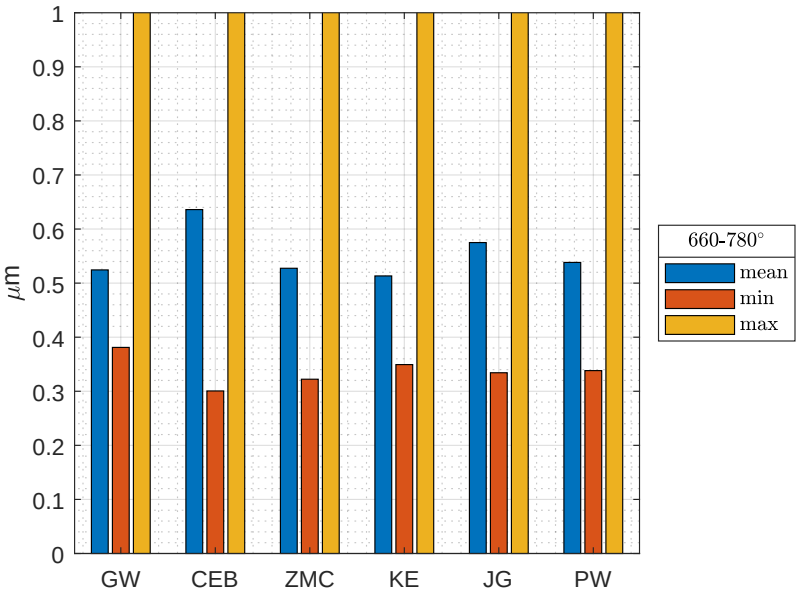

(a) $660 - 780°$

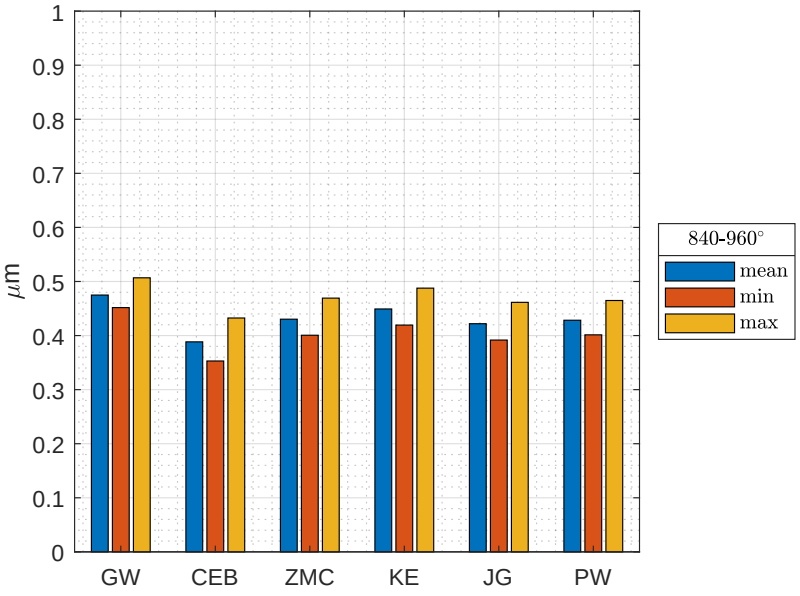

(b) $840 - 960°$

Figure 25 – Mean, minimum and maximum MOFT values in the connecting rod–slider revolute joint (CR–S) in the crank angle intervals $660 - 780°$ and $840 - 960°$ for the mechanism configuration I.

Table 9 – Mean, minimum, maximum and standard deviation of MOFT values in the connecting rod–slider revolute joint (CR–S) in the crank angle intervals $660° - 780°$ and $840° - 960°$ for the mechanism configuration I (values in micrometers).

	Mean	Min	Max	STD
	$660 - 780°$			
GW	0.524	0.381	2.256	0.193
CEB	0.636	0.301	5.008	0.407
ZMC	0.527	0.322	3.116	0.220
KE	0.513	0.349	2.163	0.179
JG	0.575	0.334	2.839	0.299
PW	0.538	0.338	3.172	0.300
	$840 - 960°$			
GW	0.475	0.452	0.507	0.014
CEB	0.388	0.353	0.432	0.020
ZMC	0.430	0.401	0.469	0.018
KE	0.449	0.419	0.488	0.017
JG	0.422	0.392	0.461	0.018
PW	0.428	0.401	0.465	0.016

crank angle interval, when the MOFT variation for all the elastoplastic models presented a decrease if compared with the results obtained in the GW elastic model. The greatest difference in percentage variation of MOFT related to the elastic GW model was obtained when applying the CEB model, reaching +20% and -20% for the average and minimum MOFT, respectively.

4.1.2 Dynamic Response

Figure 27 presents the linear and angular positions, velocities and accelerations of the slider and connecting rod for each contact model evaluated. Analyzing the results of the connecting rod angle and slider position and their respective velocities in a macro view, it is possible to conclude that there were no major differences between the results obtained with the contact models compared with the case with perfect joint. On the other hand, it was predicted a wide variation in the acceleration of the connecting rod and slider in the crank angle intervals $360° - 420°$, $660° - 780°$ and $1020° - 1080°$.

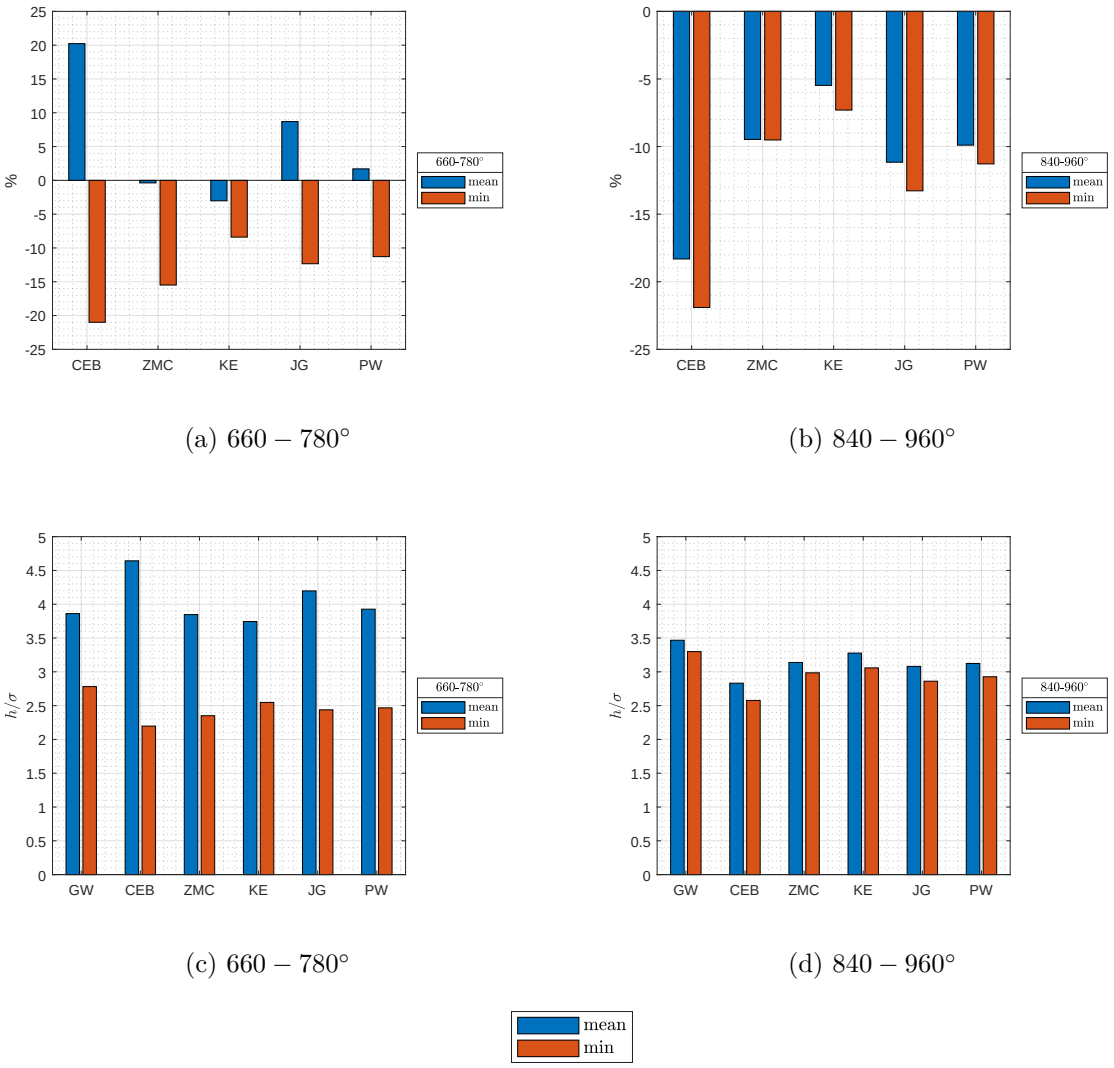

(a) $660 - 780°$

(b) $840 - 960°$

(c) $660 - 780°$

(d) $840 - 960°$

Figure 26 – MOFT percentage variation of the elastoplastic rough contact models and surface approximation (h'/σ) values in the connecting rod–slider revolute joint (CR–S) in the crank angle intervals $660° - 780°$ and $840° - 960°$ for the mechanism configuration I

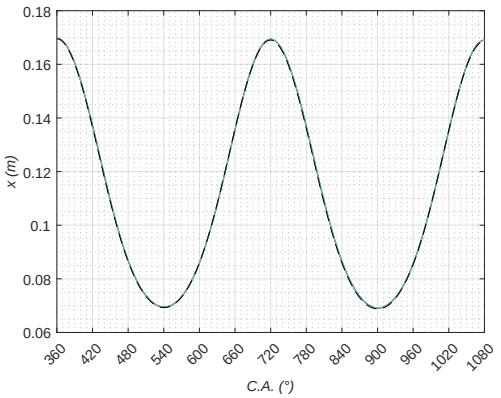

(a) x_S

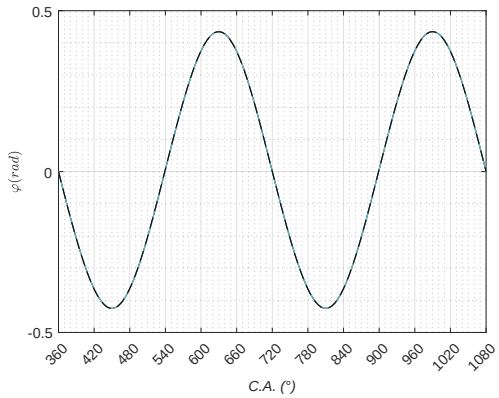

(b) φ_{CR}

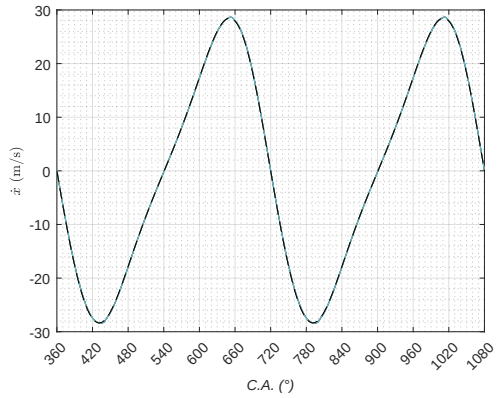

(c) $\dot{x}_S$

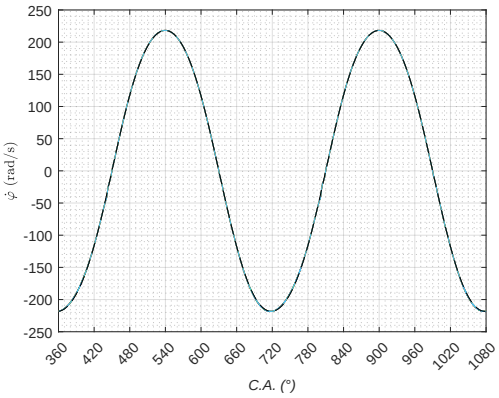

(d) $\dot{\varphi}_{CR}$

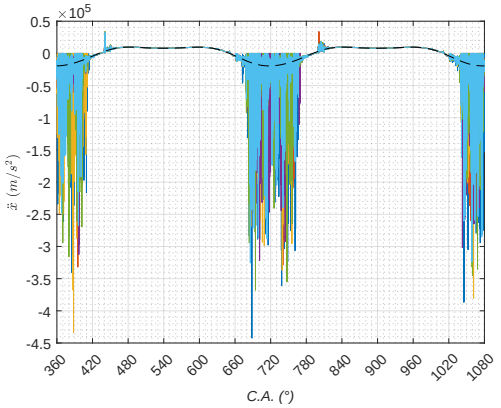

(e) $\ddot{x}_S$

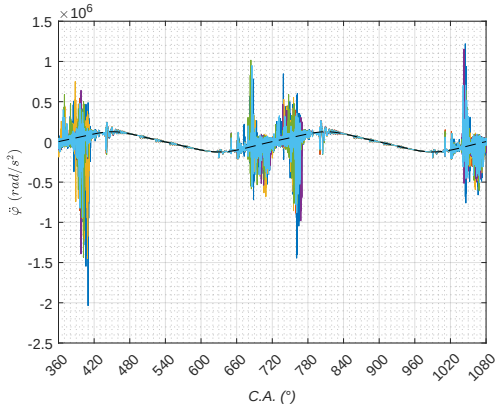

(f) $\ddot{\varphi}_{CR}$

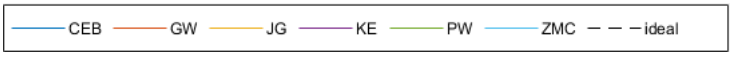

Figure 27 – Linear and angular positions, velocities and accelerations of the slider and connecting rod for the mechanism configuration I.

4.2 Mechanism Configuration II

4.2.1 Lubrication Performance

Figures 28 and 29 present the journal orbits in the connecting rod–slider (CR-P) and crankshaft–connecting rod (CS-CR) joints calculated with the different contact models evaluated. The journal orbits in the CS-CR and CR-S joints were smooth for all contact models. Since the time step used in this joint configuration was the same as that used in the mechanism configuration I, it seems that the consideration of the clearance in the CS-CR joint minimized the local fluctuations in the eccentricity of the CR-S joint previously predicted with the elastoplastic models for the joint configuration I. Furthermore, the orbits calculated in configuration II were closer to the clearance circle when compared with the same results for mechanism configuration I. The journal orbit of the CS-CR joint starts from the left side, goes toward the right, bordering the bottom perimeter, and closes the cycle, returning to the left side by the top.

Figures 30 and 31 show, respectively, the results of the bearing performance parameters of the CR-S and CS-CR joints. Similarly to what occurred in the configuration I, it is possible to notice a wide variation in the parameters in the transition intervals of the displayed cycles. Looking at Figure 30 (c), we can note that the highest hydrodynamic peak pressures in the CR-S joint occurred in the crank angle intervals $360° - 420°$, $660° - 780°$ and $1020° - 1080°$, reaching values higher than 0.3 GPa at some points when using the CEB model. Compared with the same results of the configuration I, a significant decrease in the peak pressures occurred in those crank angle intervals, indicating that the consideration of the clearance in the CS-CR joint may have caused an improved damping response of the CR-S joint. The journal orbits shown in Figure 28 corroborate this assumption, displaying almost no local fluctuation in the journal trajectory. In the crank angle intervals $480° - 600°$ and $840° - 960°$, the hydrodynamic peak pressures were very low, and the asperity peak pressures increased in the bearing domain.

The results in Figure 31 (c) show the hydrodynamic peak pressures in the CS-CR joint. Values reached their maximum near the crank angles 360°, 720° and 1080°, with peaks above 0.4 GPa when using the CEB model. It is noted a variation in the peak pressures in the crank angle intervals $360° - 420°$, $660° - 780°$ and $1020° - 1080°$, with increasing and decreasing values ranging from 0 to 0.3 GPa. An interesting difference when comparing with the CR-S joint is that even in smaller magnitudes, the hydrodynamic peak pressures in the crank angle intervals $480° - 600°$ and $840° - 960°$ are not very low, keeping a mean value of approximately 0.05 GPa.

Regarding the results presented in Figure 30 (d) for the asperity peak pressures in the CR-S joint, some small differences between the contact models begin to emerge. It can be seen that the GW model predicted higher peak pressures compared with the

other models. This is more prominent at the beginning and end of the cycles ($360° - 420°$, $660° - 780°$ and $1020° - 1080°$). When using the GW model, the asperity peak pressures in those crank angle intervals reached values just above 0.07 GPa. Regarding the behavior of the other contact models, one has the PW, KE, ZMC, JG and CEB models in descending order of magnitude for the maximum asperity peak pressure. In configuration I, some asperity peak pressures exceeded 0.1 GPa, while in configuration II, they reached values of just above 0.07, indicating a slight decrease in contact intensity. In the crank angle intervals $480° - 600°$ and $840° - 960°$, the asperity peak pressures were very close when using the different contact models. The results depicted in Figure 30 (g) show that the asperity power loss is higher in the crank angle interval $450° - 630°$.

Another characteristic observed for the CR-S joint is that in the mechanism configuration I, there was a more significant variation in the amplitude of the asperity peak pressures, ranging from 0 to 0.113 GPa in the crank angle interval $660 - 780°$ with the GW model. In contrast, this range in the configuration II was approximately 0.006-0.058 GPa and 0.012-0.071 GPa when using the CEB and GW models, respectively.

Analyzing the results in Figure 31 (d) for the asperity peak pressures in the CS-CR joint, it is evident the differences among the contact models. The maximum asperity peak pressures reached the values of just above 0.07 GPa at the crank angles 360°, 720° and 1080° with the GW model. The CEB and GW models yielded the lowest and highest mean asperity peak pressures of 0.024 GPa and 0.036 GPa in the crank angle interval $660° - 780°$. In the crank angle interval $840° - 960°$, the maximum asperity peak pressures for the CEB and GW models were 0.025 and 0.032 GPa, respectively.

Comparing the results in Figure 30 (e) and Figure 24 (e) for the total power losses in the CR-S joint, it is possible to notice a decrease from peaks of 800 W in the mechanism configuration I, to peaks of 400 W at the crank angles 360°, 720° and 1080°, and below 200 W at the crank angles 540° and 900°, in configuration II. Asperity contact dissipation was the main contributor to the total power losses. As displayed in Figure 31 (e), the CS-CR joint also showed the maximum total power losses near the crank angles mentioned above. In this joint, the maximum power losses predicted with the GW and CEB models were 1500 W and 1200 W, respectively.

Figure 30 (f) shows the MOFT in the CR-S joint calculated with the different contact models. Similarly to what happened in configuration I, it is possible to notice that the GW model predicted the highest MOFT values and the CEB model the lowest ones. However, in the joint configuration II, a decrease in the dispersion of the MOFT in the crank angle intervals $360° - 420°$, $660° - 780°$ and $1020° - 1080°$ is observed, as can be analyzed from the results in Figures 28, 25 and 32. Furthermore, the minimum MOFT values obtained using the CEB and other models were slightly higher than those predicted in configuration I.

Table 10 – Mean, minimum, maximum and standard deviation of MOFT values in the connecting rod–slider revolute joint (CR–S) in the crank angle intervals $660 - 780°$ and $840 - 960°$ for the mechanism configuration II (values in micrometers).

	Mean	Min	Max	STD
$660 - 780°$				
GW	0.459	0.417	0.527	0.021
CEB	0.378	0.320	0.511	0.027
ZMC	0.414	0.365	0.494	0.025
KE	0.431	0.383	0.511	0.025
JG	0.407	0.356	0.488	0.025
PW	0.414	0.367	0.489	0.024
$840 - 960°$				
GW	0.474	0.453	0.507	0.013
CEB	0.388	0.354	0.432	0.019
ZMC	0.429	0.402	0.468	0.016
KE	0.448	0.420	0.486	0.016
JG	0.420	0.392	0.461	0.017
PW	0.427	0.403	0.464	0.015

Regarding the kinematic parameters of the CR-S joint, the time derivative of the eccentricity ratio ($\dot{\epsilon}$), shown in Figure 30 (b), had lower peaks than in configuration I. The peaks occurred in the crank angle intervals $360° - 420°$, $660° - 780°$ and $1020° - 1080°$, with values ranging from -5×10^3 1/s to 5×10^3 1/s. The behavior of this parameter was an important factor in obtaining more uniform results of MOFT and hydrodynamic and asperity peak pressures in configuration II.

Based on the results in Figure 30, we can observe a sequence of high-frequency events of contact and noncontact in the CR-S joint in the crank angle intervals $360° - 420°$, $660° - 780°$ and $1020° - 1080°$. These events caused a wide variation in the hydrodynamic and contact peak pressures and power losses. This condition was more pronounced in configuration I, where the hydrodynamic and asperity peak pressures had a higher amplitude variation.

Figures 34 and 35 present the MOFT percentage variation obtained through the rough elastoplastic contact models taking as base the mean and minimum values obtained by the GW elastic model and the mean and minimum normalized surface separation (h/σ) for the connecting rod–slider revolute (CR–S) and crankshaft–connecting rod (CS–CR) joints in the crank angle intervals $660° - 780°$ and $840° - 960°$, respectively.

Results presented in figure 34 show that the normalized surface approximation mean and minimum values were between 2.5 and 3.5 and 2.0 to 3.0, respectively, in the crank angle interval $660° - 780°$. If compared to the configuration I, these values were slightly lower than those results and the mean and minimum values were more closer one each other. The greatest difference in percentage variation of MOFT related to the elastic

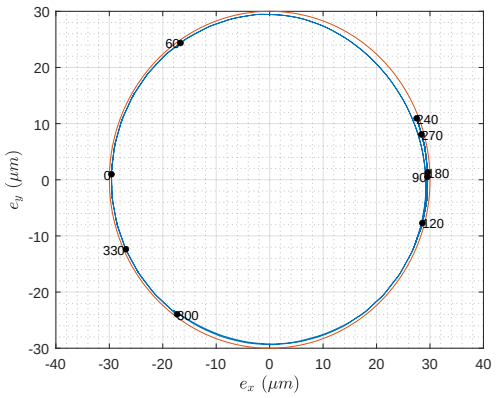

(a) GW

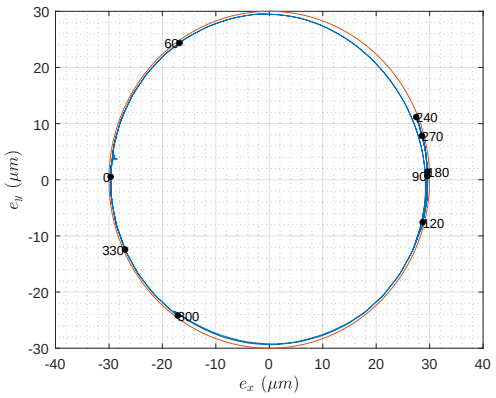

(b) CEB

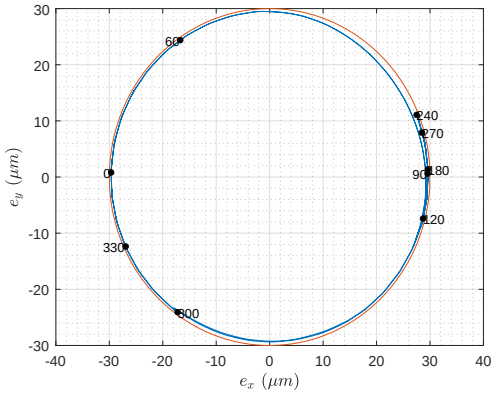

(c) ZMC

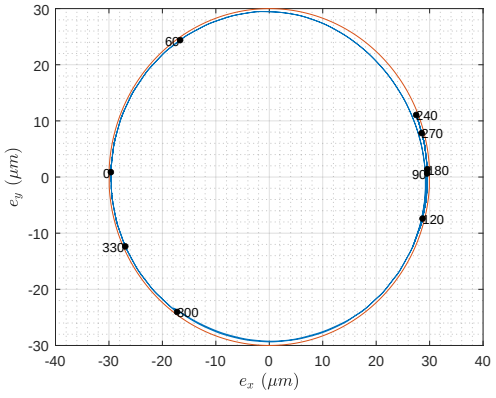

(d) KE

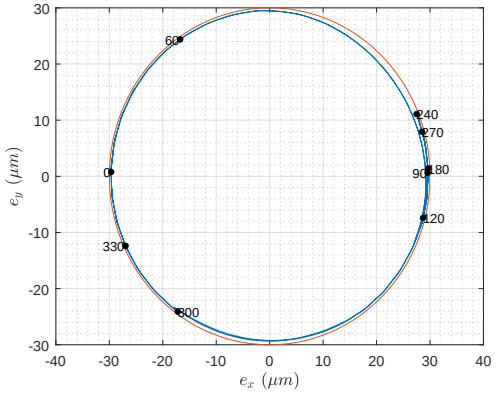

(e) JG

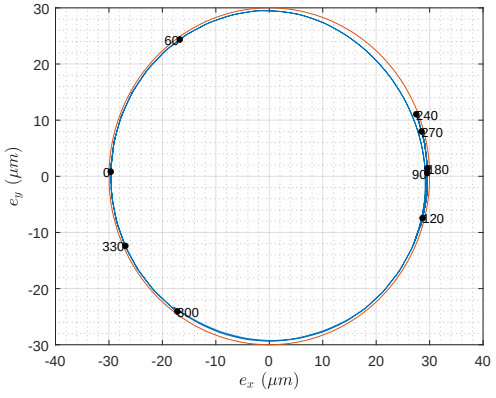

(f) PW

Figure 28 – Journal orbits in the connecting rod–slider revolute joint (CR–S) calculated with the different contact models for the mechanism configuration II.

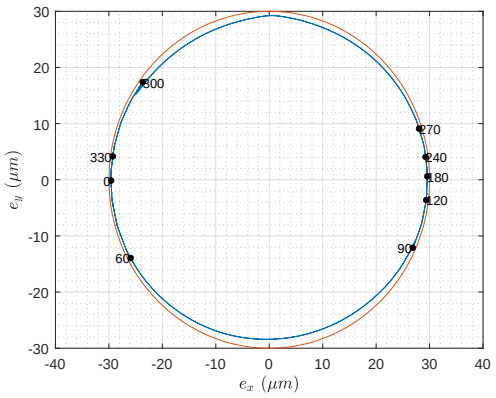

(a) GW

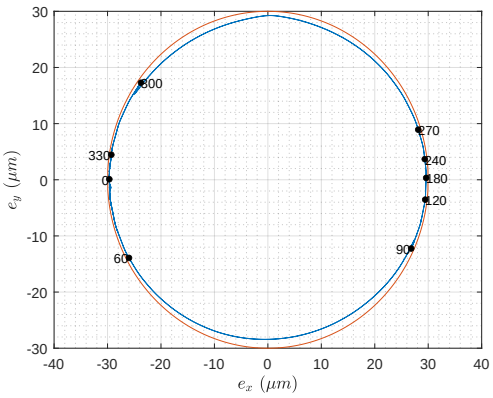

(b) CEB

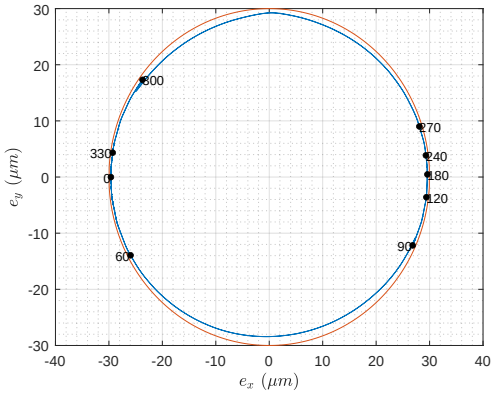

(c) ZMC

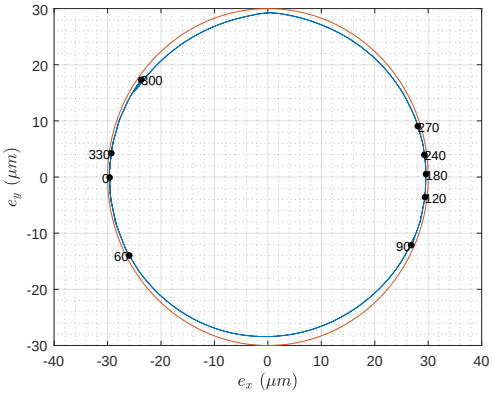

(d) KE

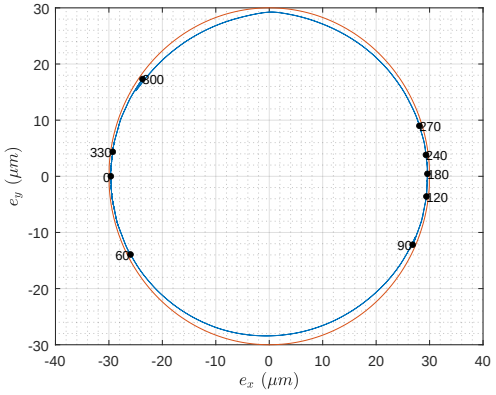

(e) JG

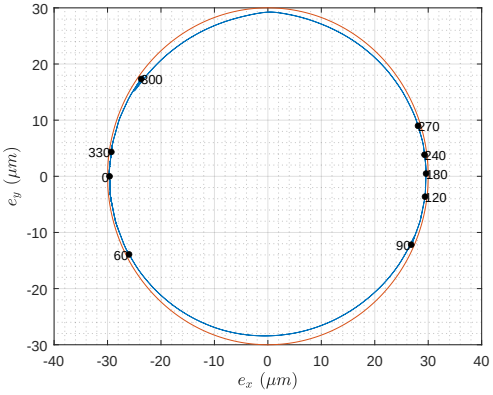

(f) PW

Figure 29 – Journal orbits in the crankshaft–connecting rod revolute joint (CS–CR) calculated with the different contact models for the mechanism configuration II.

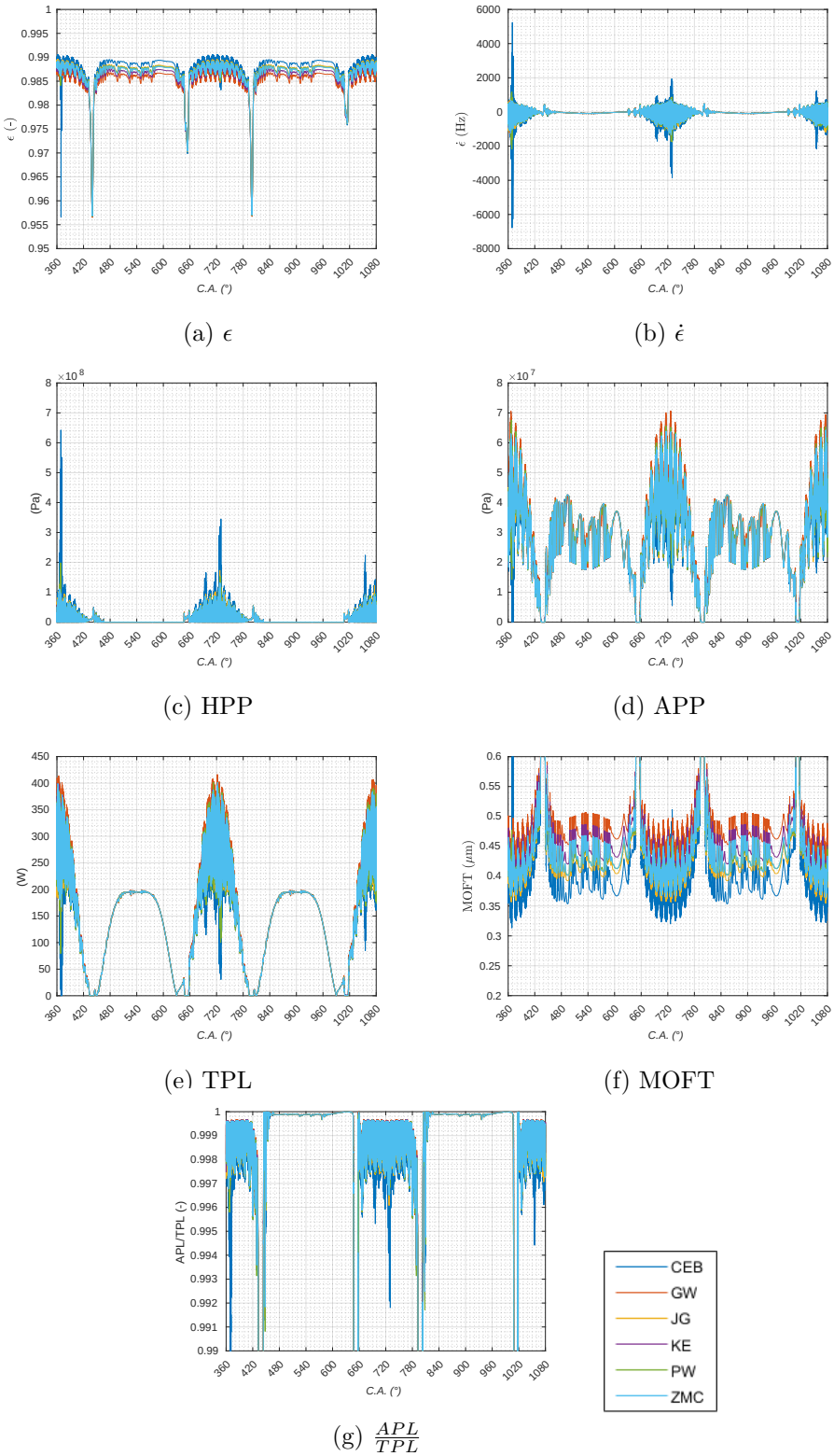

Figure 30 – Lubrication performance of the connecting rod–slider revolute joint (CR–S) for the mechanism configuration II. (a) Eccentricity ratio, (b) Eccentricity ratio velocity, (c) hydrodynamic peak pressure (HPP), (d) asperity contact peak pressure, (e) total power loss (TPL), (f) minimum oil film thickness (MOFT), and (g) asperity-to-total power loss ratio.

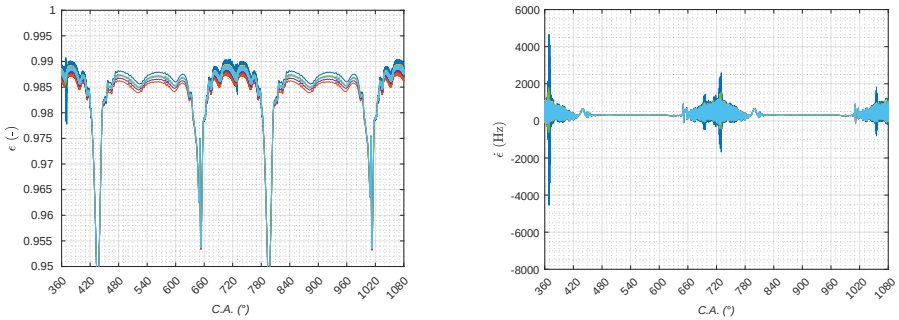

(a) ϵ

(b) $\dot{\epsilon}$

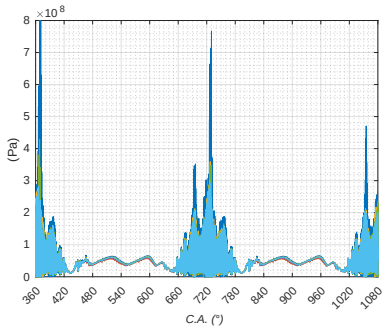

(c) HPP

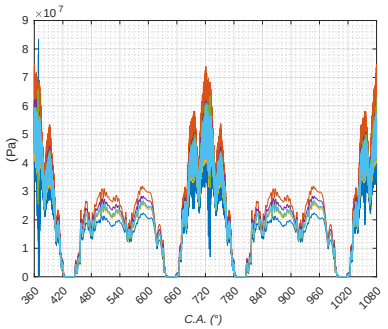

(d) APP

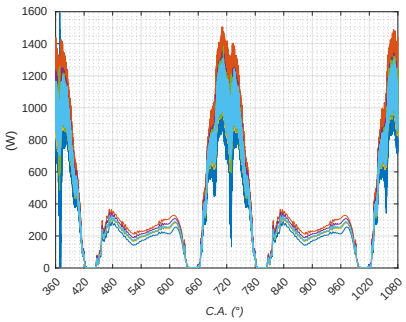

(e) TPL

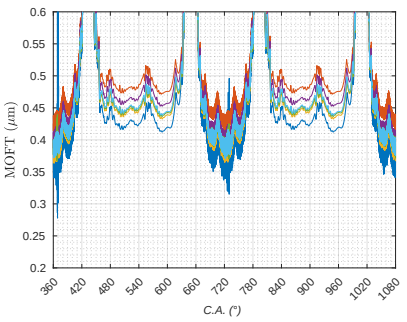

(f) MOFT

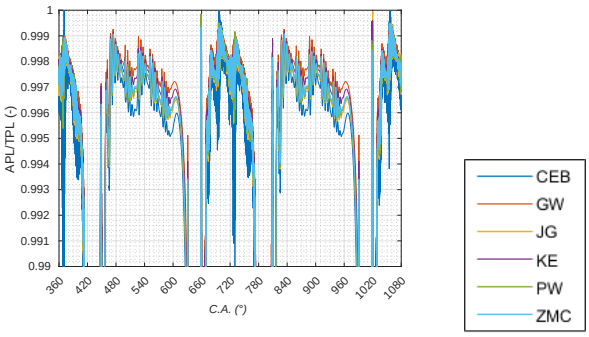

(g) $\frac{APL}{TPL}$

Figure 31 – Lubrication performance of the crankshaft–connecting rod revolute joint (CS–CR) for the mechanism configuration II. (a) Eccentricity ratio, (b) Eccentricity ratio velocity, (c) hydrodynamic peak pressure (HPP), (d) asperity contact peak pressure, (e) total power loss (TPL), (f) minimum oil film thickness (MOFT), and (g) asperity-to-total power loss ratio.

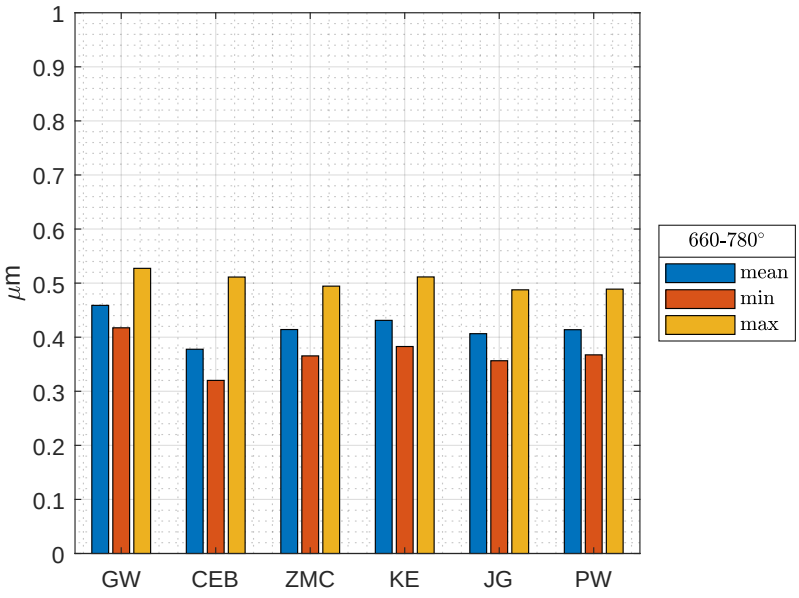

(a) $660 - 780°$

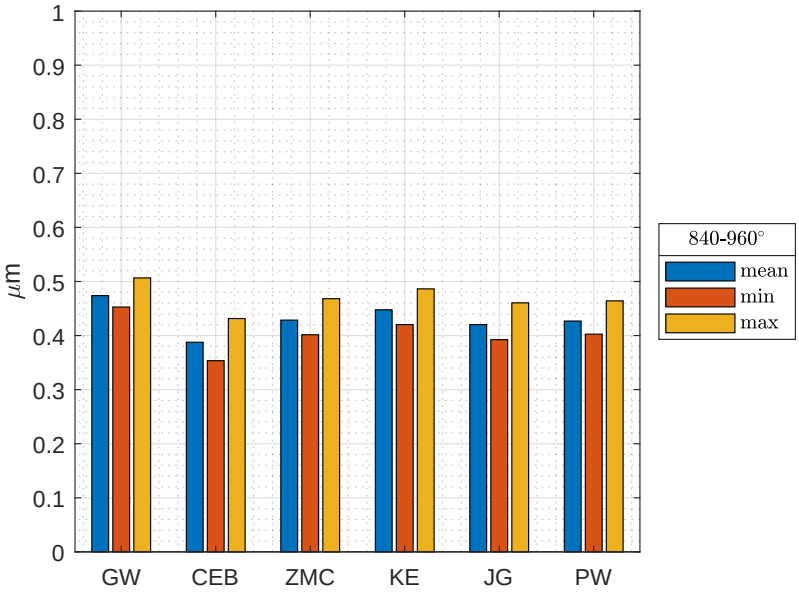

(b) $840 - 960°$

Figure 32 – Mean, minimum and maximum MOFT values in the connecting rod–slider revolute joint (CR–S) in the crank angle intervals $660 - 780°$ and $840 - 960°$ for the mechanism configuration II.

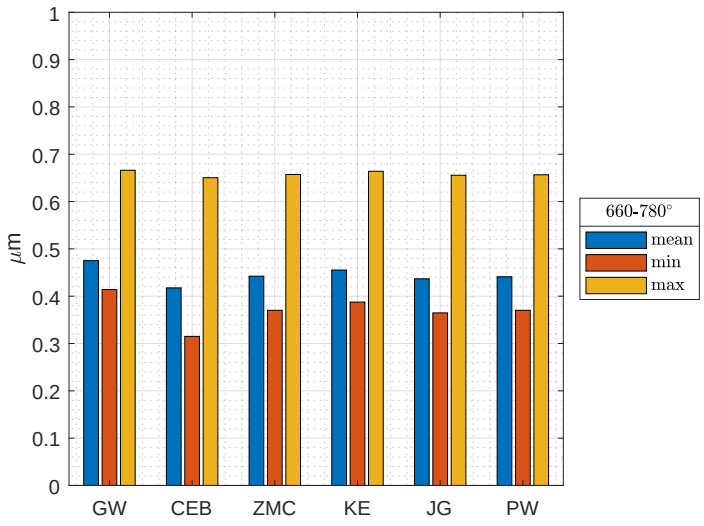

(a) $660 - 780°$

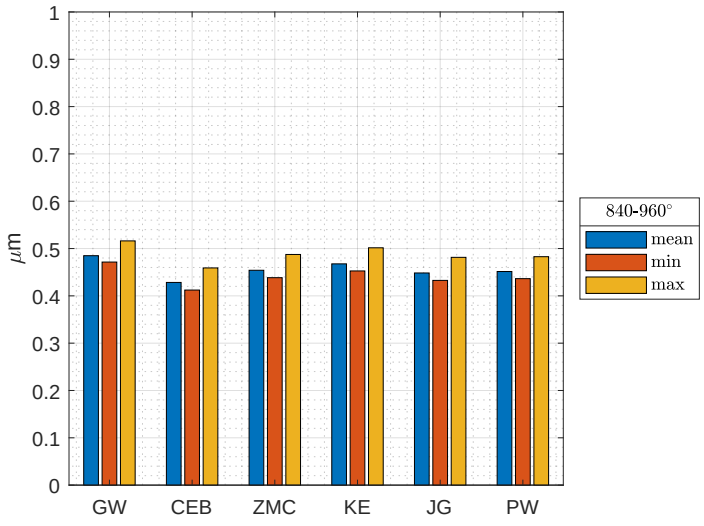

(b) $840 - 960°$

Figure 33 – Mean, minimum and maximum MOFT values in the crankshaft–connecting rod revolute joint (CS–CR) in the crank angle intervals $660 - 780°$ and $840 - 960°$ for the mechanism configuration II.

Table 11 – Mean, minimum, maximum and standard deviation of MOFT values in the crankshaft–connecting rod revolute joint (CS–CR) in the crank angle intervals $660 - 780°$ and $840 - 960°$ for the mechanism configuration II (values in micrometers).

	Mean	Min	Max	STD
$660 - 780°$				
GW	0.475	0.414	0.666	0.048
CEB	0.418	0.315	0.650	0.060
ZMC	0.442	0.370	0.657	0.055
KE	0.455	0.388	0.664	0.054
JG	0.437	0.365	0.656	0.056
PW	0.441	0.370	0.657	0.054
$840 - 960°$				
GW	0.485	0.471	0.516	0.011
CEB	0.428	0.412	0.459	0.011
ZMC	0.454	0.438	0.487	0.011
KE	0.468	0.453	0.502	0.012
JG	0.448	0.433	0.481	0.011
PW	0.451	0.436	0.483	0.011

GW model was obtained when applying the CEB model, reaching almost -24% followed by the JG model with a result of almost -15% for the minimum MOFT. In the crank angle interval $840° - 960°$, surface separation values were closer between mean and minimum noemalized surface separation, varying between 2.5 and 3.5.

4.2.2 Dynamic Response

Figure 36 presents the linear and angular positions, velocities and accelerations of the slider and connecting rod for each evaluated contact model.

Similar to what occurred in the joint configuration I, the acceleration of the connecting rod and slider varied with more intensity in the crank angle intervals $360° - 420°$, $660° - 780°$ and $1020° - 1080°$. The angular acceleration of the connecting rod reached peaks between $-0.5 \times 10^6\,\mathrm{rad/s^2}$ and $0.6 \times 10^6\,\mathrm{rad/s^2}$, while the linear acceleration of the slider reached a minimum of $-0.18 \times 10^6\,\mathrm{m/s^2}$ just after the angle of 360°. The acceleration response of the system improved slightly in the mechanism configuration II, with a lower amplitude of variation in these intervals compared to configuration I.

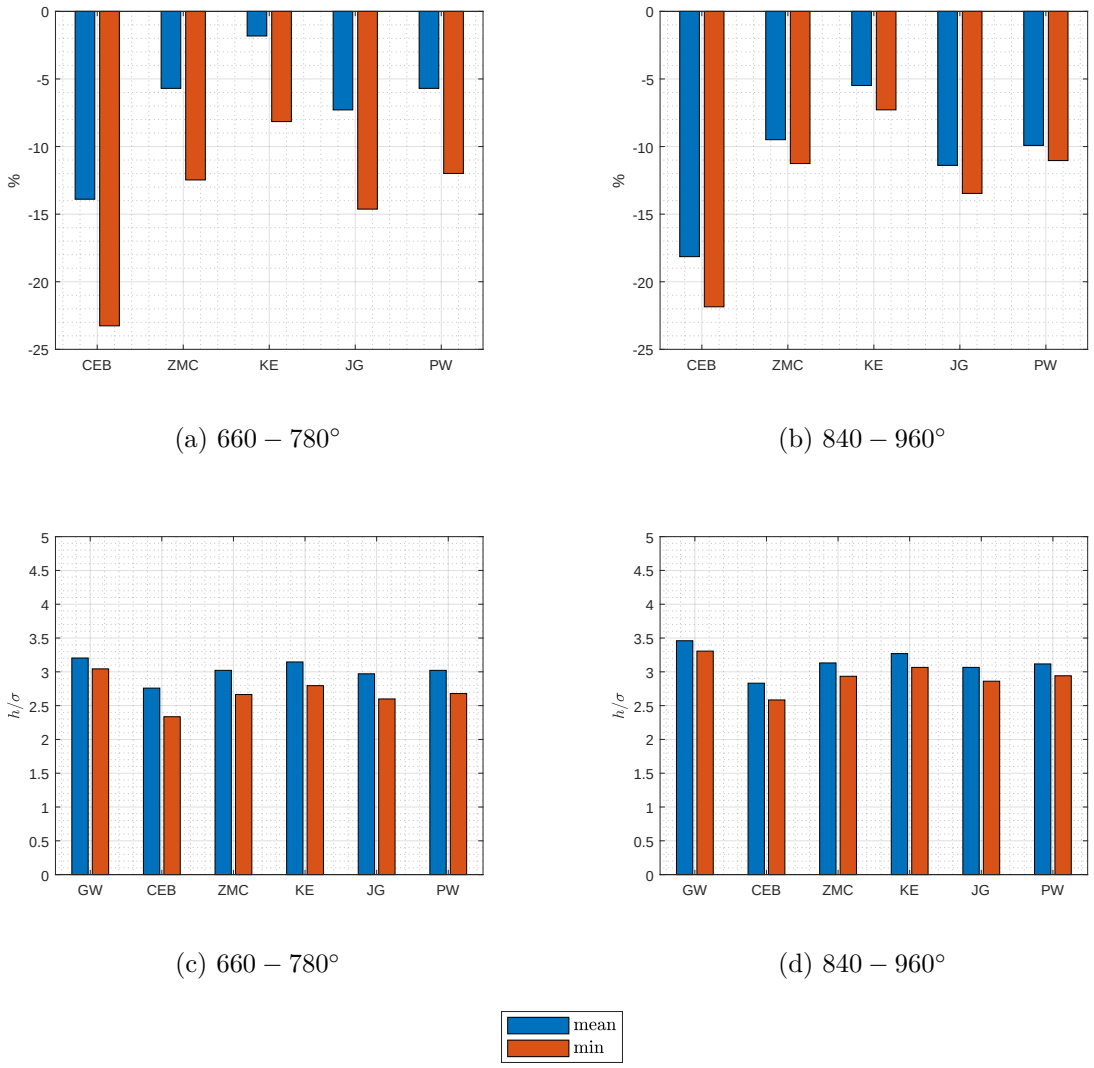

(a) $660 - 780°$

(b) $840 - 960°$

(c) $660 - 780°$

(d) $840 - 960°$

Figure 34 – MOFT percentage variation of the elastoplastic rough contact models and surface approximation (h'/σ) values in the connecting rod–slider revolute joint (CR–S) in the crank angle intervals $660° - 780°$ and $840° - 960°$ for the mechanism configuration II.

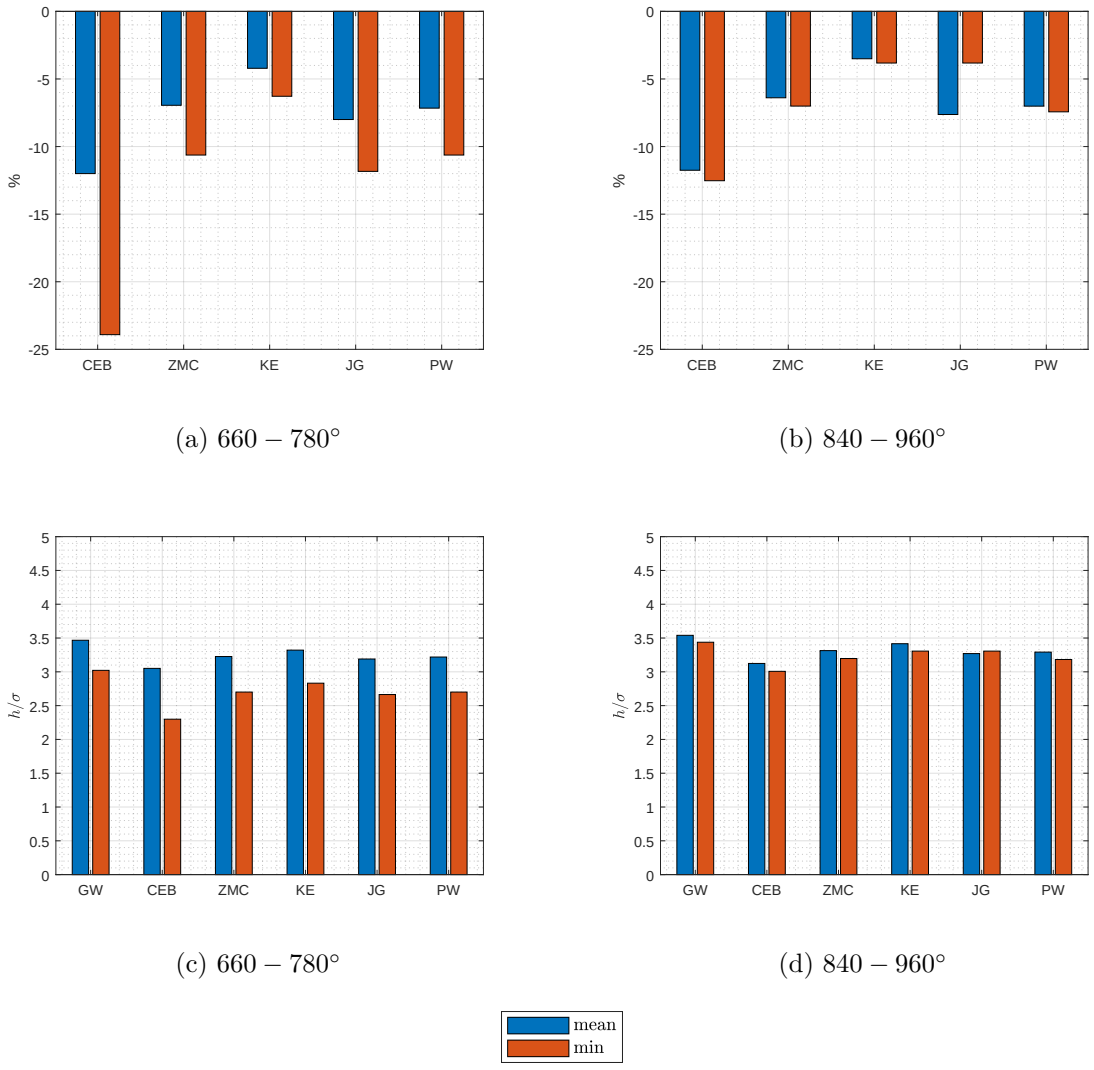

(a) $660 - 780°$

(b) $840 - 960°$

(c) $660 - 780°$

(d) $840 - 960°$

Figure 35 – MOFT percentage variation of the elastoplastic rough contact models and surface approximation (h'/σ) values in the crankshaft–connecting rod revolute joint (CS–CR) in the crank angle intervals $660° - 780°$ and $840° - 960°$ for the mechanism configuration II.

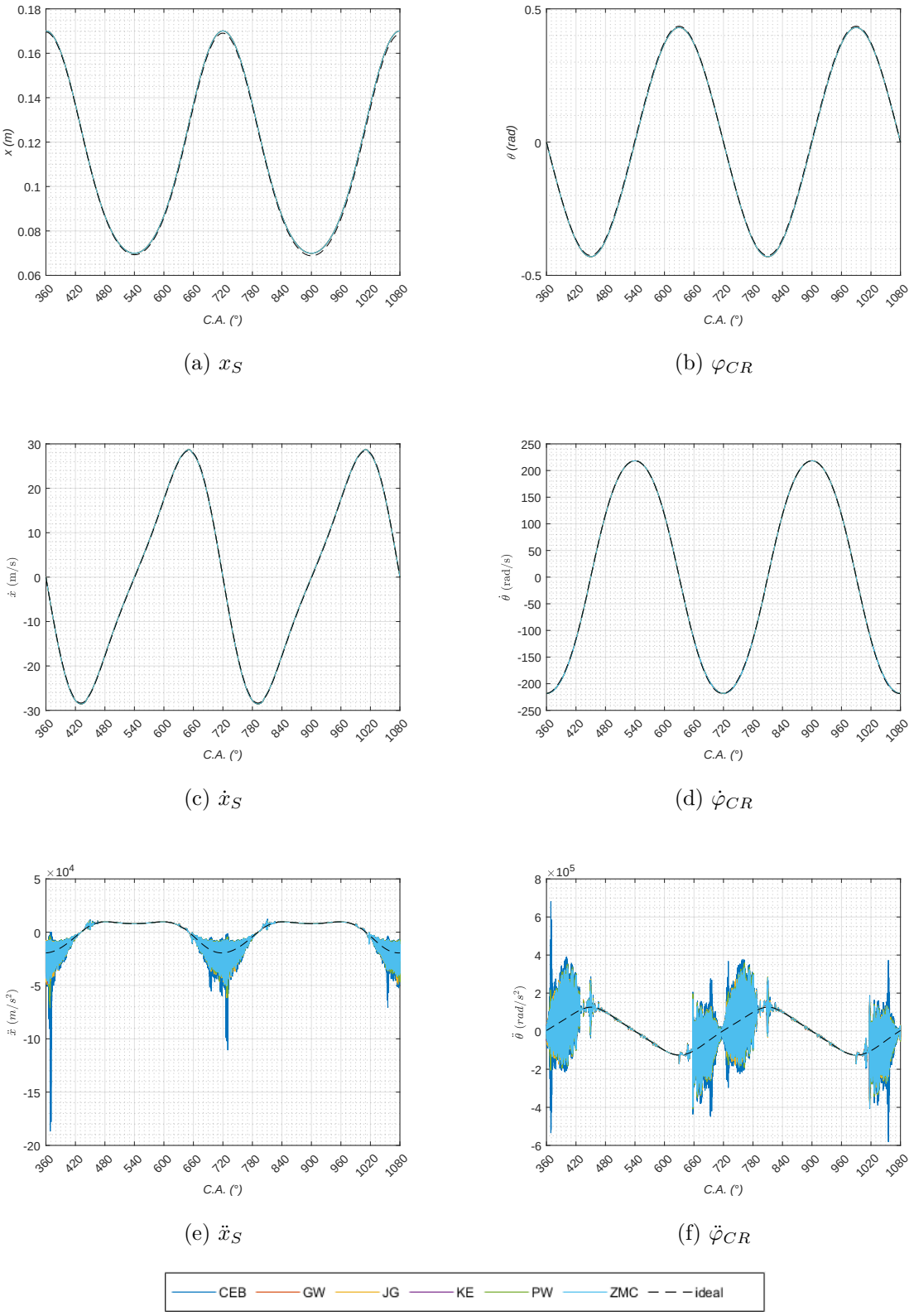

(a) x_S

(b) φ_{CR}

(c) $\dot{x}_S$

(d) $\dot{\varphi}_{CR}$

(e) $\ddot{x}_S$

(f) $\ddot{\varphi}_{CR}$

Figure 36 – Linear and angular positions, velocities and accelerations of the slider and connecting rod for the joint configuration II.

4.3 Mechanism Configuration III

4.3.1 Lubrication Performance

Figures 37, 38 and 39 present the orbit movement of the connecting rod-slider (CR-P), crankshaft-connecting rod (CS-CR) and block-crankshaft joints according to the contact models used in the simulation.

In this configuration, from the Figures 37, 38 and 39, results of orbit movement for all the revolute joints obtained by the contact models were smooth in the simulation. Particularly to the B-CS joint, the orbit movement was concentrated in the joint left side moving up and down almost until the top and bottom of the joint clearance limit. Also, only looking the orbit movement, this joint seems to make an intense contact since the movement happened very close to the clearance limit. The orbit movement of the CS-CR and CR-P joints were very closed with that obtained in the configuration II excepted some minor changes in the orbit position according to the crankshaft angle.

Figures 40, 41 and 42 show the results of the bearing parameters obtained by the rough contact models to the CR-P, CS-CR and B-CS joints, respectively. From these results, in a similar way to what occurs in the other configurations, a wide variation of the values occur during the first and last 60° of the crankshaft angle in the cycle.

Looking at the Figure 40 (c), we can observe hydrodynamic peak pressures in the crankshaft angle intervals $360-420°$, $660-780°$ and $1020-1080°$ reaching peak values above of 0.4 GPa in some points. Immediately before the crankshaft angles 720° and 1080° the peaks reach values of about 1 GPa. Excepting the punctual high peaks, we can note a tendency of increasing beginning in 60° before finish the cycle, reaching the value of almost 0.2 GPa, and decreasing this value during the first 60° in the other cycle. Making a brief comparison with the results presented in Figure 30 (c), at the configuration II, there was an increase of the values, but it was still lower than the values presented in Figure 24 (c), at the configuration I. About the results for asperity peak pressure, presented in Figure 40 (d), and compared to the results obtained in the other configurations, presented in Figures 24 (d) and 30 (d), there is an increase of the frequency of values variation in the crankshaft angle intervals of $450-630°$ and $810-990°$. Also, when compared with the results obtained in configuration II, these were higher than the values obtained in that configuration and they are somewhat similar to those obtained in configuration I but with fewer peaks of asperity pressure. The increase in the frequency of value variation is also clearly observed in the MOFT results for the different contact models, in Figure 40 (f) and in the results presented in Figure 40 (a), for the eccentricity. The elastic GW model presented the higher values of MOFT and CEB model, the smaller. In this configuration, the CEB model has presented local MOFT minimum values below 0.3 0.3 µm near the 720° crankshaft angle. In Figure 40 (e), total power loss in the CR-S joint reached a peak value of almost 1000

W in the $660 - 780°$ crankshaft angle interval when using the ZMC model. An interesting difference noted in this figure, compared to the other configurations, is the increase in the amplitude variation in the crankshaft angle intervals of $480 - 600°$ and $840 - 960°$ around the value of 200 W. The result of the dynamic parameter $\dot{\epsilon}$ presented in Figure 40 (b) had an increase in the angle intervals of $360 - 420°$, $660 - 780°$ and $1020 - 1080°$ compared to configuration II, but was still lower than the values in configuration I. The peak values were just below -10 10^3 Hz and above 7 10^3 Hz with a uniform increase and decrease in the $660 - 780°$ angle interval. Unlike the results in the other configurations, there is an increase in the variation of the values during the angle intervals of the $450 - 630°$ and $810 - 990°$.

To the CS-CR joint, when comparing with the results in configuration II for the eccentricity rate ϵ and its time derivative $\dot{\epsilon}$, presented in Figure 41 (a) and (b), there was an increase of the values and the frequency of variation. A slight increase in the eccentricity rate values ϵ, reaching peak values of 0.992 near the angle of 720° and 1080°, and an increase in the magnitude of the values for the eccentricity time rate $\dot{\epsilon}$ in the crankshaft angle intervals of $360 - 420°$, $660 - 780°$ and $1020 - 1080°$ were observed. The behavior for both these parameters was not as smooth as in configuration II. These dynamical results contributed to an increase in the value of the CS-CR joint parameters, such as the asperity and hydrodynamic peak pressures and power losses and, consequently the decrease of the MOFT values. About the MOFT, results presented in Figure 41 (f) and compared with those obtained in the configuration II, presented in Figure 31 (f), there was a slight decrease in the mean, minimum and maximum values for all the contact models in the $840 - 960°$ crankshaft angle interval in configuration III, being GW and CEB models with the higher and smaller minimum value of MOFT, 0.439 and 0.372 μm, respectively. For the crankshaft angle interval of $660 - 780°$, the values were more disperse with the minimum MOFT value of 0.268 and 0.369 μm obtained using the CEB and GW models, respectively. Values of hydrodynamic and asperity peak pressures, in Figure 41 (c) and (d) also presented a considerable increase when compared with that obtained in configuration II, which results are showed in Figure 31 (c) and (d). For the hydrodynamic peak pressure, values reach their maximum near the 360°, 720° and 1080° crankshaft angles with peaks of about 0.8, 1.3 and 1.0 GPa, respectively, when using the KE and ZMC models. It is noted a variation of the values in the $360 - 420°$, $660 - 780°$ and $1020 - 1080°$ crankshaft angle intervals increasing and decreasing in the pressure interval of usually 0 to 0.4 GPa, excepting the peak values. When comparing with the results to the CS-CR joint in configuration II, it is possible to see an increase of variation around the value of 0.05 GPa in a part of the $480 - 600°$ and $840 - 960°$ angle intervals. Regarding the results of the asperity peak pressure, the differences between the models are well highlighted and the maximum peak value is just above of 0.12 GPa when using the GW model and near the crankshaft angle of 720°. In the $840 - 960°$ crankshaft angle

interval, the higher and smaller values of the maximum total power loss is obtained with the GW and CEB models at the value of about 560 W and 420 W, respectively. In the $660 - 780°$ crankshaft angle interval, these values were 3800 W and 2100 W when using the JG and CEB models, respectively.

Of all the clearance revolute joint in this configuration, the one that presented the most intense contact was the block-crankshaft joint (B-CS). Results in Figure 42 allow us confirm it. The eccentricity and MOFT results, as presented in Figure 42 (a) and (f), were the higher and smaller, respectively, when compared with the other joints. The value of eccentricity rate reached the value of 0.995 in the crankshaft angles of 360°, 720° and 1080° when using the CEB model. The minimum MOFT was obtained with the JG model, in a peak near the angle of 720° with the value of 0.098 μm. But, as we can see in Figure 45 in terms of mean, the use of CEB and GW model presented the minimum and maximum minimum MOFT values, respectively, 0.242 and 0.380 μm in the crankshaft angle interval of $660 - 780°$. For the crankshaft angle interval of $840 - 960°$ these values were 0.269 and 0.400 μm also obtained with the CEB and GW models. Despite the high hydrodynamic pressure peaks observed in Figure 42 (c), and excepting these peaks, asperity peak pressures, as shown in Figure 42 (d), stood out from those, reaching peak values above of 0.3 GPa in the crankshaft angles of 720° and 1080°. As a consequence of the contact more intense, the total power losses were high reaching punctual peak values of more than 5000 W. The maximum values in the crankshaft angle intervals of $660 - 780°$ and $840 - 960°$ were, respectively, 9800 W with the ZMC model and almost 2000 W with the GW model.

From theses results and its respective analysis it is possible to comment that for the case of B-CS joint the difference between the MOFT values were more highlighted mainly because of the contact intensity increased, corroborated by the high values of asperity peak pressure and power losses observed to this joint. Probably the consideration of clearance in this joint with such operational characteristics and bearing geometry created a worse condition to the hole system, in virtue of the results presented in configuration II.

The behavior commented in the results of the configuration II, related to a sequence of contact and non-contact in high frequency, resulting in a wide peaks variation of hydrodynamic and contact peak pressures and power losses, seems to have repeated in this configuration but now, affecting the $480 - 600°$ and $840 - 960°$ crankshaft angle intervals.

Figures 46, 47 and 48 present the MOFT percentage variation obtained through the rough elastoplastic contact models taking as base the mean and minimum values obtained by the GW elastic model and the mean and minimum normalized surface separation (h/σ) for the connecting rod–slider revolute (CR–S), crankshaft–connecting rod (CS–CR) and block–crankshaft joints in the crank angle intervals $660° - 780°$ and $840° - 960°$, respectively.

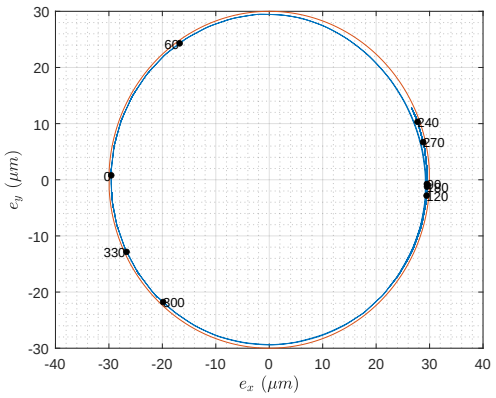

(a) GW

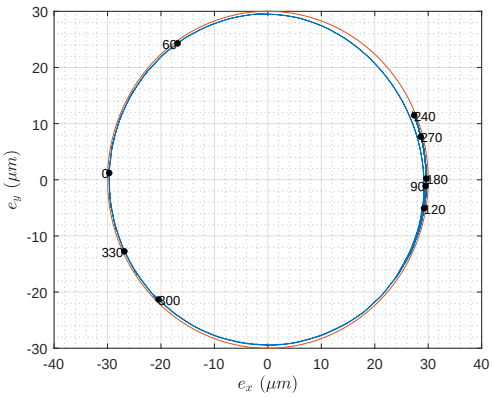

(b) CEB

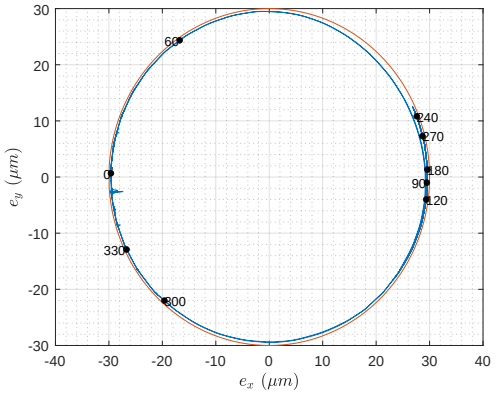

(c) ZMC

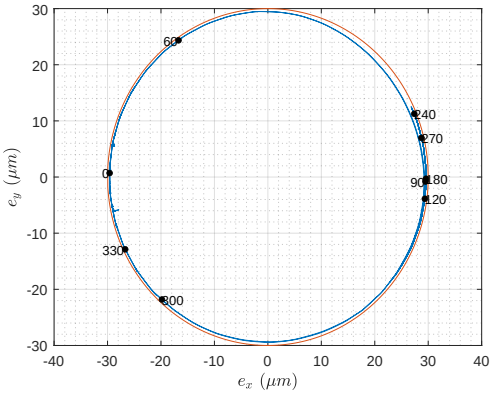

(d) KE

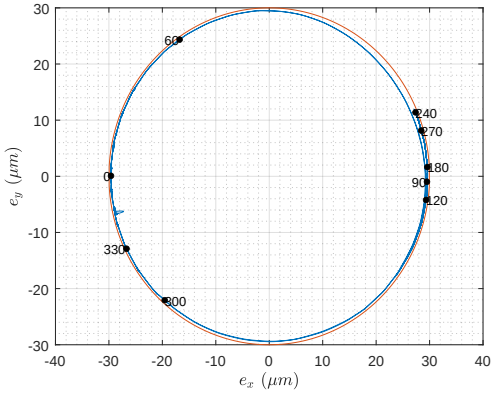

(e) JG

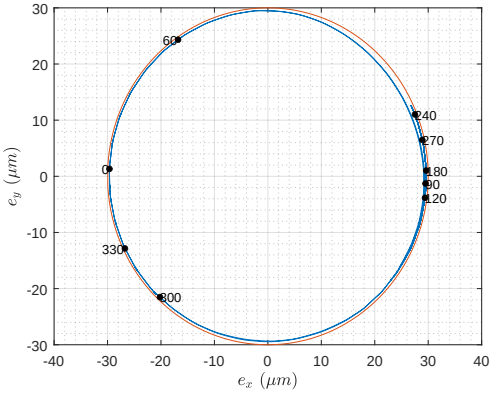

(f) PW

Figure 37 – Journal orbits in the connecting rod–slider revolute joint (CR–S) calculated with the different contact models for the mechanism configuration III.

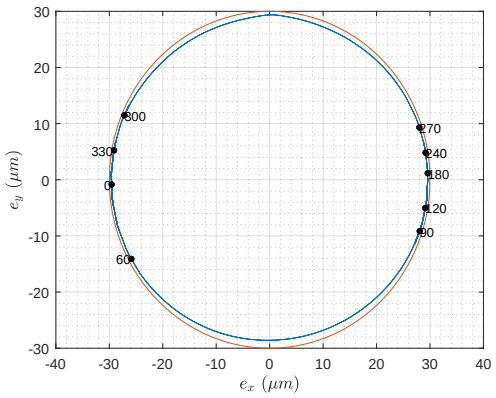

(a) GW

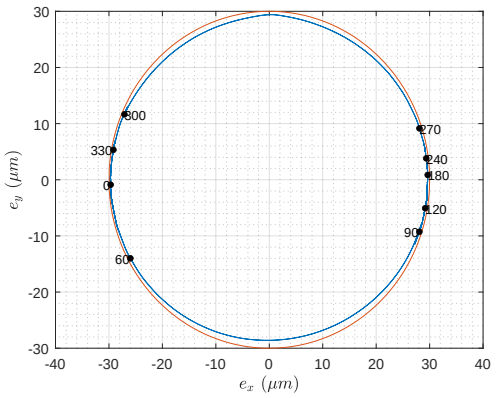

(b) CEB

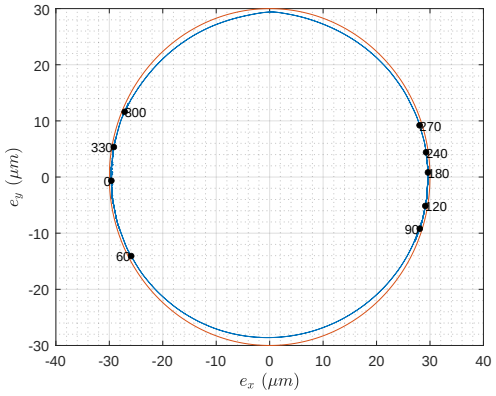

(c) ZMC

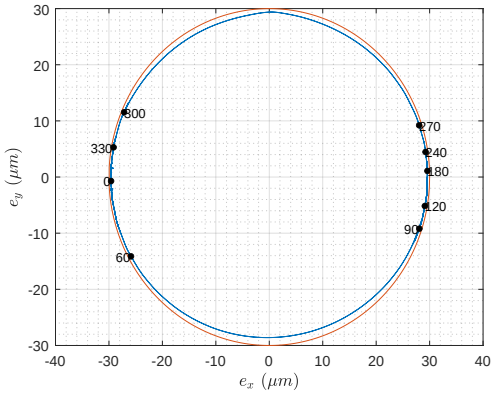

(d) KE

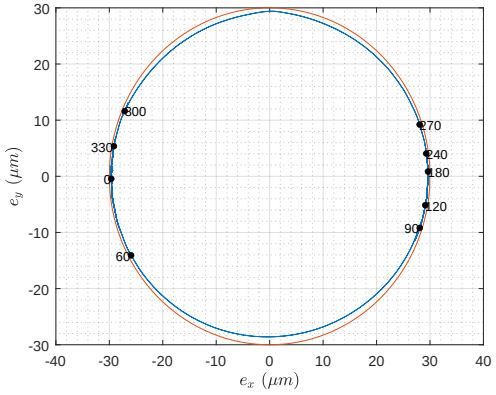

(e) JG

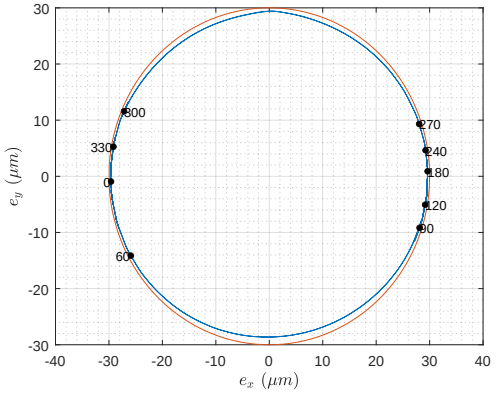

(f) PW

Figure 38 – Journal orbits in the crankshaft–connecting rod revolute joint (CS–CR) calculated with the different contact models for the mechanism configuration III.

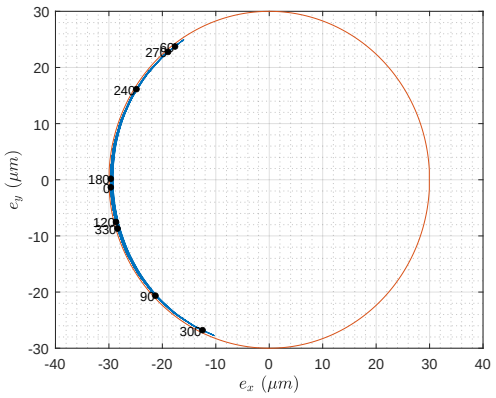

(a) GW

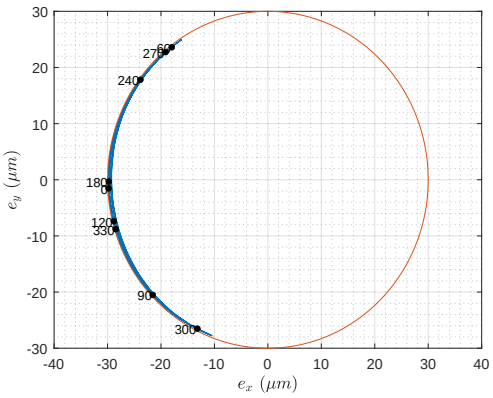

(b) CEB

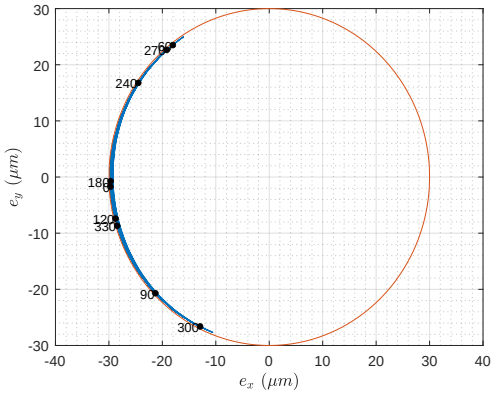

(c) ZMC

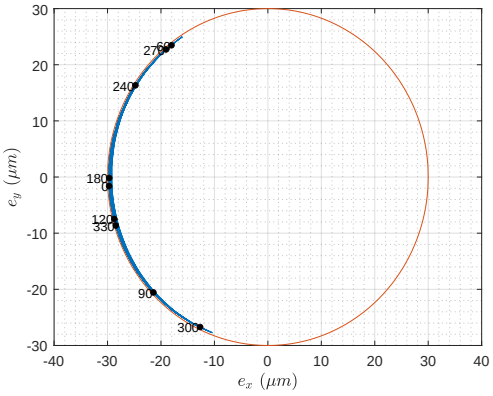

(d) KE

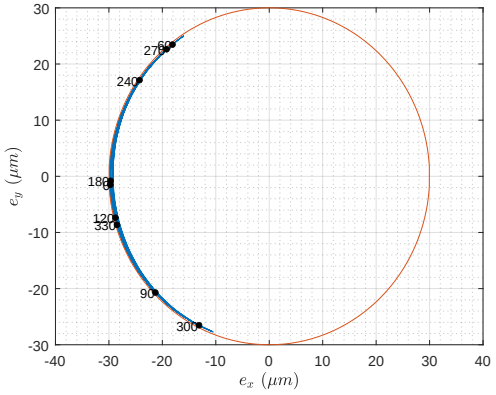

(e) JG

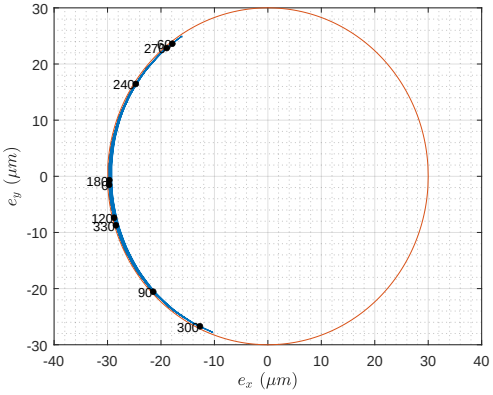

(f) PW

Figure 39 – Journal orbits in the block–crankshaft revolute joint (B–CS) calculated with the different contact models for the mechanism configuration III.

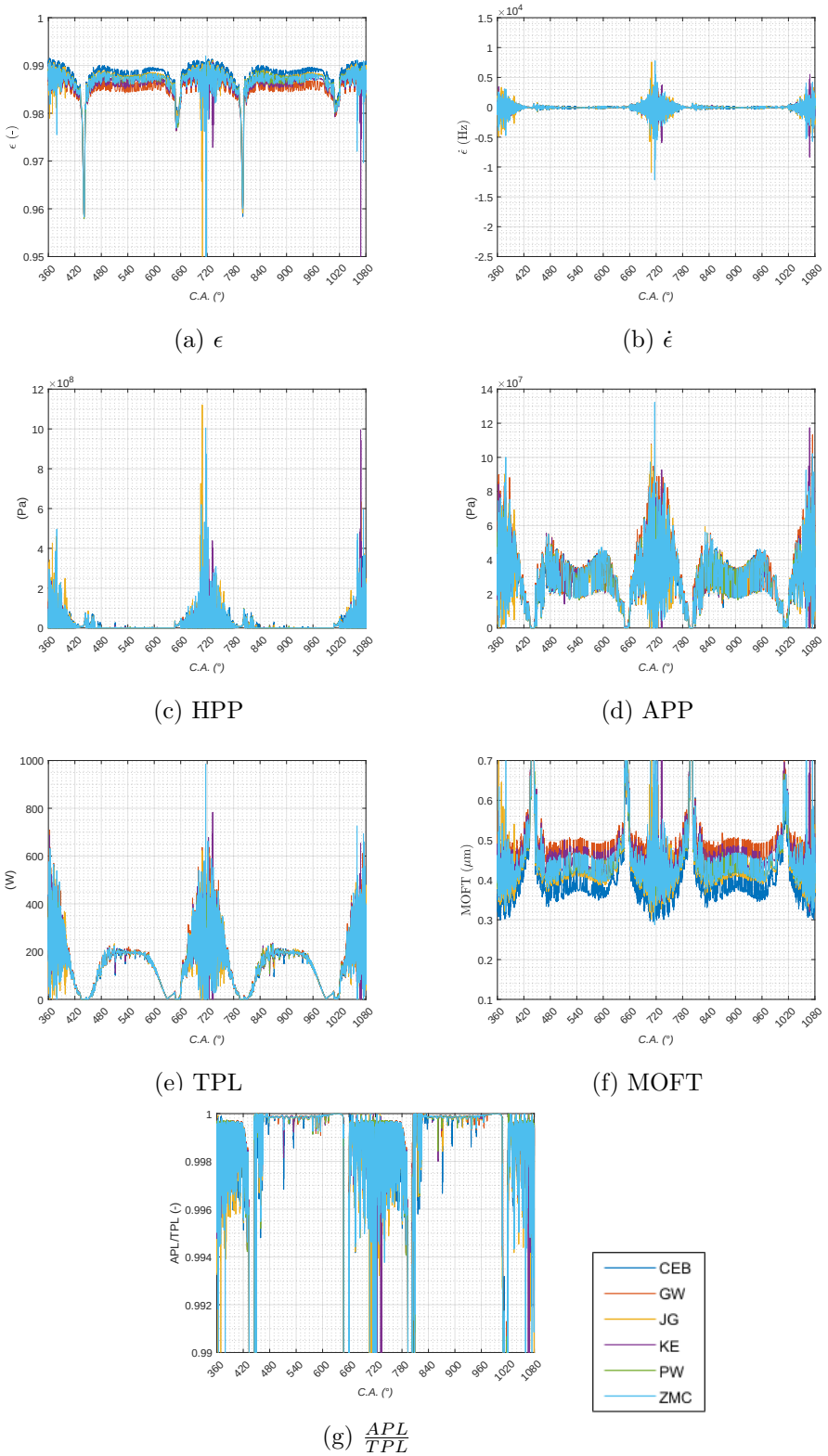

Figure 40 – Lubrication performance of the connecting rod–slider revolute joint (CR–S) for the mechanism configuration III. (a) Eccentricity ratio, (b) Eccentricity ratio velocity, (c) hydrodynamic peak pressure (HPP), (d) asperity contact peak pressure, (e) total power loss (TPL), (f) minimum oil film thickness (MOFT), and (g) asperity-to-total power loss ratio.

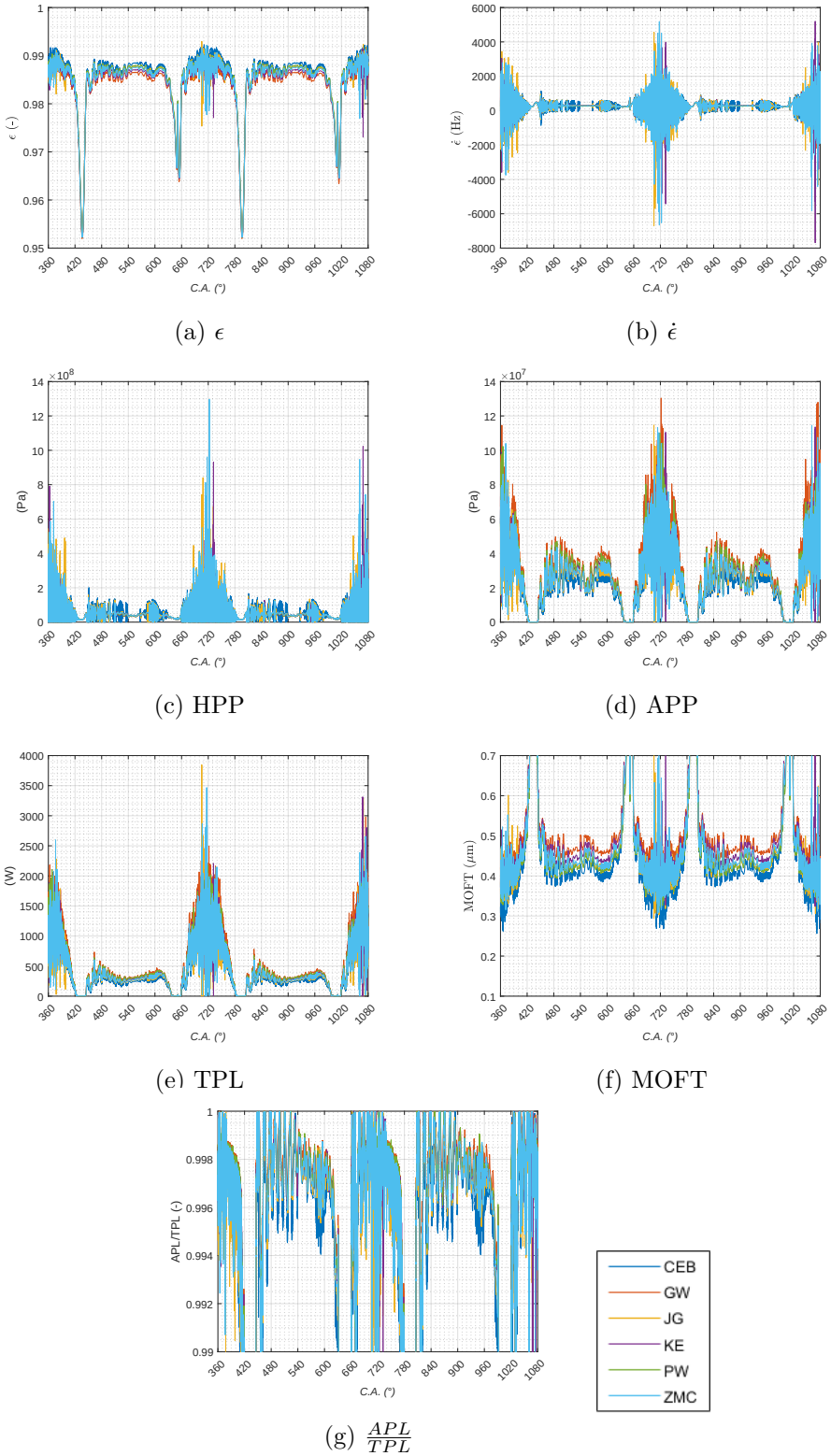

Figure 41 – Lubrication performance of the crankshaft–connecting rod revolute joint (CS–CR) for the mechanism configuration III. (a) Eccentricity ratio, (b) Eccentricity ratio velocity, (c) hydrodynamic peak pressure (HPP), (d) asperity contact peak pressure, (e) total power loss (TPL), (f) minimum oil film thickness (MOFT), and (g) asperity-to-total power loss ratio.

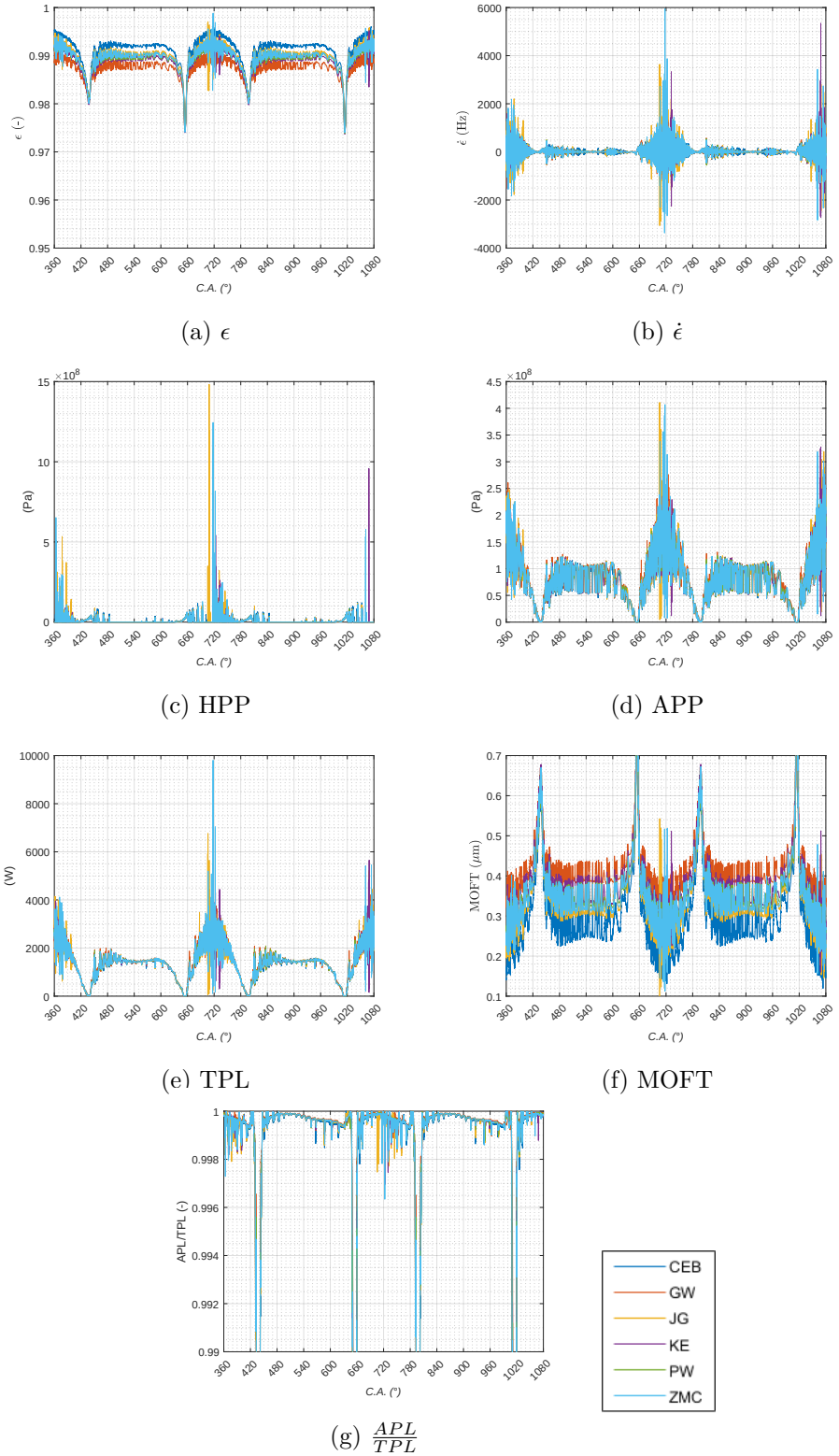

Figure 42 – Lubrication performance of the block–crankshaft revolute joint (B–CS) for the mechanism configuration III. (a) Eccentricity ratio, (b) Eccentricity ratio velocity, (c) hydrodynamic peak pressure (HPP), (d) asperity contact peak pressure, (e) total power loss (TPL), (f) minimum oil film thickness (MOFT), and (g) asperity-to-total power loss ratio.

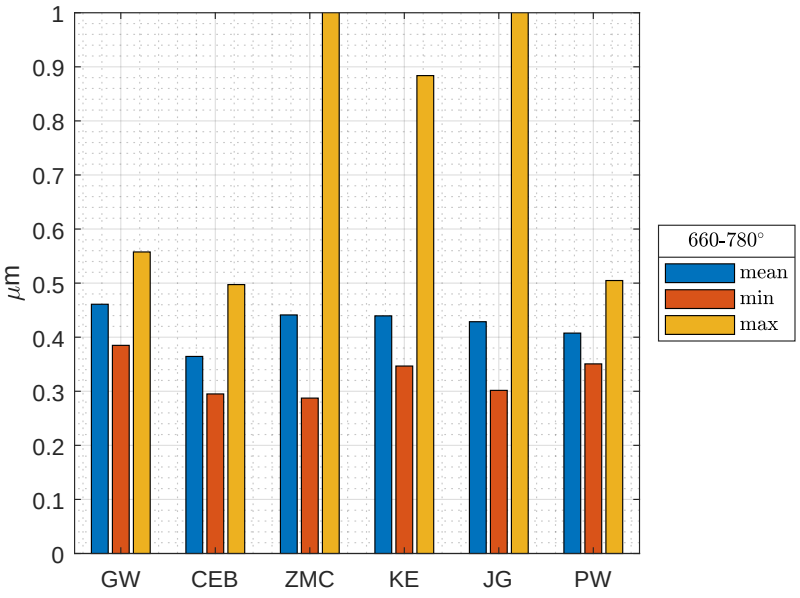

(a) $660 - 780°$

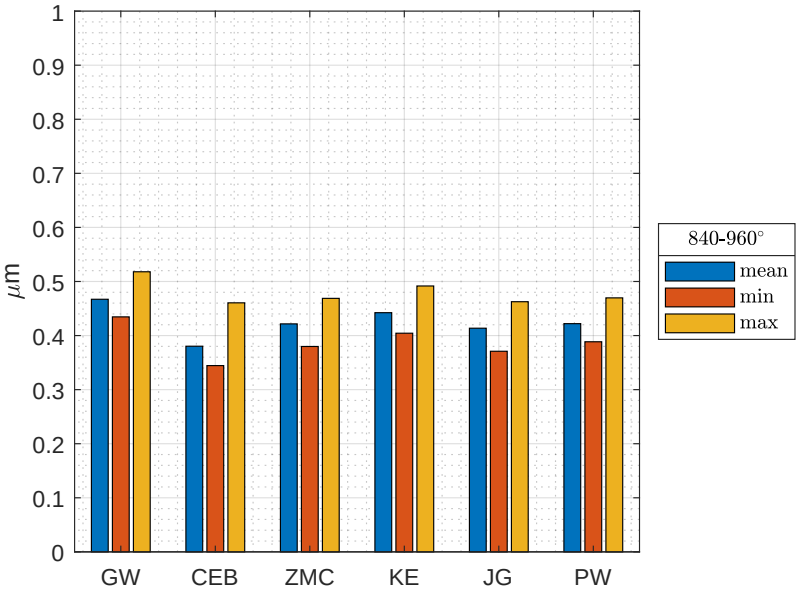

(b) $840 - 960°$

Figure 43 – Mean, minimum and maximum MOFT values in the connecting rod–slider revolute joint (CR–S) in the crank angle intervals $660 - 780°$ and $840 - 960°$ for the mechanism configuration III.

Table 12 – Mean, minimum, maximum and standard deviation of MOFT values in the connecting rod–slider revolute joint (CR–S) in the crank angle intervals $660 - 780°$ and $840 - 960°$ for the mechanism configuration III (values in micrometers).

	Mean	Min	Max	STD
$660 - 780°$				
GW	0.461	0.385	0.558	0.024
CEB	0.364	0.295	0.497	0.034
ZMC	0.441	0.287	2.577	0.150
KE	0.439	0.347	0.884	0.043
JG	0.429	0.302	2.050	0.111
PW	0.408	0.351	0.505	0.027
$840 - 960°$				
GW	0.467	0.435	0.518	0.012
CEB	0.380	0.344	0.461	0.020
ZMC	0.422	0.380	0.469	0.017
KE	0.442	0.404	0.492	0.015
JG	0.414	0.371	0.463	0.016
PW	0.422	0.389	0.470	0.015

Table 13 – Mean, minimum, maximum and standard deviation of MOFT values in the crankshaft–connecting rod revolute joint (CS–CR) in the crank angle intervals $660 - 780°$ and $840 - 960°$ for the mechanism configuration III (values in micrometers).

	Mean	Min	Max	STD
$660 - 780°$				
GW	0.459	0.369	0.566	0.035
CEB	0.381	0.268	0.532	0.054
ZMC	0.429	0.306	0.740	0.043
KE	0.439	0.327	0.702	0.040
JG	0.424	0.294	0.821	0.044
PW	0.410	0.321	0.529	0.040
$840 - 960°$				
GW	0.469	0.439	0.508	0.014
CEB	0.408	0.372	0.446	0.014
ZMC	0.436	0.405	0.480	0.015
KE	0.450	0.412	0.492	0.016
JG	0.430	0.398	0.470	0.015
PW	0.425	0.393	0.468	0.015

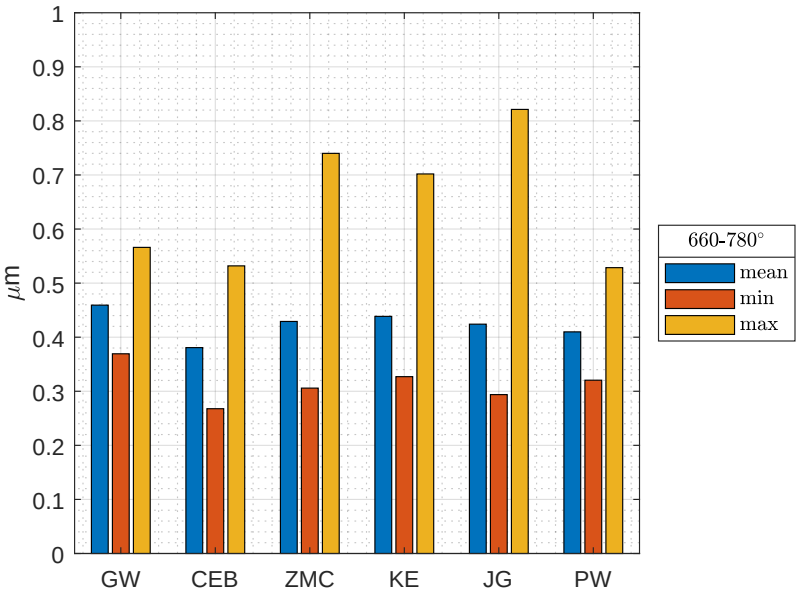

(a) $660 - 780°$

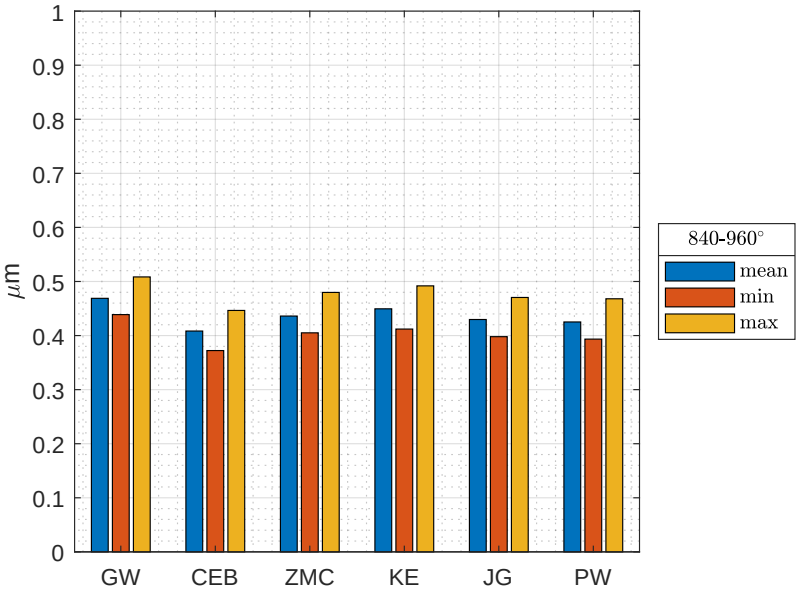

(b) $840 - 960°$

Figure 44 – Mean, minimum and maximum MOFT values in the crankshaft–connecting rod revolute joint (CS–CR) in the angle intervals $660 - 780°$ and $840 - 960°$ for the mechanism configuration III.

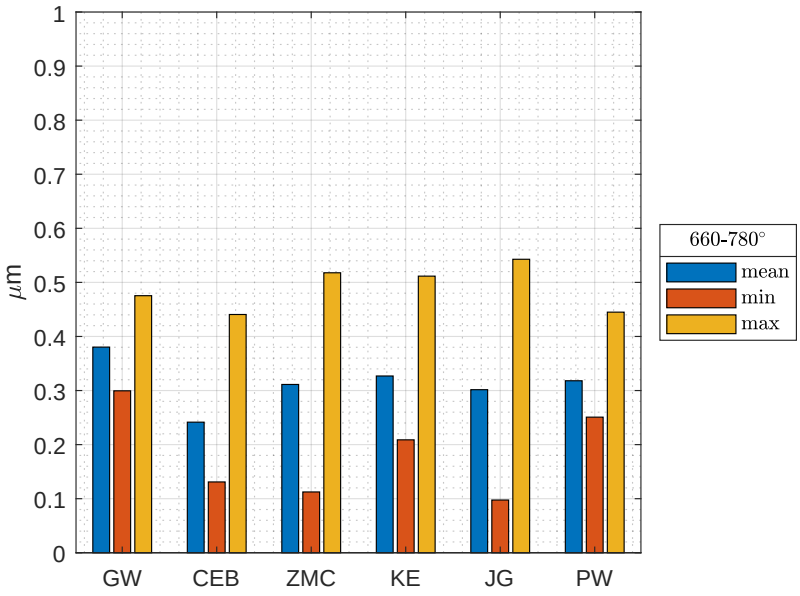

(a) $660 - 780°$

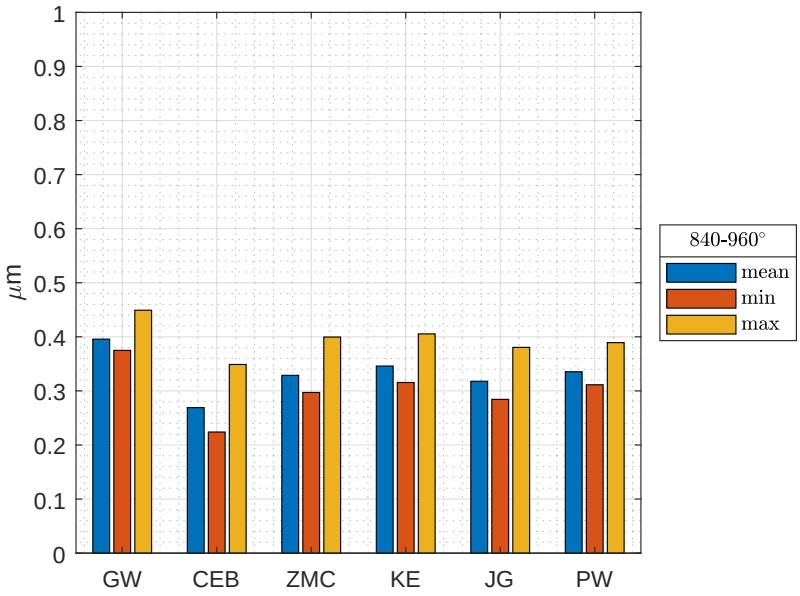

(b) $840 - 960°$

Figure 45 – Mean, minimum and maximum values of MOFT in the angle intervals $660 - 780°$ and $840 - 960°$ to the B-CS joint in configuration III.

Table 14 – Mean, minimum, maximum and standard deviation of MOFT values in the block–crankshaft revolute joint (B–CS) in the crank angle intervals $660 - 780°$ and $840 - 960°$ for the mechanism configuration III (values in micrometers).

	Mean	Min	Max	STD
$660 - 780°$				
GW	0.380	0.299	0.475	0.034
CEB	0.242	0.131	0.441	0.057
ZMC	0.311	0.112	0.518	0.049
KE	0.327	0.209	0.512	0.049
JG	0.302	0.098	0.543	0.051
PW	0.318	0.251	0.445	0.040
$840 - 960°$				
GW	0.400	0.375	0.449	0.013
CEB	0.269	0.224	0.349	0.025
ZMC	0.329	0.297	0.400	0.019
KE	0.346	0.316	0.405	0.019
JG	0.318	0.284	0.381	0.019
PW	0.335	0.311	0.389	0.016

The results presented in figure 48 corroborate the results presented in figure 42 to the B-CS revolute joint that presented high asperity pressure peaks and higher power losses than the other two clearance joints. The mean and minimum values of the normalized surface approximation were between 1.5 and 2.5 and 0.5 to 2.5, respectively, in the crank angle interval $660° - 780°$ for the elastoplastic contact models, indicating a high contact between surfaces. The CEB, ZMC and JG models presented surface separation values < 1.0. For the crank angle interval $840° - 960°$, surface separation values were slightly closer and higher, varying between 1.0 and 3.0. It is possible to verify that in the first crank angle interval there was a high percentage variation of the mean MOFT parameter to all elastoplastic models compared to the GW model, notably the CEB, ZMC and JG elastoplastic models, whose results reach more than - 50% of variation on the MOFT considering the results in the crank angle interval $660° - 780°$.

4.3.2 Dynamic Response

Figure 49 presents the linear and angular positions, velocities and accelerations of the slider and connecting rod to each contact model in configuration 3RJ.

In this configuration, it is possible to observe a wide variation in the acceleration of the connecting rod and slider in the crankshaft angle intervals $360 - 420°$, $660 - 780°$ and $1020 - 1080°$. The angular and linear acceleration of connecting rod and slider, respectively, reach the minimum and maximum peak values of -1.0 10^6 rad/s^2 to above 1.5 10^6 rad/s^2 for connecting rod and below -0.35 10^6 m/s^2 immediately before the angle of 720°. Comparing with the results in configuration II, there was an increase in the acceleration response of

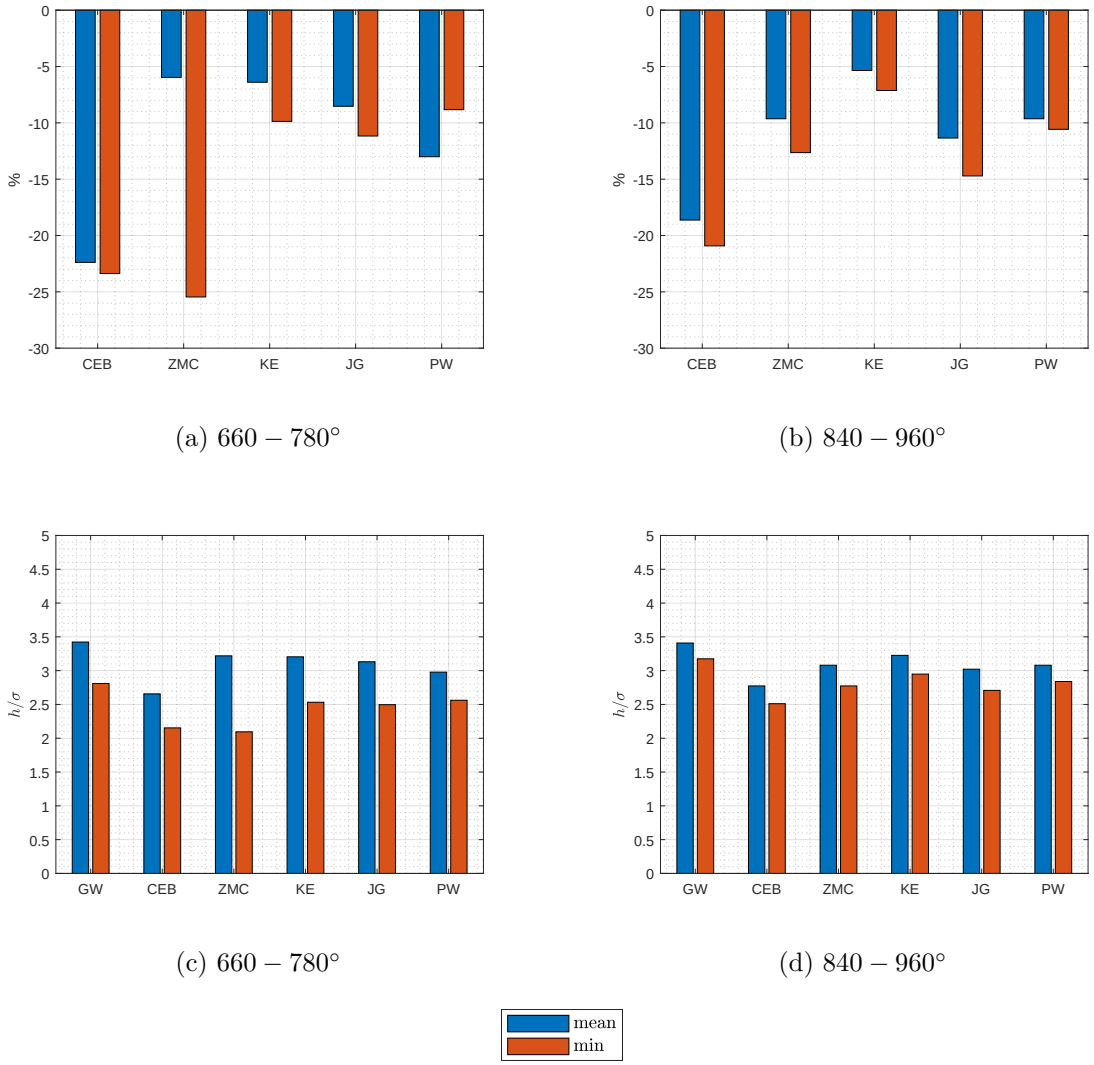

(a) $660 - 780°$

(b) $840 - 960°$

(c) $660 - 780°$

(d) $840 - 960°$

Figure 46 – MOFT percentage variation of the elastoplastic rough contact models and surface approximation (h'/σ) values in the connecting rod–slider revolute joint (CR–S) in the crank angle intervals $660° - 780°$ and $840° - 960°$ for the mechanism configuration III.

the system and the amplitude of variation in these intervals, but it was still smaller than in the configuration I. In this case there was an increase of the variation in the values inside the crankshaft angle intervals of $420 - 660°$ and $780 - 1020°$.

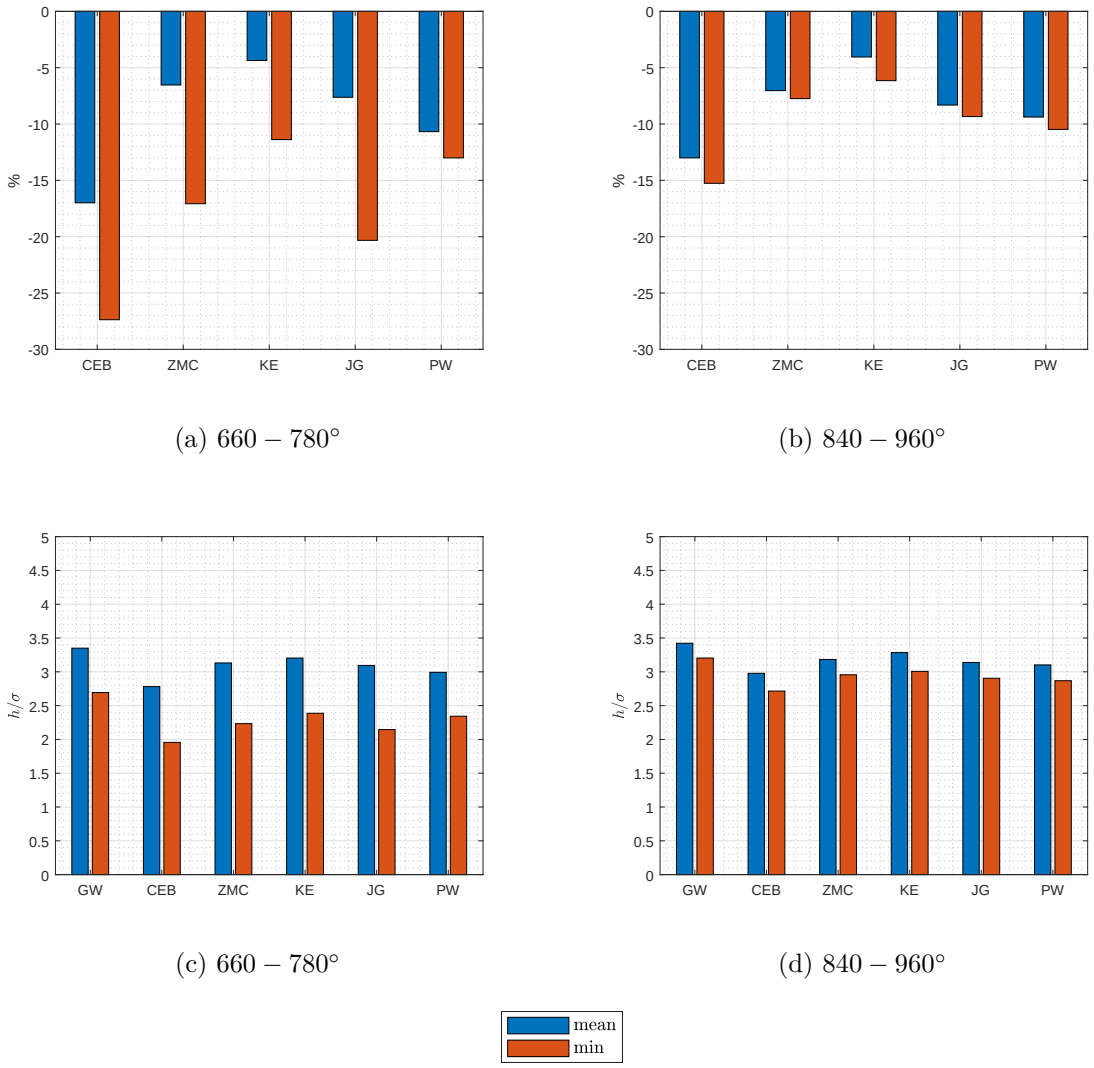

(a) $660 - 780°$

(b) $840 - 960°$

(c) $660 - 780°$

(d) $840 - 960°$

Figure 47 – MOFT percentage variation of the elastoplastic rough contact models and surface approximation (h'/σ) values in the crankshaft–connecting rod revolute joint (CS–CR) in the crank angle intervals $660° - 780°$ and $840° - 960°$ for the mechanism configuration III.

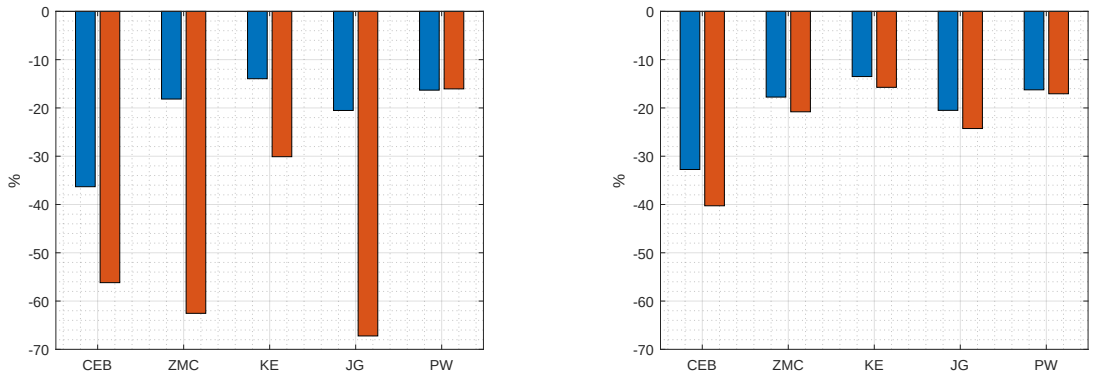

(a) $660 - 780°$

(b) $840 - 960°$

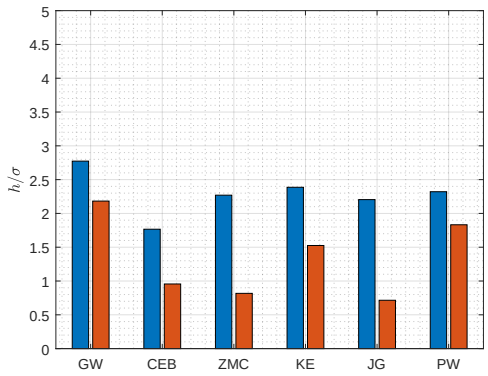

(c) $660 - 780°$

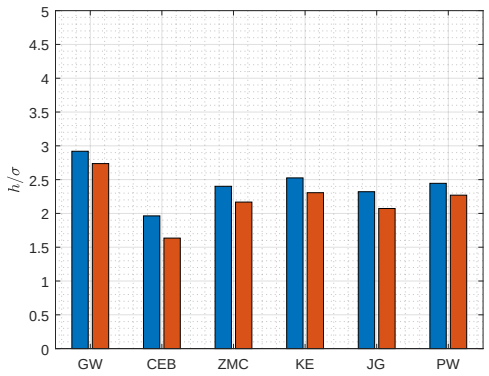

(d) $840 - 960°$

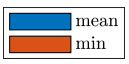

Figure 48 – MOFT percentage variation of the elastoplastic rough contact models and surface approximation (h'/σ) values in the block–crankshaft revolute joint (B–CS) in the crank angle intervals $660° - 780°$ and $840° - 960°$ for the mechanism configuration III.

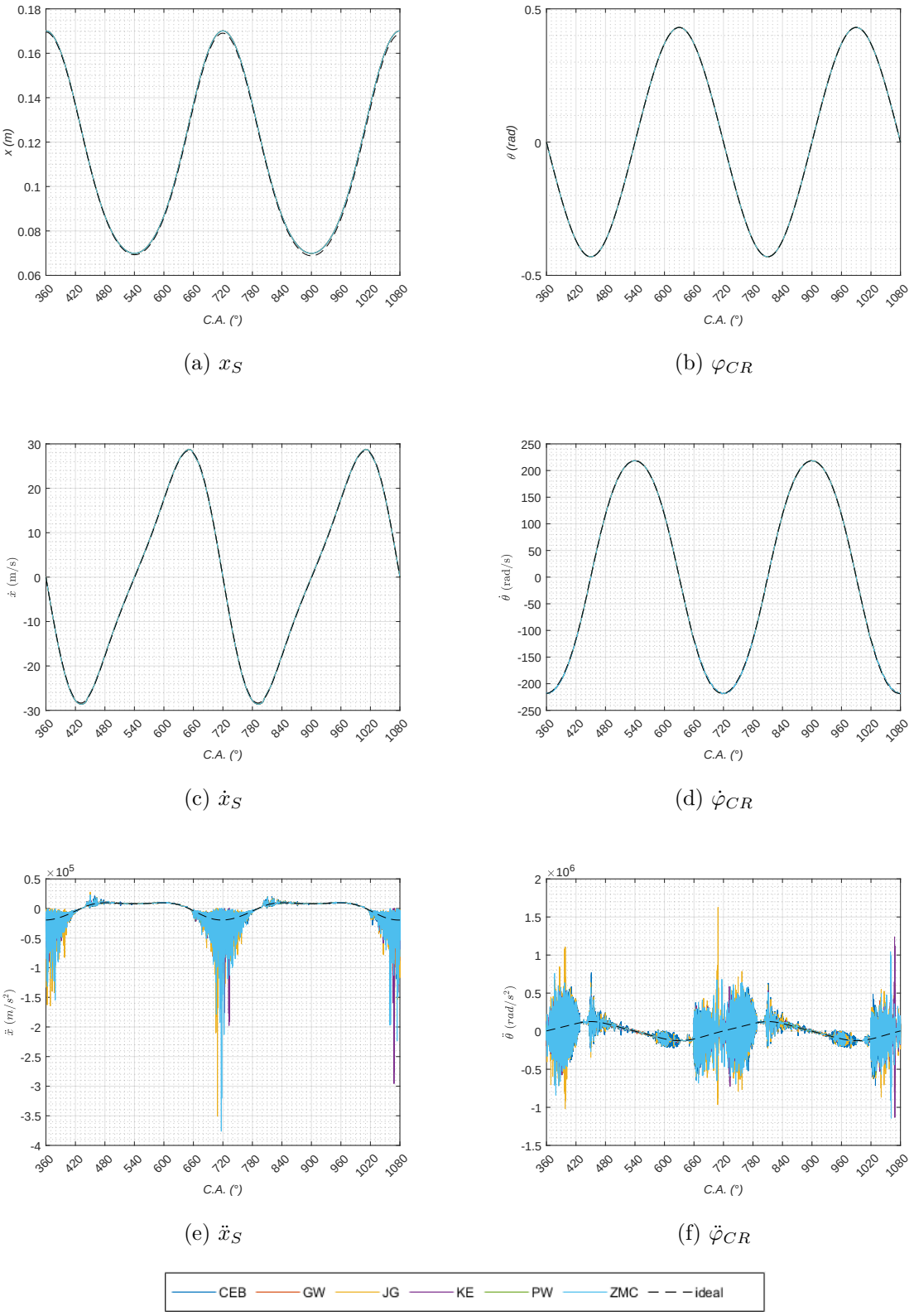

(a) x_S (b) φ_{CR}

(c) $\dot{x}_S$ (d) $\dot{\varphi}_{CR}$

(e) $\ddot{x}_S$ (f) $\ddot{\varphi}_{CR}$

Figure 49 – Linear and angular positions, velocities and accelerations of the slider and connecting rod for the configuration III.

5 Conclusions

This work evaluated the tribodynamic behavior of a crank-slider mechanism with lubricated revolute clearance joints operating under mixed lubrication conditions for three joint configurations. A multibody tribodynamics modeling methodology that couples the tribological phenomena in lubricated clearance joints with the dynamic model of multibody systems using the multibody dynamics formalism was implemented in the research computational code LUBST. The lubrication behavior of the revolute joints was evaluated using a Reynolds-based mixed lubrication model with mass-conserving cavitation and various elastic and elastoplastic rough contact models. The influence of the different rough contact models on the lubrication performance of the system was assessed for each joint configuration. Furthermore, a Multibody Dynamics Simulation Toolbox (MDST), including a graphical user interface (GUI), was also developed and coupled to the LUBST framework. This intends to enable non-developers and/or non-academic users to interact with the MDST and LUBST tools and potentially extend them in future research.

In addition to the Greenwood–Williamson (GW) and Greenwood–Tripp (GT) elastic rough contact models that had already been implemented in LUBST, the following new elastoplastic rough contact models were implemented in this work: Chang, Etsion and Bogy model (CEB), Zhao, Maietta and Chang model (ZMC), Kogut and Etsion model (KE), Jackson and Green model (JG), and Pullen and Williamson model (PW). The lubrication performance of the revolute joints and the dynamic response of the connecting rod and slider components for three joint configurations varying from one to three clearance joints in the system were analyzed.

The simulation results predicted with the elastoplastic rough contact models (CEB, ZMC, KE, JG and PW) differed significantly from those obtained with standard elastic rough contact models (GW and GT) used in most published studies and commercial multibody dynamics software. These differences were more evident when the contact was heavy, as in the configuration considering the three revolute joints with clearance. Particularly for this mechanism configuration, the block–crankshaft joint (B–CS) had very high peak pressures and power losses compared with the other two configurations. This condition was highlighted when verifying that the low values of the normalized surface approximation for some elastoplastic models were less than 1.5 and the significant difference in the percentage variation of MOFT in the elastoplastic contact models compared to the values obtained using the GW elastic model. It was noted that considering a second joint with clearance, as in the case of configuration II compared to configuration I, provided a damping effect, improving the clearance joint performance parameters, whose values could be seen in the graphical results. Furthermore, the results presented a wide variation in

values of the parameters in the 60◦ before and after the transition between cycles.

The rough contact models evaluated in this work have different assumptions and results for the contact of journal bearing surfaces compared with the contact-impact models often used in multibody dynamics analyzes. A continuous contact-impact model for smooth surfaces often leads to higher penetration in the contact zone, which may indicate an unrealistic component failure. However, a rough contact model avoids this overestimated prediction problem by considering the surface roughness characteristics in the contact model. The journal orbits calculated in this work with the rough contact models show that the surface interactions mostly occurred inside the clearance circle because the contact was more realistically assumed to occur at the asperities of the rough surfaces. This differs from the smooth surface-based contact-impact models, where the contact often occurs outside the clearance circle due to the often overvalued higher penetrations predicted with such models. It is also noteworthy that the rough contact models are highly nonlinear, so the simulation time steps should be carefully controlled to prevent convergence issues during contact events.

When only the connecting rod–slider joint was assumed with clearance (joint configuration I), the lubrication performance parameters of the joint were similar among the rough contact models evaluated. However, significant differences between the elastic and elastoplastic contact models were realized for the other joint configurations, especially in the minimum oil film thickness, hydrodynamic and asperity contact peak pressures, and power losses.

It was possible to observe that the CEB contact model usually provided lower results, mainly for the MOFT, an essential bearing performance parameter. Then, it could indicate that using such a model would be interesting in more conservative analyses. The elastic GW contact model presented higher MOFT values for all revolute joints in the three configurations. Overall, due to the robustness of the mathematical formulations and physical mechanisms considered, it is suggested the use of the KE or JG models when more detailed analyses are desired, especially those involving wear and failure effects.

Overall, the simulation results for the mechanism and joint configurations analyzed in this work indicate that the greater the severity of the lubrication conditions in the joints, the greater the differences between the elastic and elastoplastic rough contact models evaluated. This is likely due to the increasing predominance of the elastoplastic deformation of the surface asperities at a higher contact intensity. The rough elastic contact models ignore the elastoplastic deformation of the asperities, giving higher values for the contact pressures and forces than the elastoplastic models. Therefore, the elastoplastic contact models could provide more consistent results for the mechanism and joint configurations analyzed in this work since the joints operated predominantly in the mixed lubrication regime due to the high load conditions and low-viscosity oil used.

5.1 Future Works

Some possible directions for future work on the topics approached in this contribution are outlined below.

- Incorporate the secondary piston motion and the loads acting on the piston head into the proposed multibody dynamics model of the crank–connecting rod–piston mechanism;
- Explore the use of surface textures to enhance performance and investigate the effects of low-viscosity oil rheology on joint behavior;
- Include additional factors that influence the tribological performance of joints, such as temperature and the wear-induced changes in surface geometry and asperity distribution and morphology;
- Validate the proposed modeling framework with experimental data and compare it with other methods for simulating multibody dynamics with rough contact surfaces and wear;
- Extend the proposed modeling framework to include the flexibility of the connected bodies (*flexible* multibody dynamics model);
- Extend the proposed modeling framework to three-dimensional problems and spatial contact situations, which require more complex geometric and kinematic descriptions of the contacting surfaces and bodies;
- Continue the development of the graphical user interface of the Multibody Dynamic Simulation Toolbox (MDST) coupled to the LUBST code.

Bibliography

ALLMAIER, H.; OFFNER, G. Current challenges and frontiers for the ehd simulation of journal bearings: a review. *SAE Technical Paper Series*, SAE International, p. 13, 2016. ISSN 0148-7191.

BAUMGARTE, J. Stabilization of constraints and integrals of motion in dynamical systems. *Computer Methods in Applied Dynamics and Engineering*, Elsevier, v. 1, p. 1–16, 1972.

BEHESHTI; KHONSARI. Asperity micro-contact models as applied to the deformation of rough line contact. *Tribology International*, Elsevier, v. 52, p. 61–74, 2012. Disponível em: <https://doi.org/10.1016/j.triboint.2012.02.026>.

CAMPBELL, J. et al. Bearings for reciprocating machinery: A review of the present state of theoretical, experimental and service knowledge. *Sage*, Institution of Mechanical Engineers, v. 182, n. 1, p. 51–74, 1967. Disponível em: <https://doi.org/10.1243/PIME_CONF_1967_182_008_02>.

CHANG, W.-R.; ETSION, I.; BOGY, D. An elastic-plastic model for the contact of rough surfaces. *Journal of Tribology*, ASME, v. 109, n. 2, p. 257–263, 1987. Disponível em: <https://doi.org/10.1115/1.3261348>.

DUBOWSKY, S.; FREUDENSTEIN, F. Dynamic analysis of mechanical systems with clearances - part 1 formation of dynamic model. *Manufacturing Science and Engineering*, ASME, v. 93, n. 1, p. 305–309, 1971.

DUBOWSKY, S.; FREUDENSTEIN, F. Dynamic analysis of mechanical systems with clearances - part 2 dynamic response. *Manufacturing Science and Engineering*, ASME, v. 93, n. 1, p. 310–316, 1971.

DUBOWSKY, S.; MOENING, M. F. An experimental and analytical study of impact forces in elastic mechanical systems with clearances. *Mechanism and Machine Theory*, Elsevier, v. 13, n. 4, p. 451–465, 1978. Disponível em: <https://doi.org/10.1016/0094-114X(78)90018-6>.

FANG, C. et al. Modeling a lubricated full-floating pin bearing in planar multibody systems. *Tribology International*, Elsevier, v. 131, n. 1, p. 22–37, 2019. Disponível em: <https://doi.org/10.1016/j.triboint.2018.10.045>.

FANG, C. et al. On the tribo-dynamic interactions between piston skirt-liner system and pin assembly in a gasoline engine. *Mechanism and Machine Theory*, Elsevier, v. 166, n. 1, p. 1–26, 2021. Disponível em: <https://doi.org/10.1016/j.mechmachtheory.2021.104497>.

FISCHER-CRIPPS, A. *Introduction to Contact Mechanics*. 2. ed. [S.l.]: Springer, 2007.

FLORES, P. Kinematics and dynamics of multibody systems with imperfect joints. In: _____. *Lecture Notes in Applied and Computational Mechanics*. Springer, 2008. v. 34, p. 169. Disponível em: <https://doi.org/10.1007/978-3-540-74361-3>.

FLORES, P.; AMBROSIO, J. On the contact detection for contact-impact analysis in multibody systems. *Multibody System Dynamics*, Elsevier, v. 24, p. 106–122, 2010. Disponível em: <https://doi.org/10.1007/s11044-010-9209-8>.

FLORES, P. et al. A study on dynamics of mechanical systems including joints with clearance and lubrication. *Mechanism and Machine Theory*, Elsevier, v. 41, p. 247–261, 2006. Disponível em: <https://doi.org/10.1016/j.mechmachtheory.2005.10.002>.

FLORES, P. et al. Dynamic behaviour of planar rigid multi-body systems including revolute joints with clearance. *Mechanism and Machine Theory*, Elsevier, v. 221, n. 2, p. 161–174, 2007. Disponível em: <https://doi.org/10.1243/14644193JMBD96>.

FLORES, P.; AMBRÓSIO, J.; CLARO, J. P. Dynamic analysis for planar multibody mechanical systems wit lubricated joints. *Multibody System Dynamics*, Kluwer Academic Publishers, v. 12, n. 1, p. 47–74, 2004. Disponível em: <https://doi.org/10.1023/B:MUBO.0000042901.74498.3a>.

FRENê, J. et al. Hydrodynamic lubrication: Bearings and thrust bearings. In: _____. *Tribology Series*. Elsevier, 1997. v. 33, p. 490. Disponível em: <https://www.sciencedirect.com/bookseries/tribology-series/vol/33/suppl/C>.

GHAEDNIA, H. et al. A review of elastic-plastic contact mechanics. *Applied Mechanics Reviews*, ASME, v. 69, n. 6, p. 30, 2017. Disponível em: <https://doi.org/10.1115/1.4038187>.

GREENWOOD, J.; WILLIAMSON, J. Contact of nominally flat surfaces. *Mathematical and Physical Sciences*, Proceedings of the Royal Society of London. Series A, v. 295, n. 1442, p. 300–319, 1966. Disponível em: <https://www.jstor.org/stable/2415421>.

HAINES, R. An experimental investigation into the dynamic behaviour of revolute joints with varying degrees of clearance. *Mechanism and Machine Theory*, Elsevier, v. 20, n. 3, p. 221–231, 1985. Disponível em: <https://doi.org/10.1016/0094-114X(85)90009-6>.

HAMROCK, B. J.; SCHMID, S. R.; JACOBSON, B. O. *Fundamentals of Fluid Film Lubrication*. 2. ed. [S.l.]: Marcel Dekker Inc, 2004.

INSIGHT, I. *Moving to even lower viscosities: the latest on north american engine oil viscosity grade trends*. Infineum International Limited, 2020. Disponível em: <https://www.infineuminsight.com/en-gb/articles/moving-to-even-lower-viscosities/>. Acesso em: 10/01/2023.

JACKSON, R. L.; GREEN, I. A statistical model of elasto-plastic asperity contact between rough surfaces. *Tribology International*, Elsevier, v. 39, n. 9, p. 906–914, 2006. Disponível em: <https://doi.org/10.1016/j.triboint.2005.09.001>.

JOHNSON, K. *Contact Mechanics*. 1. ed. [S.l.]: Cambridge University Press, 1985.

KOGUT, L.; ETSION, I. A finite element based elastic-plastic model for the contact of rough surfaces. *Tribology Transactions*, Taylor Francis, v. 46, n. 3, p. 383–390, 2003. Disponível em: <https://doi.org/10.1080/10402000308982641>.

KOSHY, C.; FLORES, P.; LANKARANI, H. Study of the effect of contact force model on the dynamic response of mechanical systems with dry clearance joints: computational and experimental approaches. *Nonlinear Dynamics*, Springer, v. 73, p. 325–338, 2013. Disponível em: <https://doi.org/10.1007/s11071-013-0787-x>.

LANKARANI, H.; NIKRAVESH, P. A contact force model with hysteresis damping for impact analysis of multibody systems. *Mechanical Design*, ASME, v. 112, n. 3, p. 369–376, 1985. Disponível em: <https://doi.org/10.1115/1.2912617>.

LIU, G.; WANG, Q. J.; LIN, C. A survey of current models for simulating the contact between rough surfaces. *Tribology Transactions*, Taylor Francis, v. 42, n. 3, p. 581–591, 1999.

LU, Y. et al. The analysis of secondary motion and lubrication performance of piston considering the piston skirt profile. *Shock and Vibration*, Hindawi, p. 1–27, 2018. Disponível em: <https://doi.org/10.1155/2018/3240469>.

MEDEIROS, J. T. N. de. *Fadiga de contato de discos metálicos não-conformes submetidos a ensaio a seco de rolamento cíclico*. Tese (Doutorado) — Escola Politécnica da Universidade de São Paulo, 2002.

MOKHTAR, M.; HOWARTH, R.; DAVIES, P. The behavior of plain hydrodynamic journal bearings during starting and stopping. *ASLE Translactions*, Taylor Francis, v. 20, n. 3, p. 183–190, 1977. Disponível em: <https://doi.org/10.1080/05698197708982832>.

NIKRAVESH, P. E. *Computer-Aided Analysis of Mechanical Systems*. [S.l.]: Prentice Hall, 1988.

NIKRAVESH, P. E. *Planar Multibody Dynamics: formulation, programming and applications*. [S.l.]: Prentice Hall, 2007.

NORTON, R. *Machine Design*. 1. ed. [S.l.]: Prentice-Hall, 1996.

PERSSON, B. Contact mechanics for randomly rough surfaces. *Surface Science Reports*, Elsevier, v. 61, n. 4, p. 201–227, 2006. Disponível em: <https://doi.org/10.1016/j.surfrep.2006.04.001>.

PROFITO, F. J. *On the development of advanced techniques for mixed-elastohydrodynamic lubrification modelling of journal and sliding bearing systems*. Tese (Doutorado) — Escola Politécnica da Universidade de São Paulo, 2015. Disponível em: <http://www.teses.usp.br/teses/disponiveis/3/3152/tde-07072016-151613/pt-br.php>.

PULLEN, J.; WILLIAMSON, J. On the plastic contact of rough surfaces. *Mathematical and Physical Sciences*, Proceedings of the Royal Society of London. Series A, v. 327, n. 1569, p. 159–173, 1972. Disponível em: <https://www.jstor.org/stable/78125>.

RAVN. A continuous analysis method for planar multibody systems with joint clearance. *Multibody System Dynamics*, Kluwer Academic Publishers, v. 2, n. 1, p. 1–24, 1998. Disponível em: <https://link.springer.com/article/10.1023/A:1009759826529>.

RHEE, J.; AKAY, A. Dynamic response of a revolute joint with clearance. *Mechanism and Machine Theory*, Elsevier, v. 31, n. 1, p. 121–134, 1996. Disponível em: <https://doi.org/10.1016/0094-114X(95)00061-3>.

ROGERS, R.; ANDREWS, G. Dynamic simulation of planar mechanical systems with lubricated bearing clearances using vector-network methods. *Journal of Engineering for Industry*, ASME, v. 99, n. 1, p. 131–137, 1977. Disponível em: <https://doi.org/10.1115/1.3439126>.

SANDER, D. E.; ALLMAIER, H.; PRIEBSCH, H.-H. Friction and wear in automotive journal bearings operating in today's severe conditions. In: _____. *Advances in Tribology*. [S.l.]: InTechOpen, 2006. cap. 7, p. 142–174.

SHABANA, A. A. *Dynamics of Multibody Systems*. 4. ed. [S.l.]: Cambridge University Press, 2013.

SKVORTSOV, L. Efficient implementation of second-order implicit runge-kutta methods. *Mathematical Models and Computer Simulations*, Pleiades, v. 5, n. 6, p. 565–574, 2013.

SOONG, K.; THOMPSON, B. S. A theoretical and experimental investigation of the dynamic response of a slider-crank mechanism with radial clearance in the gudgeon-pin joint. *Mechanical Design*, ASME, v. 112, n. 2, p. 183–189, 1990. Disponível em: <https://doi.org/10.1115/1.2912591>.

STACKOWIAK, G.; BATCHELOR, A. *Engineering Tribology*. 2. ed. [S.l.]: Butterworth-Heinemann, 2005.

TIAN, Q.; ZHANG, Y.; YANG, J. Simulation of planar flexible multibody systems with clearance and lubricated revolute joints. *Nonlinear Dynamics*, Springer, v. 489, p. 489–511, 2010. Disponível em: <https://doi.org/10.1007/s11071-009-9610-0>.

WANG, X.; LIU, G. Modeling and simulation of revolute joint with clearance in planar multi-body systems. *Mechanical Science and Technology*, Springer, v. 29, p. 4113–4120, 2015. Disponível em: <https://doi.org/10.1007/s12206-015-0905-4>.

ZHAO, B. et al. Modeling and analysis of planar multibody system with mixed lubricated revolute joint. *Tribology International*, Elsevier, v. 98, p. 229–241, 2016. Disponível em: <https://doi.org/10.1016/j.triboint.2016.02.024>.

ZHAO, Y.; MAIETTA, D. M.; CHANG, L. An asperity microcontact model incorporating the transition from elastic deformation to fully plastic flow. *Journal of Tribology*, ASME, v. 122, n. 1, p. 86–93, 2000. Disponível em: <https://doi.org/10.1115/1.555332>.

ZHMUD, B. Motor oil, fuel economy and real driving emissions in the era of e-mobility. In: EUROPEAN BASE OILS & LUBRICANTS INTERACTIVE SUMMIT. Florence, Italy, 2018.

Annex

ANNEX A – Rough Contact Models Equations

A.1 Constants and Integration Terms of Contact Models

This subsection aims to present the terms and integration constants of each of the contact models used in the simulation. These models are implemented in the LUBST platform, used for calculating and returning the hydrodynamic and contact forces acting on joints with clearance. Initially, the terms and constants related to the dimensionless pressure are presented, and finally, the terms and constants related to the calculations of the dimensionless area are presented.

A.1.1 Dimensionless Contact Pressure

- Greenwood and Williamsom Model (GW)

  Constants

$$C_{\Phi_1}^{GW} = \frac{4}{3}\sqrt{\frac{\sigma}{\beta}}$$

$$C_{\Phi_2}^{GW} = 0$$

  Integral Terms

$$\Phi_1^{GW} = \int_{h'}^{\inf} (s - h')^{3/2} \phi(s)\, ds$$

$$\Phi_2^{GW} = 0$$

- Chang, Etsion and Bogy Model (CEB)

  Constants

$$C_{\Phi_1}^{CEB} = \frac{4}{3}\sqrt{\frac{\sigma}{\beta}}$$

$$C_{\Phi_2}^{CEB} = \pi K \frac{H}{E}$$

where $K = 0.454 + 0.41v$, H and E are the hardness of soft material and effective elastic modulus, respectively.

Integral Terms

$$\Phi_1^{CEB} = \int_{h'}^{h'+\delta_{CEB}^*} (s - h')^{3/2} \phi(s) ds$$

$$\Phi_2^{CEB} = \int_{h'+\delta_{CEB}^*}^{\inf} [2(s - h') - \delta_{CEB}^*] \phi(s) ds$$

where $\delta_{CEB}^* = (\frac{\pi KH}{2E})^2 (\frac{\beta}{\sigma})$.

- Zhao, Maietta and Chang Model (ZMC)

Constants

$$C_{\Phi_1}^{ZMC} = \frac{4}{3} \sqrt{\frac{\sigma}{\beta}}$$

$$C_{\Phi_2}^{ZMC} = 2\pi \frac{H}{E}$$

$$C_{\Phi_3}^{ZMC} = \pi \frac{H}{E}$$

Integral Terms

$$\Phi_1^{ZMC} = \int_{h'}^{h'+\delta_{ZMC}^1} (s - h')^{3/2} \phi(s) ds$$

$$\Phi_2^{ZMC} = \int_{h'+\delta_{ZMC}^2}^{\inf} (s - h') \phi(s) ds$$

$$\Phi_3^{ZMC} = \int_{h'+\delta_{ZMC}^1}^{h'+\delta_{ZMC}^2} [1 - (1 - (2K/3)) \frac{\ln \delta_{ZMC}^2 - \ln (s - h')}{\ln \delta_{ZMC}^2 - \ln \delta_{ZMC}^1}]$$
$$[1 - 2(\frac{(s - h') - \delta_{ZMC}^1}{\delta_{ZMC}^2 - \delta_{ZMC}^1})^3 + 3(\frac{(s - h') - \delta_{ZMC}^1}{\delta_{ZMC}^2 - \delta_{ZMC}^1})^2] (s - h') \phi(s) ds$$

where $\delta_{ZMC}^1 = (\frac{3\pi KH}{4E})^2 (\frac{\beta}{\sigma})$ and $\delta_{ZMC}^2 = 54\delta_{ZMC}^1$.

- Kogut and Etsion Model (KE)

  Constants

$$C_{\Phi_1}^{KE} = \frac{4}{3}\sqrt{\frac{\sigma}{\beta}}$$

$$C_{\Phi_2}^{KE} = 2\pi\frac{H}{E}$$

$$C_{\Phi_3}^{KE} = \frac{2.06}{3}\pi K\frac{H}{E}(\delta_{KE}^*)^{-0.425}$$

$$C_{\Phi_4}^{KE} = \frac{2.8}{3}\pi K\frac{H}{E}(\delta_{KE}^*)^{-0.263}$$

  Integral Terms

$$\Phi_1^{KE} = \int_{h'}^{h'+\delta_{KE}^*}(s-h')^{3/2}\phi(s)ds$$

$$\Phi_2^{KE} = \int_{h'+110\delta_{KE}^*}^{\infty}(s-h')\phi(s)ds$$

$$\Phi_3^{KE} = \int_{h'+\delta_{KE}^*}^{h'+6\delta_{KE}^*}(s-h')^{1.425}\phi(s)ds$$

$$\Phi_4^{KE} = \int_{h'+6\delta_{KE}^*}^{h'+110\delta_{KE}^*}(s-h')^{1.263}\phi(s)ds$$

- Jackson and Green Model (JG)

  Constants

$$C_{\Phi_1}^{JG} = \frac{4}{3}\sqrt{\frac{\sigma}{\beta}}$$

$$C_{\Phi_2}^{JG} = \frac{4}{3}\frac{C\pi Y}{2E}$$

  Integral Terms

$$\Phi_1^{JG} = \int_{h'}^{h'+1.9\delta_{JG}^*}(s-h')^{3/2}\phi(s)ds$$

$$\Phi_2^{JG} = \int_{h'+1.9\delta^*_{JG}}^{\infty} [(\delta^*_{JG})^{-0.5}(s-h')^{3/2} e^{-0.25(\frac{s-h'}{\delta^*_{JG}})^{5/12}} + 4\frac{2.84}{C}(1 - e^{(-0.82(\sqrt{\frac{s-h'}{R}}(\frac{s-h'}{1.9\delta^*_{JG}})^{B/2})^{-0.7})})(s-h')(1 - e^{(}-0.04(\frac{s-h'}{\delta^*_{JG}})^{5/9}))]\phi(s)ds$$

where $\delta^*_{JG} = (\frac{\pi CY}{2E})^2(\frac{\beta}{\sigma})$, $C = 1.295e^{0.736v}$ and $D = 0.14e^{23\frac{Y}{E}}$.

- Pullen and Williamsom Model (PW)

  Constants

$$C^{PW}_{\Phi_1} = 0$$

$$C^{PW}_{\Phi_2} = 2\pi\frac{H}{E}$$

  Integral Terms

$$\Phi^{PW}_1 = 0$$

$$\Phi^{PW}_2 = \int_{h'}^{\inf} (s-h')^{3/2}\phi(s)ds$$

A.1.2 Dimensionless Contact Area

- Greenwood and Williamsom Model (GW)

  Constants

$$C^{GW}_{\Lambda_1} = 1$$

$$C^{GW}_{\Lambda_2} = 0$$

  Integral Terms

$$\Lambda^{GW}_1 = \int_{h'}^{\inf} (s-h')\phi(s)ds$$

$$\Lambda^{GW}_2 = 0$$

- Chang, Etsion and Bogy Model (CEB)

  Constants

$$C_{\Lambda_1}^{CEB} = 1$$

$$C_{\Lambda_2}^{CEB} = 1$$

  Integral Terms

$$\Lambda_1^{CEB} = \int_{h'}^{h'+\delta_{CEB}^*} (s - h')\phi(s)\,ds$$

$$\Lambda_2^{CEB} = \int_{h'+\delta_{CEB}^*}^{\inf} [2(s - h') - \delta_{CEB}^*]\phi(s)\,ds$$

  where $\delta_{CEB}^* = (\frac{\pi KH}{2E})^2(\frac{\beta}{\sigma})$.

- Zhao, Maietta and Chang Model (ZMC)

  Constants

$$C_{\Lambda_1}^{ZMC} = 1$$

$$C_{\Lambda_2}^{ZMC} = 2$$

$$C_{\Lambda_3}^{ZMC} = 1$$

  Integral Terms

$$\Lambda_1^{ZMC} = \int_{h'}^{h'+\delta_{ZMC}^1} (s - h')\phi(s)\,ds$$

$$\Lambda_2^{ZMC} = \int_{h'+\delta_{ZMC}^2}^{\infty} (s - h')\phi(s)\,ds$$

$$\Lambda_3^{ZMC} = \int_{h'+\delta^1_{ZMC}}^{h'+\delta^2_{ZMC}} [1 - 2(\frac{(s-h') - \delta^1_{ZMC}}{\delta^2_{ZMC} - \delta^1_{ZMC}})^3 + 3(\frac{(s-h') - \delta^1_{ZMC}}{\delta^2_{ZMC} - \delta^1_{ZMC}})^2](s-h')\phi(s)\,ds$$

where $\delta^1_{ZMC} = (\frac{3\pi KH}{4E})^2(\frac{\beta}{\sigma})$ and $\delta^2_{ZMC} = 54\delta^1_{ZMC}$.

- Kogut and Etsion Model (KE)

  Constants

$$C^{KE}_{\Lambda_1} = 1$$

$$C^{KE}_{\Lambda_2} = 2$$

$$C^{KE}_{\Lambda_3} = 0.93\pi\eta\beta\sigma(\delta^*_{KE})^{-0.136}$$

$$C^{KE}_{\Lambda_4} = 0.94(\delta^*_{KE})^{-0.146}$$

  Integral Terms

$$\Lambda_1^{KE} = \int_{h'}^{h'+\delta^*_{KE}} (s-h')\phi(s)\,ds$$

$$\Lambda_2^{KE} = \int_{h'+110\delta^*_{KE}}^{\infty} (s-h')\phi(s)\,ds$$

$$\Lambda_3^{KE} = \int_{h'+\delta^*_{KE}}^{h'+6\delta^*_{KE}} (s-h')^{1.136}\phi(s)\,ds$$

$$\Lambda_4^{KE} = \int_{h'+6\delta^*_{KE}}^{h'+110\delta^*_{KE}} (s-h')^{1.146}\phi(s)\,ds$$

- Jackson and Green Model (JG)

  Constants

$$C^{JG}_{\Lambda_1} = 1$$

$$C_{\Lambda_2}^{JG} = (\frac{1}{1.9\delta_{JG}^*})^D$$

Integral Terms

$$\Lambda_1^{JG} = \int_{h'}^{h'+1.9\delta_{JG}^*} (s-h')\phi(s)ds$$

$$\Lambda_2^{JG} = \int_{h'+1.9\delta_{JG}^*}^{\infty} (s-h')^{(D+1)}\phi(s)ds$$

where $\delta_{JG}^* = (\frac{\pi CY}{2E})^2(\frac{\beta}{\sigma})$ and $D = 0.14e^{23\frac{Y}{E}}$.

- Pullen and Williamsom Model (PW)

Constants

$$C_{\Lambda_1}^{PW} = 0$$

$$C_{\Lambda_2}^{PW} = 2$$

Integral Terms

$$\Lambda_1^{PW} = 0$$

$$\Lambda_2^{PW} = \int_{h'}^{\inf} (s-h')\phi(s)ds$$

A.2 General Form of Contact Model Equations

These are the general equations used to calculate the dimensionless contact pressure and dimensionless contact area, respectively:

$$p = p_r[C_{\Phi_1}^{(GW,CEB,ZMC,KE,JG,PW)}\Phi_1^{(GW,CEB,ZMC,KE,JG,PW)} + C_{\Phi_2}^{(GW,CEB,ZMC,KE,JG,PW)}\Phi_2^{(GW,CEB,ZMC,KE,JG,PW)} + ... + C_{\Phi_i}^{(GW,CEB,ZMC,KE,JG,PW)}\Phi_i^{(GW,CEB,ZMC,KE,JG,PW)}], i = 1,2,...,n$$

$$A = A_0[C_{\Lambda_1}^{(GW,CEB,ZMC,KE,JG,PW)} \Lambda_1^{(GW,CEB,ZMC,KE,JG,PW)} + C_{\Lambda_2}^{(GW,CEB,ZMC,KE,JG,PW)} \Lambda_2^{(GW,CEB,ZMC,KE,JG,PW)} + ... + C_{\Lambda_i}^{(GW,CEB,ZMC,KE,JG,PW)} \Lambda_i^{(GW,CEB,ZMC,KE,JG,PW)}], i = 1, 2, ..., n$$

where $p_r = \eta\beta\sigma E$; $A_0 = \eta\beta\sigma\pi$; C_{Λ_1}/C_{Φ_1} and C_{Λ_2}/C_{Φ_2} are the elastic and plastic constants, respectively, and C_{Λ_i}/C_{Φ_i}, where $i = 3, 4, ..., n$, are the elastoplastic constants of the contact models.

A.3 Interpolation of Contact Models Integration Terms

In order to facilitate and speed up the simulation procedure with regard to the pressure calculations obtained from the contact models, the interpolation function *spline* was used, available in the MATLAB software (Mathworks registered product), which generates a *struct* object containing characteristic fields (*fields*) for future evaluation of the interpolation object. The interpolated terms were called at each time step in the simulation and evaluated numerically using the *ppval* function, which returns the numerical value of the interpolated curve as a function of the dimensionless lubricant film thickness $\bar{h}$. The integration terms presented in sections A.1.1 and A.1.2 were interpolated using this technique.